A Travelling Cable System: Apparatus Development, System Modeling, and Vibration Control

Sung-Wen, Dung

Supervised by Dr. Kefu Liu

Date: 10th Octorber 2005

A Thesis Submitted In Partial Fulfillment Of The Requirements

Of The MscEng Degree In Control Engineering

Faculty of Engineering

Lakehead University

Thunder Bay, Ontario

Your file Votre référence
ISBN: 978-0-494-15614-8
Our file Notre référence
ISBN: 978-0-494-15614-8

Abstract

The vibration of axially moving materials with arbitrarily varying length has received increased attention due to both the interesting behaviours of such systems and the many applications such as deep mine hoisting systems, high-speed elevator systems and robotic arms in a prismatic joint. Vibration control is needed for such system; especially when there are safety, speed, and precision concerns. The model governing vibration of such systems is time varying. Control of time-varying systems poses many challenges. The objective of this research is to develop an experimental system to study the dynamics of a travelling cable with variable length and to test control strategies for vibration suppression.

In this research, an experimental system is developed, which includes a travelling cable apparatus, a signal conditioning circuit board, a data acquisition board, a computer system, and sensors. The mathematical models of the lateral vibration of stationary and axially moving cables are presented. Computer simulations are performed to understand the dynamics of the travelling cable. A preliminary testing of the experimental system is preformed

Boundary control method is used to suppress the vibration of the cable. Two closed-loop feedback control systems, direct velocity feedback control and observer output feedback control with optimal feedback gains, are designed to suppress the vibration of the stationary cable. Both control systems are simulated by computer and tested by experiment. An observer-based feedback control system with variable optimal feedback gains is designed to suppress the vibration of the travelling cable. The performance of the controller is tested using computer simulations.

Acknowledgement

I would like to express sincere gratitude to my supervisor Dr. Kefu Liu for his endless guidance and support. I would like to express my appreciation to my co-supervisor Dr. Henri Saliba for his generous support. I would like to thank Dr. Xiaoping Liu for his valuable suggestions. I would also like to thank Mr. Kailash Bhatia for his technical assistance with the production of the experimental apparatus.

I dedicate this work to my family, especially my wife Vivian, for their love and support.

Contents

List of Figures

List of Tables

Chapter 1

Introduction

Many mechanical systems use the mechanism of axially moving materials with arbitrarily varying length. The model governing vibration of such systems is time varying. Control of time-varying systems poses many challenges. This research is motivated by the need for further study of the vibration control of travelling cables with arbitrarily varying length. The main task of the research is to develop an experimental system to study the dynamics of a travelling cable with variable length and to test control strategies for vibration suppression.

The rest of the chapter is organized as follow: Section 1.1 reviews the previous studies on axially moving materials with arbitrarily varying length, Section 1.2 lists the objectives of the thesis research, and Section 1.3 outlines the thesis.

1.1 Overview of the Previous Studies on Axially Moving Materials with Arbitrarily Varying Length

Axially moving materials with arbitrarily varying length are found in many engineering applications such as deep mine hoisting [1-3] and elevator cables [1, 4-11], satellite tethers [12], and robotic arms in a prismatic joint [13-16]. The vibration behaviours of axially moving materials with arbitrarily varying length in these applications are often

being studied for the improvements of the performance. The studies on axially moving material can be classified into two areas: dynamics modeling and vibration control.

In most cases, the axially moving materials with arbitrarily varying length are modeled as strings or beams. Among the various studies, high-rise elevator cables have received increased attention due to its high flexibility, low intrinsic damping and high travelling speed. The longitudinal vibration and natural frequencies of a cable and car system were studied in [1]. The parametric resonance responses of a non-linear rope model with varying parameters were analyzed in [4]. The free vibration of a string with time-varying length was analyzed by using a travelling wave technique in [5]. The free and forced lateral vibrations of a travelling string with time-varying length and a mass-spring termination were examined in [6, 7]. The linear dynamics, stability, and rates of change of energies of translating media with variable length were analyzed in [8]. Effects of boundary conditions on the energy and stability characteristics of translating media with variable length were examined in [9]. Effects of the small bending stiffness of the elevator cables was studied for the both stationary and travelling cables with different boundary conditions in [10]. A scaled model of a high-rise and high-speed model was developed for studying the lateral dynamics of the elevator cable in [11].

Modeling the dynamics of axially moving material with arbitrarily varying length poses many challenges which require developing a distributed parameter model coupled with a discrete model or a continuous model. The fundamental dynamics characteristics of a moving material with variable length differ significantly from its time-invariant counterpart. While the energy of vibration of a moving material decreases and increases in general during extension and retraction, respectively, the amplitude of its response can behave in an opposite manner.

Generally speaking, vibration will affect the performance and efficiency of a particular mechanical system. Therefore, vibration control is needed for such systems; especially systems where there are concerns with speed and precision.

Vibration control of axially moving material systems with constant length such as power transmission belts, paper tapes, band saws has been developed for decades. In the earlier days, studies of vibration control focused on the stabilization of the axially moving system by passive damping and stiffness designs [17]. Later on, active vibration control has received increased attention due to its superior performance. Since 1990, many different active vibration control methods have been designed based on the feedback control principle such as adaptive control methods, transfer function methods, direct velocity feedback method, and boundary control methods [18]. The controllability and the observability of distributed gyroscopic and time-varying systems are analyzed in [19, 20], where it is shown that all the modes of vibration can be stabilized. Among all the active control methods for axially moving material, the boundary control method is the most efficient and easiest method to implement [21-25].

Recently, several researchers used the external force generated from a point-wise controller to control the vibration of axially moving beams and strings with arbitrary varying length [26, 27]. Sufficient conditions for uniform stability and uniform exponential stability of the control system have also been obtained via Lyapunov stability criteria. The boundary control method with optimal control gains has been recognized as the fastest controller for reducing vibratory energies. Also, it has been shown that under optimal control gains, moving materials with arbitrary varying length can be completely stabilized during both extension and retraction movement.

1.2 Objectives of the Research

Most of the previous studies focused on modeling and computer simulations, and little effort has been made on experimental implementations. Therefore the objectives of this research includes:

- To develop an experimental system that can be used to study the dynamics of a travelling cable with variable length and to test control strategies for vibration suppression.
- To develop an analytical model to simulate the dynamics of the travelling cable in the experiment system.
- To develop different control algorithms to suppress the lateral vibration of the system.
- To implement the active control to the experimental system.

1.3 Outline of the Thesis

The following chapters of the thesis are organized as follows: Chapter 2 describes the development of the experimental system, Chapter 3 describes the modeling of the travelling cable model and presents some computer simulation results, Chapter 4 presents some preliminary test results of the experiment system, Chapter 5 describes the modeling of the boundary controlled system for the stationary cable system and presents some simulation and experimental results, Chapter 6 describes the modeling of the boundary control system for the travelling cable system and presents some simulation results, and Chapter 7 summarizes the thesis and recommends future work.

Chapter 2

The Experimental System

An experimental system is needed for this study. The system should include a travelling cable apparatus, different types of sensors, a signal conditioning system, and a computer system equipped with a data acquisition (DAQ) board. This chapter describes the developed experimental system. The rest of the chapter is organized as follows: Section 2.1 describes the design requirements and constraints of the experimental system, Section 2.2 describes the final design of the travelling cable apparatus, Section 2.3 presents a more detailed design of the actuator, Section 2.4 explains the usages of different types of sensors and the signal conditioning system, Section 2.5 describes the DAQ board and the computer system, and Section 2.6 is a brief conclusion.

2.1 Design Requirements and Constraints

Several design requirements were observed. First, the cable has to be able to vary its length while maintaining its boundary conditions. Second, lateral vibration of the cable is constrained to one plane to simplify the problem. Third, the tension of the cable is adjustable. Fourth, an actuator is needed to implement a boundary force control. Fifth, a closed-loop control system is needed for varying the travelling speed of the cable in the desired way.

The design of the system was subjected to several constraints. First, the budget is very limited. Second, the height of the apparatus is restricted by several factors: the room height, the dimensions of stocks used for the frame and guide rails, length of sensor cables, etc. Third, the apparatus must be easy to be disassembled. The budget constraint greatly affected the final design, reflected in the selection of materials, instrumentation, and fabrication.

2.2 Travelling Cable Apparatus

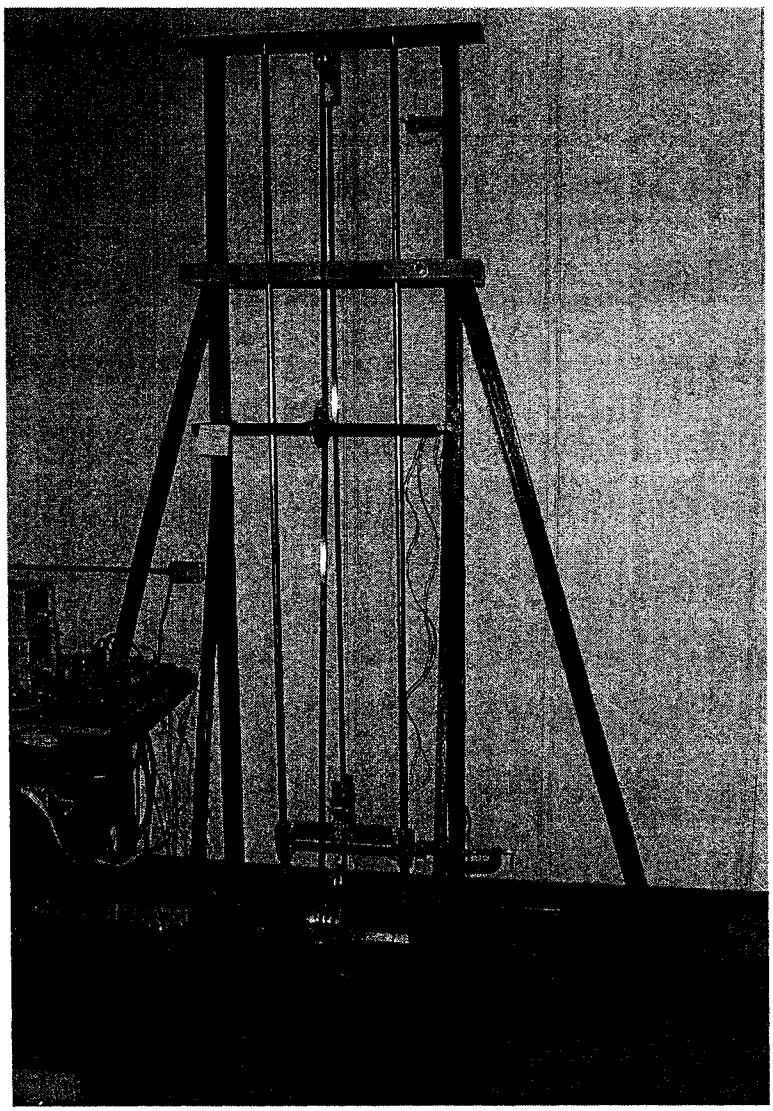

Figure 2.1: Travelling cable apparatus

A travelling cable apparatus was designed and built in house, as shown in Figure 2.1. The apparatus is able to simulate the dynamics of a travelling cable with variable length and to test control strategies for vibration suppression. A schematic diagram of the travelling apparatus is shown in Figure 2.2.

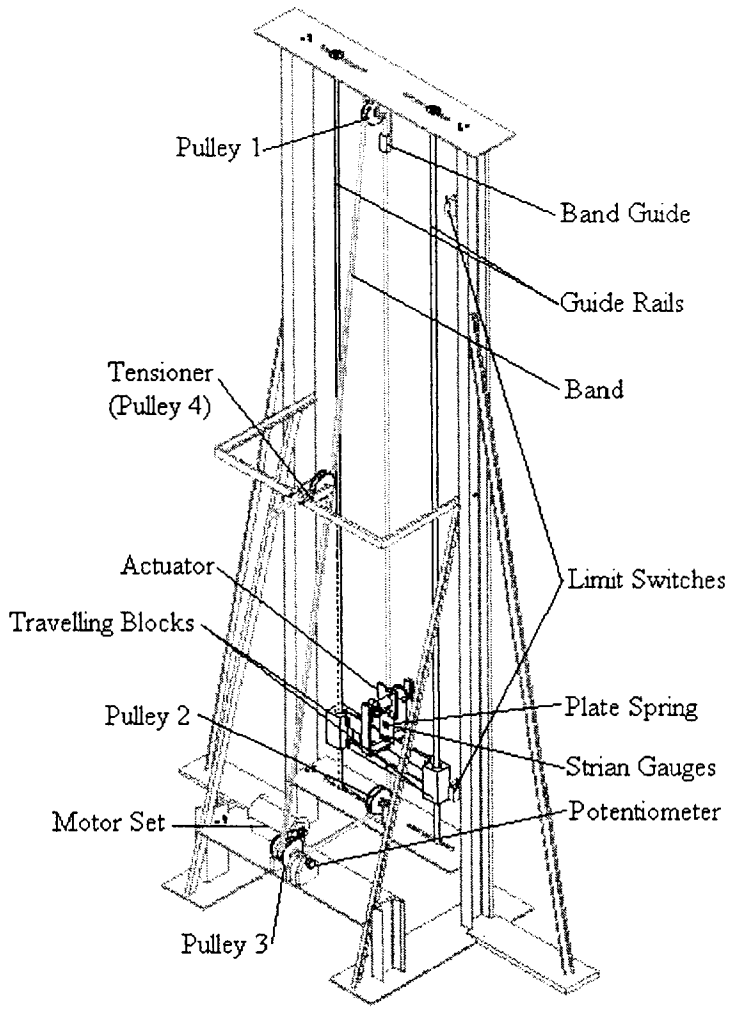

Figure 2.2: Schematic diagram of the travelling cable apparatus

To constrain the lateral vibration in one plane, a steel band of width 12.7 mm and thickness 0.3 mm is used because it is readily available. The lower end of the band is attached to an electromagnet that is the main component of the actuator. Using a thin aluminium plate, the electromagnet is connected to a rigid aluminium bar named as upper connection bar. The thin aluminium plate acts as an end spring that restricts the motion of

the electromagnet and creates the lower end boundary condition. A rail system is designed to meet the requirement of varying the cable length while maintaining the lower end boundary condition. Two grounded steel bars with diameter of 95 mm and length of 2360 mm are used as guide rails in the rail system. Two custom made aluminium blocks with internal linear bearings provide smooth travel along the guide rails. The band runs through a band guide made from Teflon, providing the top fixed end boundary condition. The band further runs through four pulleys and connects to a rigid aluminium bar named as lower connection. By connecting the upper and the lower connection bars to the travelling blocks, the band forms a loop.

A rubber band is glued in the groove of each pulley to increase friction. Pulley four is mounted at the end of an adjusting screw, which allows the adjustment of the tension of the band. A direct current (DC) motor (Dumore) drives pulley three through a pulley and belt set. The motor has a built-in gearbox with a transmission ratio of 13:1. The motor is rated to run 180 RPM at 1.5 amps with no load and 160 rpm at 6.2 to 7.2 amps with a load of 2.712 Nm. The pulley and belt set has a transmission ratio of 11:10. A potentiometer is attached to the shaft of pulley three.

The frame that houses the moving system is made of four steel channels and seven steel plates and supported by four steel angles. Two limit switches are installed to shut off the motor before the actuator reaches the highest position or the lowest position. The rail bars are subjected to some tension to ensure their straightness. A pinned-pinned boundary condition is observed at the ends of the rail bars, which is not stable enough for a travelling system. To solve the problem, a temporary clamping system is designed to further secure the rail bars. The clamping system reduces the maximum travel distance of the band from 1844 mm to 1200 mm.

2.3 Actuator

A low cost actuator is designed in house. As shown in Figure 2.3, it consists of an electromagnet, a plate spring, two permanent magnets, and a mounting frame.

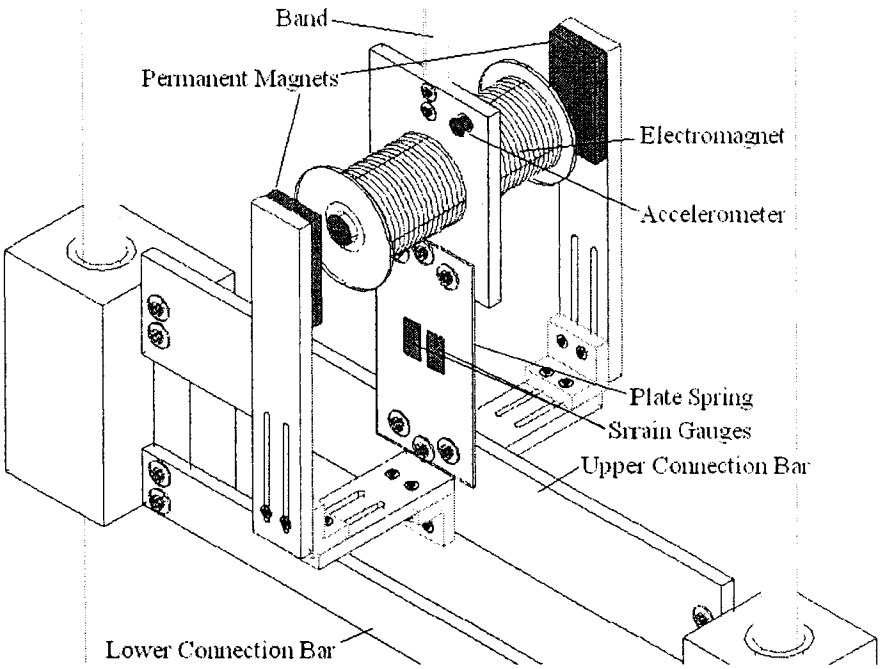

Figure 2.3: Actuator

As mentioned in Section 2.2, the electromagnet is connected between the lower end of the band and the plate spring. A steel rod with diameter of 14 mm and length of 130 mm is used as the core for the electromagnet. The steel rod is pressed into an aluminium plate, which allows the connection of the electromagnet to the band and the plate spring. Gauge 18 wire is used to wind a core of 1850 turns. Each of the permanent magnets is glued on its holding seat to interact with the electromagnetic field. The poles of the two permanent magnets are arranged in such a way that, when an alternating current is applied to the electromagnet, a non-contact actuating force can be generated, as shown in Figure 2.4.

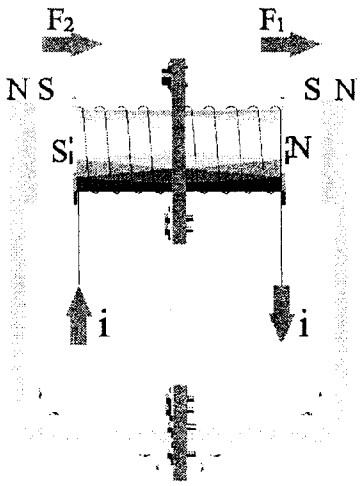

Figure 2.4: Actuating force

The interaction forces F_1 and F_2 between the permanent magnets and the electromagnet can be expressed as

$$F_1 = \gamma \frac{i}{(G_{ap} - x)^2}, \tag{2.1}$$

$$F_2 = \gamma \frac{i}{(G_{ap} + x)^2}, \tag{2.2}$$

where γ is a constant related to the property of the actuator, i is the current applied to the wire, x is the displacement of the electromagnet, and G_{ap} is the air gap between the electromagnet and the permanent magnets. For the slight motion of the electromagnet about its equilibrium position, equations (2.1) and (2.2) can be approximated as

$$F_1 \approx \gamma \frac{i}{G_{ap}^2}\left(1 + \frac{2x}{G_{ap}}\right) \tag{2.3}$$

$$F_2 \approx \gamma \frac{i}{G_{ap}^2}\left(1 - \frac{2x}{G_{ap}}\right) \tag{2.4}$$

Summing the forces results in the net electromagnet actuating force as

$$F_{net} = 2\gamma \frac{i}{G_{ap}^2} \tag{2.5}$$

2.4 Sensors and the Signal Conditioning System

Three types of sensors are used: potentiometer, accelerometer, and strain gauge. A potentiometer is used for the measurement of the band position. The relationship between the length of the travelling band and the voltage reading from the potentiometer is determined. An accelerometer is used to sense the lateral acceleration of the actuator or the band. Strain gauges produce a voltage signal that is proportional to the deflection of the plate spring. With the strain gauge signal the lateral displacement of the electromagnet can be found. Figure 2.5 is a schematic of the signal conditioning system.

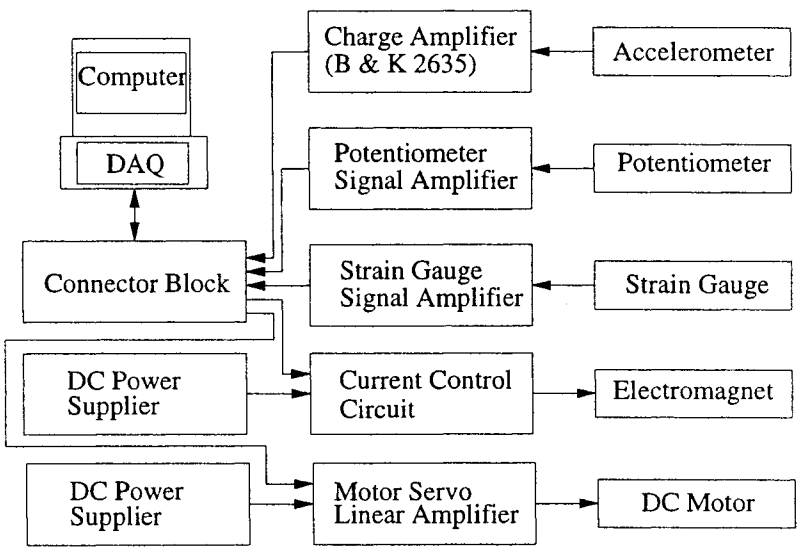

Figure 2.5: Signal conditioning system

A charge amplifier (B & K 2635) is used to condition the accelerometer signal. A signal conditioning board is assembled in house to condition the rest of the signals. Circuitries used were designed and tested in the previous researches. The board consists of a potentiometer signal amplifier, a strain gauge signal amplifier, an unregulated DC power supplier, a current control circuit, and a motor servo linear amplifier.

2.5 DAQ Board and Computer System

A Pentium III personal computer is used. An academic starter kit from National Instruments is used for data acquisition, which includes a data acquisition board (PCI-6024E), a connector block (BNC-2120) and interfacing software LabView.

2.6 Conclusions

An experimental system is developed. The travelling cable apparatus meets all the design requirements. An actuator is designed which is capable of generating a non-contact actuating force. The experimental system also includes sensors, signal conditioning unit and a computer system with a DAQ board.

Chapter 3

Modelling and Simulation

Translating media are typically modelled as a translating string or tensioned Euler-Bernoulli beam. In this study, the cable is modelled as a translating string as the flexural rigidity of the band is very small. For mathematical modelling, two stationary cable models and a travelling cable model are considered. The mathematical models consist of distributed parameters with time varying states. Control of such system poses many challenges. Boundary control method is used.

Boundary control method has two major advantages for controlling such systems. First, there is no attachment of sensors or actuators required along the cable. Second, the end boundaries of the cable are always fixed at its ends.

The state space representation of the systems for the stationary and travelling models are presented. Natural frequencies of two stationary models are calculated. A computer simulation is conducted to study the dynamics of the travelling cable. The rest of the chapter is organized as follows: Section 3.1 describes the modelling of stationary cable models and examines the natural frequencies of the systems, Section 3.2 describes the modeling of the travelling cable model and presents some computer simulation results, Section 3.3 is a brief summary.

3.1 Stationary Cable Model

3.1.1 Mathematical Modelling

Two stationary models with different boundary conditions are considered. Both models are modelled as tensioned strings with fixed length l. Shown in Figure 3.1 are model A and B. Model A represents a tensioned string with fixed-fixed boundary condition. For model B, the string is fixed at one end and attached to a point mass m_a at the other end. The point mass represents the mass of the actuator. The movement of the point mass is restricted by a resultant spring stiffness k_a and damper d_a, which are created in the lateral direction by the plate spring. A constant tension force p is applied to the string.

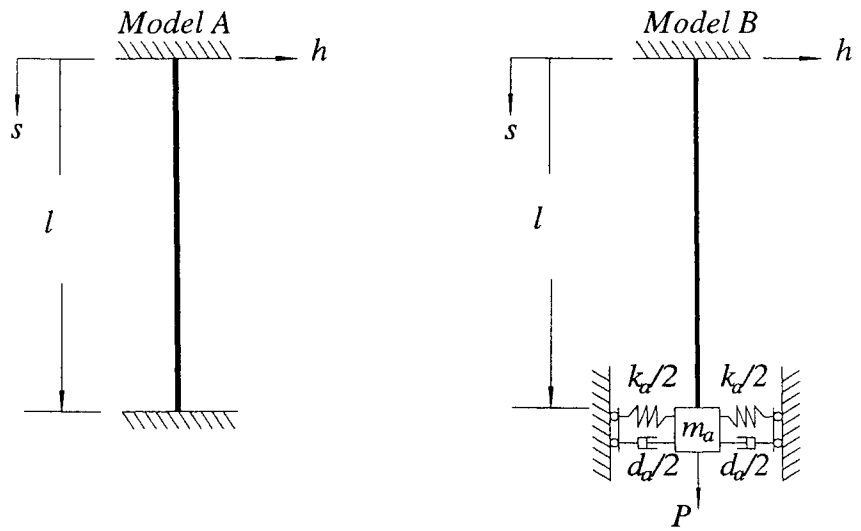

Figure 3.1: Stationary cable models

A governing equation of the stationary model is derived by examining the force diagram of an infinitesimal element of a fixed-fixed string, as shown in Figure 3.2. The string has uniform density per length ρ and length l. The deflection of the string is denoted by $w(s,t)$. Forces acting on a point along the string contain an external distributed force $f(s,t)$ and a tension force $\tau(s,t)$.

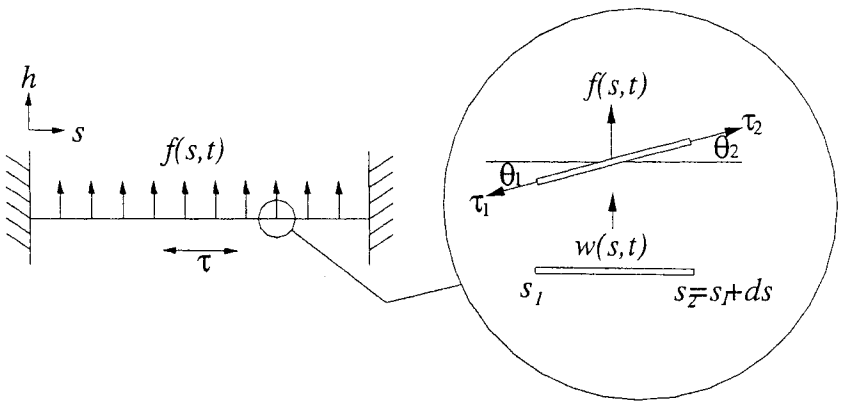

Figure 3.2: Free body diagram of a fixed-fixed string

Appling Newton's second law of motion yields

$$f(s,t)ds - \tau_1 \sin\theta_1 + \tau_2 \sin\theta_2 = \rho \frac{\partial^2 w(s,t)}{\partial t^2} ds \,. \tag{3.1}$$

Assuming that θ_1 and θ_2 are very small. For small θ,

$$\tau_1 \sin\theta_1 \cong \tau \tan\theta = \left(\tau \frac{\partial w(s,t)}{\partial s} \right)\Big|_{s_1} \tag{3.2}$$

and

$$\tau_2 \sin\theta_2 = \left(\tau \frac{\partial w(s,t)}{\partial s} \right)\Big|_{s_2} , \tag{3.3}$$

where $(\partial w/\partial s)|_{s_1}$ and $(\partial w/\partial s)|_{s_2}$ are the slope of the string at points s_1 and s_2, respectively. The relation between $\tau(\partial w/\partial s)|_{s_1}$ and $\tau(\partial w/\partial s)|_{s_2}$ can be further derived by evaluating the Taylor series expansion around point s_1. This yields

$$\left(\tau \frac{\partial w(s,t)}{\partial s} \right)\Big|_{s_2} = \left(\tau \frac{\partial w(s,t)}{\partial s} \right)\Big|_{s_1} + \frac{\partial}{\partial s}\left(\tau \frac{\partial w(s,t)}{\partial s} \right)\Big|_{s_1} ds + O(ds^2) \tag{3.4}$$

where $O(ds^2)$ denotes the rest of the Taylor series, which includes terms of order ds^2 and higher. Since ds is very small, $O(ds^2)$ is even smaller and hence neglected. Substituting equation (3.4) into equation (3.1) and dividing by ds gives

$$f(s,t)+\frac{\partial}{\partial s}\left(\tau(s)\frac{\partial w(s,t)}{\partial s}\right)=\rho\frac{\partial^2 w(s,t)}{\partial t^2} \tag{3.5}$$

If no external force is applied, the free later vibration of the stationary model is governed by

$$\rho w_{tt}(s,t)-(\tau(s)w_s(s,t))_s=0,\quad 0<s<l, \tag{3.6}$$

where the subscripts 's' and 't' denote partial differentiation with respect to s and t, respectively. The tension $\tau(s)$ is given by

$$\tau(s)=p+m_a g+(l-s)\rho, \tag{3.7}$$

where p is the tension due to the tensioner and g is the gravity acceleration. The boundary conditions of the cable with fixed ends are

$$w(0,t)=w(l,t)=0. \tag{3.8}$$

The boundary conditions of the cable with a spring and a damper attached are

$$w(0,t)=0,\quad m_a w_{tt}(l,t)+d_a w_t(l,t)+k_a w(l,t)=-\tau(l)w_s(l,t). \tag{3.9}$$

By the modified Galerkin's method, the solution of equation (3.6) can be expressed in the form

$$w(s,t)=\sum_{j=1}^{n} q_j(t)\phi_j(s), \tag{3.10}$$

where $\phi_j(s)$ is the jth trial function, $q_j(t)$ is the jth generalized coordinate, and n is the number of included modes. The following development is based on the work presented in [10]. The trial functions used for model A are

$$\phi_j(s)=\sqrt{\frac{2}{l}}\sin\left[\frac{j\pi s}{l}\right]. \tag{3.11}$$

The trial functions used for model B are

$$\phi_j(s)=\sqrt{\frac{2}{l}}\sin\left[\frac{(2j-1)\pi s}{2l}\right]. \tag{3.12}$$

The initial conditions for the generalized coordinates and velocities are

$$q_j(0) = \int_0^l \phi_j(s) w(s,0) ds\,, \tag{3.13}$$

$$\dot{q}_j(0) = \int_0^l \phi_j(s) w_t(s,0) ds\,, \tag{3.14}$$

where $w(s,0)$ and $w_t(s,0)$ are the initial displacement and velocity of the cable, respectively, dot denotes derivation with respect to t. Substituting equation (3.10) into equation (3.6), multiplying the governing equation by $\phi_i(s)$ $(i = 1,2,....n)$, integrating it from $s = 0$ to l, and applying the boundary conditions yield

$$M_q \ddot{q}(t) + D_q \dot{q}(t) + K_q q(t) = 0\,, \tag{3.15}$$

where $q = [q_1, q_2, ..., q_n]^T$ is the generalized coordinate vector. M_q, K_q, and D_q represent the mass, stiffness, and damping matrices for the stationary models, respectively, and their elements can be expressed as

$$M_{q_{ij}} = \int_0^l \rho \phi_i(s) \phi_j(s) ds + m_a \phi_i(l) \phi_j(l)\,, \tag{3.16}$$

$$K_{q_{ij}} = \int_0^l \tau(s) \phi_i'(s) \phi_j'(s) ds + k_a \phi_i(l) \phi_j(l)\,, \tag{3.17}$$

$$D_{q_{ij}} = d_a \phi_i(l) \phi_j(l)\,, \tag{3.18}$$

in which the prime denotes differentiation with respect to s. The discretized equations for model A are given by equations (3.15) to (3.18) with $m_a = k_a = d_a = 0$.

Model B is used to apply the boundary control strategy for the stationary cable. Figure 3.3 shows the boundary-controlled model for the stationary cable. A control input $u(t)$ is applied at the point mass m_a for the purpose of suppressing the lateral vibration of the cable. A disturbance force $f(t)$ is applied at a fixed point on the cable, located at $s = l - r$.

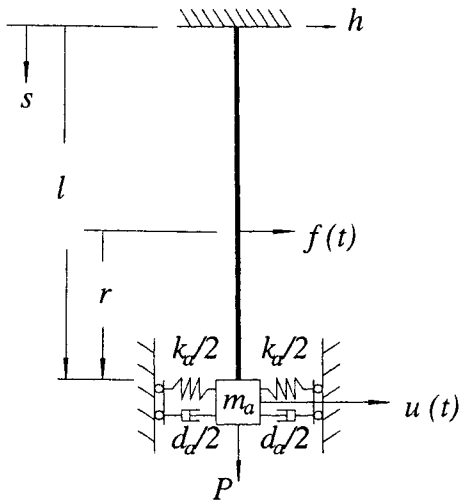

Figure 3.3: Stationary cable model with boundary control

The governing equations for model B can be developed from equations (3.6) and (3.15), which can be expressed as

$$\rho w_{tt}(s,t)-(\tau(s)w_s(s,t))_s = u(t)\delta(s-l)+f(t)\,\delta(s-(l-r)),\quad 0<s\le l, \tag{3.19}$$

$$M_q\ddot{q}(t)+D_q\dot{q}(t)+K_q q(t)=B_{q1}u(t)+B_{q2}f(t), \tag{3.20}$$

respectively, where δ is the Dirac Delta, and B_{q1} and B_{q2} are input matrixes, and their elements can be expressed as

$$B_{q1}=[\phi_1(l)\quad \phi_2(l)\cdots\phi_n(l)]^{\mathrm{T}}, \tag{3.21}$$

$$B_{q2}=[\phi_1(l-r)\quad \phi_2(l-r)\cdots\phi_n(l-r)]^{\mathrm{T}}, \tag{3.22}$$

Equation (3.20) can be written into a state-space representation

$$\begin{aligned}\dot{x}(t)&=Ax(t)+B_1u(t)+B_2f(t)\\ y(t)&=Cx(t)\end{aligned}, \tag{3.23}$$

where the state vector is

$$x(t)=\begin{bmatrix}q(t)\\ \dot{q}(t)\end{bmatrix}, \tag{3.24}$$

the system matrix is

$$A = \begin{bmatrix} 0_{n\times n} & \mathrm{I} \\ -M_q^{-1}K_q & -M_q^{-1}D_q \end{bmatrix}, \tag{3.25}$$

the input matrices are

$$B_1 = \begin{bmatrix} 0_{n\times 1} \\ M_q^{-1}B_{q1} \end{bmatrix}, \tag{3.26}$$

$$B_2 = \begin{bmatrix} 0_{n\times 1} \\ M_q^{-1}B_{q2} \end{bmatrix}. \tag{3.27}$$

The formation of the output matrix C depends on the type of the sensor used and on the location of the sensor during the experiment. The system's output that will be used for feedback purpose is the actuator's lateral displacement $w_a(l,t)$ or the lateral velocity $\dot{w}_a(l,t)$. The lateral displacement $w_a(l,t)$ and the lateral velocity $\dot{w}_a(l,t)$ of the actuator can be expressed as

$$w_a(l,t) = C_1\, q(t), \tag{3.28}$$

$$\dot{w}_a(l,t) = C_1\, \dot{q}(t), \tag{3.29}$$

, respectively, where C_1 is a $1\times n$ vector, and its elements can be expressed as

$$C_{1j} = g_y \phi_j(l), \tag{3.30}$$

where is g_y the correction factor of the sensor's measurement.

Therefore, if the displacement of the actuator is used as the output $y(t)$, the output matrix C can be expressed as

$$C = [C_1 \quad 0_{1\times n}]. \tag{3.31}$$

If the velocity of the actuator is used as the output $y(t)$, the output matrix C can be expressed as

$$C = [0_{1\times n} \quad C_1]. \tag{3.32}$$

3.1.2 Natural Frequencies of the Stationary Cables

Natural frequencies of model A are used to identify the tension of the belt loop. Natural frequencies of model B are also obtained for validating the experimental results. For each model, the undamped natural frequencies of the first three modes are obtained. Two different lengths of cable, specified as l_{long} and l_{short} in Section 4.3, are used to verify the results. All parameters used are listed in Table 3.1.

Parameters	ρ (kg/m)	g (m/s^2)	k_a (N/m)	m_a (kg)	l_{long} (m)	l_{short} (m)
Mode A	0.03	9.81	0	0	1.84	0.982
Mode B			756	0.803		

Table 3.1: Parameters used for calculating natural frequencies

The natural frequencies are obtained from the boundary value problem and eigenvalue problem. The natural frequencies obtained from the boundary value problem for model A and model B can be expressed as

$$\omega_n = \frac{n\pi}{l} b, \tag{3.33}$$

$$\omega_n = \sigma_n b, \tag{3.34}$$

respectively, where ω_n is the nth natural frequency (rad/s), $b = \sqrt{\tau/\rho}$ called the wave speed, and σ_n can be obtained from

$$\tan \sigma_n l = \frac{\sigma_n \tau}{m_a \sigma_n^2 b^2 - k_a}. \tag{3.35}$$

The natural frequencies obtained from eigenvalue problem can be expressed as

$$\omega_n = \sqrt{\lambda_n}, \tag{3.36}$$

where λ_n is nth eigenvalue of the spectral matrix $\tilde{K}$. The spectral matrix can be expressed as

$$\tilde{K} = M_q^{-1/2} K_q M_q^{-1/2} \tag{3.37}$$

The natural frequencies of model A with different magnitude of tension at $l = l_{long}$ are obtained by using equation (3.33). The results are plotted in Figure 3.4. In Figure 3.4, the solid line, the dashed line, and the dotted line indicate the natural frequency of the first, the second, and the third mode, respectively.

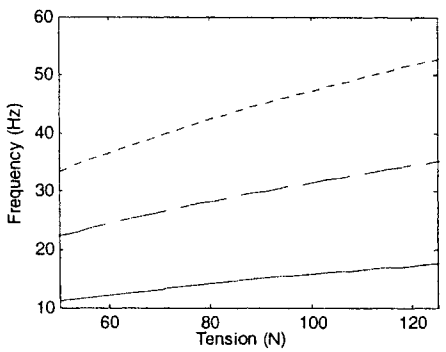

Figure 3.4: Relationship between natural frequencies and tension

From Figure 3.4, the first three natural frequencies of the cable at $l = l_{long}$ with the fixed-fixed boundary condition should be 14.9, 29.8, and 44.7 Hz. The pattern of the experimental results matches the observation from equation (3.33). With Figure 3.4, the magnitude of tension is found to be approximately 90 N. The same tension is used to calculate the undamped natural frequencies of model A at $l = l_{short}$. The undamped natural frequencies of the first three modes, ω_i $(i = 1, 2, 3)$, of each model at $l = l_{long}$ and $l = l_{short}$ are obtained and listed in Table 3.2.

$l = l_{long}$				
Model A	(1)	14.88 Hz	29.77 Hz	44.65 Hz
	(2)	14.91 Hz	29.81 Hz	44.72 Hz
Model B	(1)	7.46 Hz	22.33 Hz	37.21 Hz
	(2)	6.96 Hz	19.31 Hz	31.94 Hz
$l = l_{short}$				
Model A	(1)	27.89 Hz	55.78 Hz	83.66 Hz
	(2)	27.91 Hz	55.82 Hz	83.73 Hz
Model B	(1)	13.94 Hz	41.83 Hz	69.71 Hz
	(2)	12.23 Hz	35.82 Hz	59.57 Hz

Table 3.2: The first three natural frequencies (Hz). (1) and (2) represent the results obtained form boundary values problem and eigenvalue problem, respectively.

3.2 Travelling Cable Model

3.2.1 Mathematical Modeling

Unlike the stationary cable models, the travelling cable model has a variable length $l(t)$, an axial velocity $\dot{l}(t)$, and an axial acceleration $\ddot{l}(t)$. Figure 3.5 shows the schematic of model C, the moving cable model.

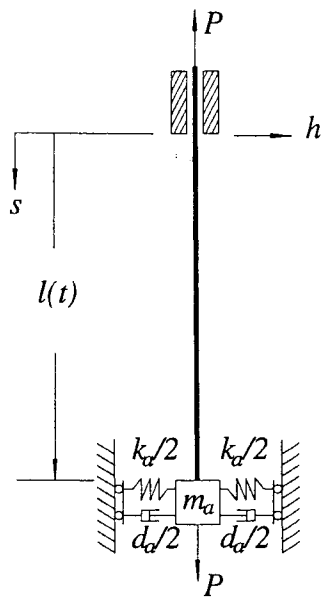

Figure 3.5: Model C (moving cable model)

The following development is based on the work presented in [10]. Rearranging equation (3.6), the free lateral vibration of the model is governed by

$$\rho\frac{D^2w(s,t)}{Dt^2}-[\tau(s,t)w_s(s,t)]_s=0,\quad 0<s<l(t), \tag{3.38}$$

where

$$\frac{D^2}{Dt^2}=\frac{\partial^2}{\partial t^2}+2\dot{l}(t)\frac{\partial^2}{\partial s\partial t}+\dot{l}^2(t)\frac{\partial^2}{\partial s^2}+\ddot{l}(t)\frac{\partial}{\partial s}, \tag{3.39}$$

$\tau(s,t)$ is the tension at position x at time t given by

$$\tau(s,t)=p+[m_a+\rho(l(t)-s)][g-\ddot{l}(t)]. \tag{3.40}$$

The boundary conditions for the moving cable model is given by

$$w(0,t)=0,\quad m_a\frac{D^2w(l(t),t)}{Dt^2}+d_a\frac{Dw(l(t),t)}{Dt}+k_aw(l(t),t)=-\tau(l(t),t)w_s(l(t),t),\qquad(3.41)$$

where.

$$\frac{D}{Dt}=\frac{\partial}{\partial t}+\dot{l}(t)\frac{\partial}{\partial s}.\qquad(3.42)$$

Once again, the solution of equations (3.38) and (3.41) can be expressed in the form

$$w(s,t)=\sum_{j=1}^{n}q_j(t)\phi_j(s,t),\qquad(3.43)$$

where $\phi_j(x,t)$ are the time-dependent trial functions. The trail function can be expressed as

$$\phi_j(s,t)=\frac{1}{\sqrt{l(t)}}\psi_j(\xi),\qquad(3.44)$$

where $\xi=s/l(t)$, and $\psi_j(\xi)$ is the jth normalized eigenfunction given by

$$\psi_j(\xi)=\sqrt{2}\sin\left[\frac{(2j-1)\pi\xi}{2}\right].\qquad(3.45)$$

The initial conditions for the generalized coordinates and velocities are

$$q_j(0)=\sqrt{l(0)}\int_0^1 w(\xi l(0),0)\psi_j(\xi)d\xi,\qquad(3.46)$$

$$\dot{q}_j(0)=\sqrt{l(0)}\int_0^1 w_t(\xi l(0),0)\psi_j(\xi)d\xi+\frac{\dot{l}(0)}{l(0)}\sum_{i=1}^{n}q_i(0)\int_0^1\xi\psi_i'(\xi)\psi_j(\xi)d\xi+\frac{\dot{l}(0)}{2l(0)}q_j(0),\qquad(3.47)$$

where $w(\xi l(0),0)$ and $w_t(\xi l(0),0)$ are the initial displacement and velocity, respectively, and the dot and prime denote derivation with respect to t and ξ, respectively. Substituting equations (3.43) into equation (3.38), multiplying the governing equation by $\psi_i(\xi)/\sqrt{l(t)}$, integrating it from $s=0$ to $l(t)$, and applying the boundary conditions yield

$$M_q(t)\ddot{q}(t)+\left[D_q(t)+G_q(t)\right]\dot{q}(t)+\left[K_q(t)+H_q(t)\right]q(t)=0,\qquad(3.48)$$

where $q=[q_1,q_2,...,q_n]^{\mathrm{T}}$ is the generalized coordinates. $M_q(t)$, $K_q(t)$, $D_q(t)$, $G_q(t)$, and $H_q(t)$ represent the mass, stiffness, damping, skew-symmetric gyroscopic and circulatory matrices for model C, respectively, and their elements can be expressed as

$$M_{q_{ij}}(t)=\rho\delta_{ij}+m_a l^{-1}(t)\psi_i(1)\psi_j(1), \tag{3.49}$$

$$K_{q_{ij}}(t)=\frac{1}{4}\rho l^{-2}(t)\dot{l}^2(t)\delta_{ij}-\rho l^{-2}(t)\dot{l}^2(t)\int_0^1(1-\xi)^2\psi_i'(\xi)\psi_j'(\xi)d\xi+pl^{-2}\int_0^1\psi_i'(\xi)\psi_j'(\xi)d\xi$$

$$+\rho l^{-1}(t)[g-\ddot{l}(t)]\int_0^1(1-\xi)\psi_i'(\xi)\psi_j'(\xi)\,d\xi-m_a l^{-2}(t)[g-\ddot{l}(t)]\int_0^1\psi_i'(\xi)\psi_j'(\xi)\,d\xi$$

$$+\left[m_a\left(\frac{3}{4}\dot{l}^2(t)l^{-3}(t)-\frac{1}{2}\ddot{l}(t)l^{-2}(t)\right)-\frac{1}{2}d_a l^{-2}(t)\dot{l}(t)+k_a\,l^{-1}(t)\right]\psi_i(1)\psi_j(1), \tag{3.50}$$

$$D_{q_{ij}}(t)=d_a l^{-1}(t)\psi_i(1)\psi_j(1)+m_a l^{-2}(t)\dot{l}(t)\psi_i(1)\psi_j(1), \tag{3.51}$$

$$G_{q_{ij}}(t)=\rho l^{-1}(t)\dot{l}(t)\left[2\int_0^1(1-\xi)\psi_i(\xi)\psi_j'(\xi)d\xi-\delta_{ij}\right], \tag{3.52}$$

$$H_{q_{ij}}(t)=\rho\left[l^{-2}(t)\dot{l}^2(t)-l^{-1}(t)\ddot{l}(t)\right]\left[\frac{1}{2}\delta_{ij}-\int_0^1(1-\xi)\psi_i(\xi)\psi_j'(\xi)\,d\xi\right]. \tag{3.53}$$

where δ_{ij} is the Kronecker delta.

Figure 3.6 shows the boundary control model for travelling cable. A control input $u(t)$ is applied at the point mass m_a for the purpose of suppressing the lateral vibration of the cable. A disturbance force $f(t)$ is applied at a fixed point on the cable, located at $s=l-r$.

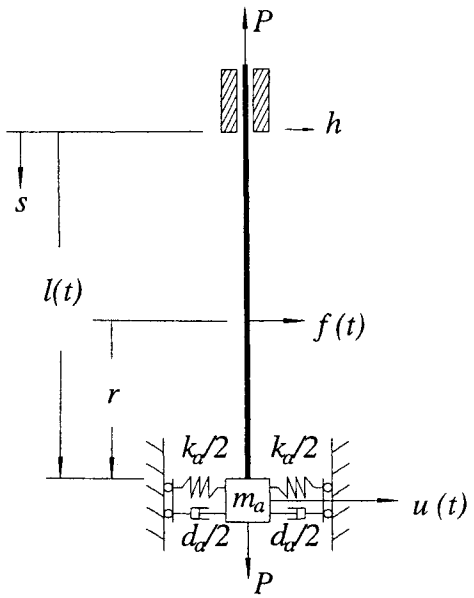

Figure 3.6: Moving cable model with boundary control

From Figure 3.6, equations (3.38) and (3.48) can be expressed as

$$\rho\, w_{tt}(s,t)-\left(\tau(x)w_s(x,t)\right)_s = u(t)\delta\left(s-l(t)\right)+f(t)\,\delta(s-(l(t)-r)),\quad 0<s<l, \tag{3.54}$$

$$M_q(t)\ddot{q}(t)+D_q(t)\dot{q}(t)+K_q(t)q(t)=B_{q1}(t)u(t)+B_{q2}(t)f(t), \tag{3.55}$$

respectively, where $B_{q1}(t)$ is the input vector for the control input and $B_{q2}(t)$ is the input vector for the disturbance, and their elements can be expressed as

$$B_{q1}(t)=\frac{1}{\sqrt{l(t)}}[\psi_1(1)\quad \psi_2(1)\cdots\psi_n(1)]^{\mathrm{T}}, \tag{3.56}$$

$$B_{q2}(t)=\frac{1}{\sqrt{l(t)}}\left[\psi_1\left(1-\frac{l(t)-r}{l(t)}\right)\quad \psi_2\left(1-\frac{l(t)-r}{l(t)}\right)\cdots\psi_n\left(1-\frac{l(t)-r}{l(t)}\right)\right]^{\mathrm{T}}, \tag{3.57}$$

Equation (3.55) can be written into a state-space representation

$$\begin{aligned}\dot{x}(t)&=A(t)x(t)+B_1(t)u(t)+B_2(t)f(t)\\ y(t)&=C(t)x(t)\end{aligned}, \tag{3.58}$$

where the state vector is

$$x(t)=\begin{bmatrix}q(t)\\ \dot{q}(t)\end{bmatrix}, \tag{3.59}$$

$$A(t)=\begin{bmatrix} 0_{n\times n} & \mathrm{I} \\ -M_q(t)^{-1}\left(K_q(t)+H_q(t)\right) & -M_q(t)^{-1}\left(D_q(t)+G_q(t)\right) \end{bmatrix}, \tag{3.60}$$

the input matrices are

$$B_1(t)=\begin{bmatrix} 0_{n\times 1} \\ M_q(t)^{-1}B_{q1}(t) \end{bmatrix}, \tag{3.61}$$

$$B_2(t)=\begin{bmatrix} 0_{n\times 1} \\ M_q(t)^{-1}B_{q2}(t) \end{bmatrix}, \tag{3.62}$$

Similar to the stationary model, the outputs of the system can be the lateral displacement $w_a(l(t),t)$ or the lateral velocity $\dot{w}_a(l(t),t)$ of the actuator. The displacement $w_a(l(t),t)$ and the lateral velocity $\dot{w}_a(l(t),t)$ of the actuator can be expressed as

$$w_a(l(t),t)=\sum_{j=1}^{n} C_{1j}(t)q_j(t), \tag{3.63}$$

$$\dot{w}_a(l(t),t)=\sum_{j=1}^{n}\left(C_{2j}(t)q_j(t)+C_{1j}(t)\dot{q}_j(t)\right), \tag{3.64}$$

where $C_1(t)$ and $C_2(t)$ are $1\times n$ vectors, and their elements are given by

$$C_{1j}(t)=g_y\frac{1}{\sqrt{l(t)}}\psi_j(1), \tag{3.65}$$

$$C_{2j}(t)=g_y\frac{\dot{l}(t)}{l(t)}\frac{1}{\sqrt{l(t)}}\psi_j(1). \tag{3.66}$$

Therefore, if the displacement of the actuator is used as the output $y(t)$, the output matrix $C(t)$ can be expressed as

$$C(t)=[C_1(t)\quad 0_{1\times n}]. \tag{3.67}$$

If the velocity of the actuator is used as the output $y(t)$, the output matrix C can be expressed as

$$C(t)=[C_2(t) \quad C_1(t)]. \tag{3.68}$$

3.2.2 Travelling Cable Dynamics

To better understand the dynamics of the travelling cable with a varying length, mathematical simulations have been done. The parameters used here are the same as those in Section 2.1.2. Two scenarios were considered. Scenario A: axial extension in which the cable travels from $l = l_{short}$ to $l = l_{long}$; Scenario B: axial retraction in which the cable travels from $l = l_{long}$ to $l = l_{short}$, where $l_{long} = 1.5346\ m$ and $l_{short} = 0.6064\ m$. The cable travel is assumed to have a trapezoidal velocity profile. Figure 3.7 shows the motion profiles of the travelling cable.

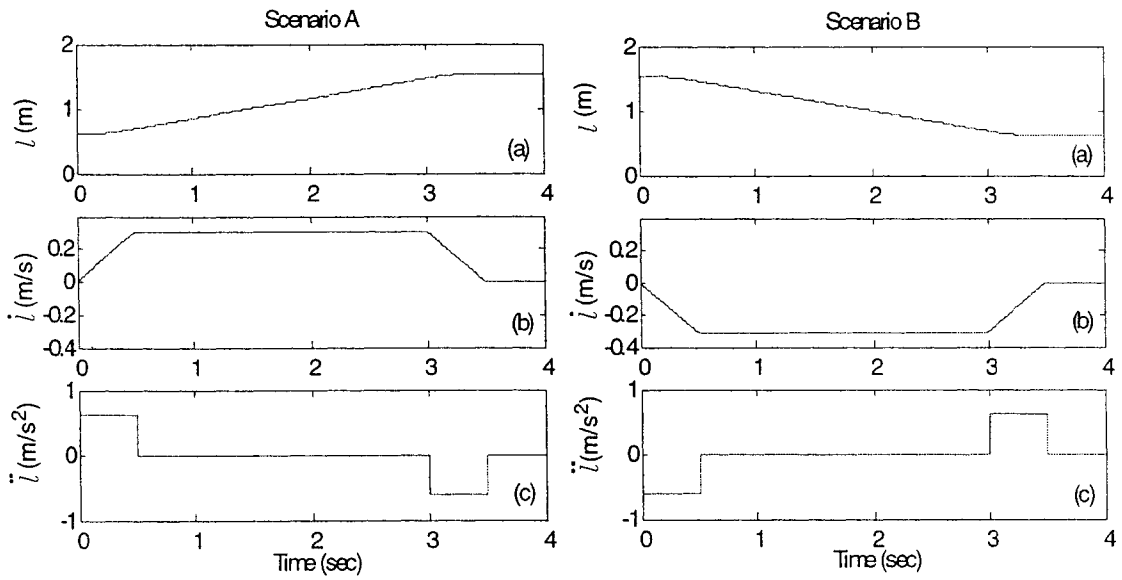

Figure 3.7: The motion profiles of the travelling cable. (a) Displacement l, (b) Velocity $\dot{l}$, (c) Acceleration $\ddot{l}$.

The maximum absolute travelling velocity $\dot{l}$ and acceleration $\ddot{l}$ are 309.4 mm/s and 618.8 mm/s^2, respectively. The initial displacements for both scenarios are described in Figure 3.8, and the initial velocities are set to zero. The concentrated force creates

maximum deflections of the belt $w_{\max} = d_{b\max} = 0.03$ m and the actuator $w_{a\max} = d_{a\max} = 0.003$. The initial displacement of the cable can be expressed as

$$w(s,0) = \begin{cases} xd_{b\max}/(l(0)-0.498), & 0 \le s \le l(0)-0.498, \\ d_{b\max} + [s-(l(0)-0.498)](d_{a\max} - d_{b\max})/0.498, & l(0)-0.498 \le s \le l(0). \end{cases} \quad (3.69)$$

Figure 3.8 shows the initial displacement profiles of the travelling cable.

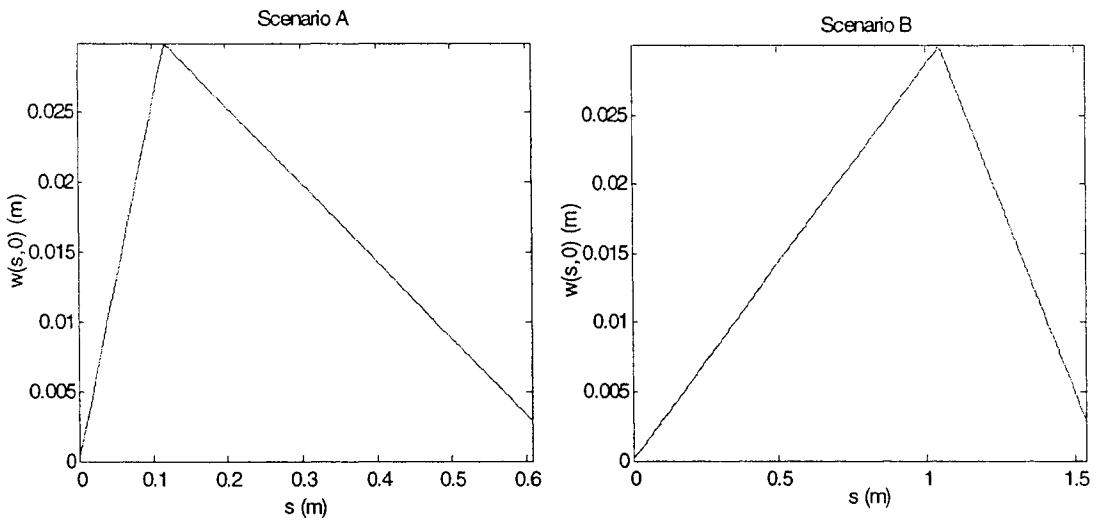

Figure 3.8: The initial displacement profile

The total simulation time is set to 4 sec, in which the total cable travelling period is 3.5 sec. Simulation results are based on a fixed particle on the cable, located at $s = l(0) - 0.498$ m. Figures 3.9 to 3.11 show the simulation results for both scenarios.

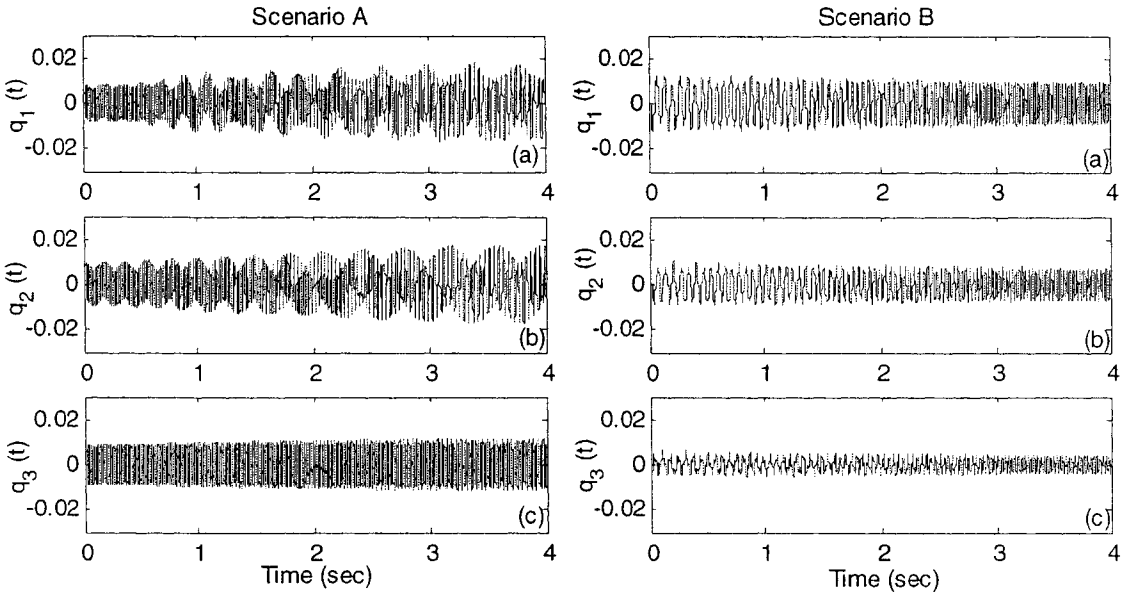

Figure 3.9: The generalized coordinates q of the travelling cable. (a) First mode, (b) Second mode, (c) Third mode.

Figure 3.9 shows the responses of the generalized coordinates of the travelling cable. From Figure 3.9, a few observable facts can be noted. First, the oscillating frequencies of the generalized coordinates are decaying in Scenario A, but increasing in Scenario B. Second; the magnitudes of the generalized coordinates are increasing in Scenario A. For Scenario B, the magnitudes of the generalized coordinates are decaying slightly during the cable-travelling period. Third, the magnitudes of the third mode for both scenarios are smaller than those of the first and second modes. The first two observations can be explained by the variation of the cable's stiffness. Axial extension reduces the stiffness of the cablehence makes the cable more flexible. It also increases the total mass of the cable. The effects combine to lower vibrating frequency of the cable.

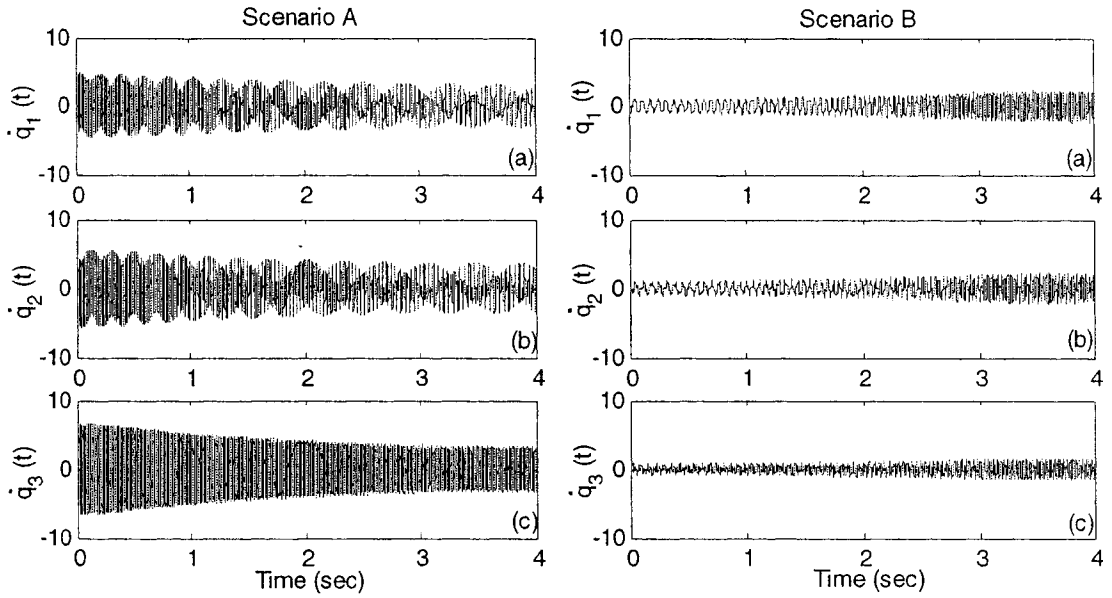

Figure 3.10: The generalized velocities of the travelling cable. (a) First mode, (b) Second mode, (c) Third mode.

Figure 3.10 shows the responses of the generalized velocities of the travelling cable. Here, the magnitudes of the generalized velocities are decaying in Scenario A, but increasing in Scenario B. A conclusion can be drawn from the simulation results of the generalized coordinates and velocities. The axial extension should make the cable vibrate at a higher oscillating magnitude and lower oscillating rate. The axial retraction should make the cable vibrate at a faster oscillating rate.

The effect on the oscillating magnitude from the axial extension is further investigated from the lateral displacements and velocities simulation results. The lateral displacements and velocities for both scenarios are simulated and shown in Figure 3.11. The results are based on a fixed particle on the cable located at $x = l(0) - 0.498\,\text{m}$.

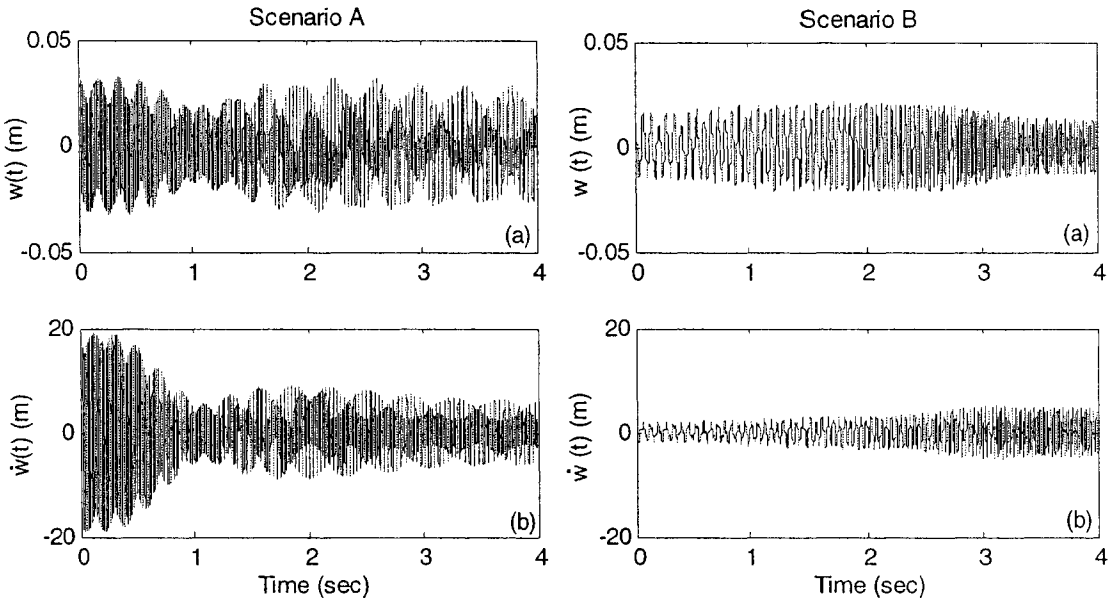

Figure 3.11: The undamped responses of the travelling cable. (a) Lateral displacement w, (b) Lateral velocity $\dot{w}$.

Figure 3.11 shows the responses of the lateral displacement and the velocity of the travelling cable. From Figure 3.11, the dynamics of the cable are as expected in Scenario A with the axial extension increasing the flexibility of the cable. An interesting trend is observed in Scenario B. The amplitude of the lateral displacement increases first and decreases near the end of the cable-travelling period, which is a typical "unstable shortening" behaviour.

3.3 Summary

Mathematical models are developed to study the dynamics of a travelling cable with variable length. Two stationary cable models with different boundary conditions and a travelling cable model are developed. The models for the boundary force control are also developed. State space representation of the stationary and travelling cable models are presented for the purpose of developing boundary control strategies in the future. The relationship between the axial tension and the natural frequencies are determined. The

natural frequencies of the stationary models are used to verify the experimental testing results. The free vibration simulations demonstrate the dynamics of the travelling cable with a varying length.

Chapter 4

PRELIMINARY TESTING RESULTS OF THE EXPERIMENT SYSTEM

To better understand the dynamics of the travelling cable apparatus and the actuator, a preliminary testing has been done. LabView programs were developed to implement the test. The rest of the chapter is organized as follows: Section 4.1 examines the natural frequencies of stationary cable with different boundary conditions, Section 4.2 calculates the stiffness and damping ratio of the plate spring, Section 4.3 discusses the procedure and results of controlling the position of the DC motor, Section 4.4 presents the free vibration of the travelling cable, Section 4.5 examines the relationship between the magnitude of the actuator acceleration and the voltage applied to the actuator, Section 4.6 examines the functionality of the strain gauges installed on the plate spring, and Section 4.7 contains the conclusions.

4.1 Natural Frequencies of the Stationary Cable

A LabView program was used to experimentally determine the natural frequencies of the stationary cable. Three boundary conditions were considered. Condition 1: fixed-fixed boundary condition; Condition 2: fixed-spring-constrained boundary condition without placing the permanent magnets; Condition 3: fixed-spring-constrained boundary

condition with the permanent magnets placed as designed. The first two boundary conditions refer to the mathematical models expressed in Section 3.1.1. The third boundary condition is examined to see the effects from the permanent magnets. For each boundary condition, two cable lengths, namely l_{long} and l_{short}, were considered. l_{long} was the maximum length of the cable when the travelling blocks were at their lowest position and l_{short} was the length of the cable when the travelling blocks were at a higher position. The spectrums of free responses of Conditions 1, 2, and 3 are shown in Figures 4.1, 4.2, and 4.3, respectively.

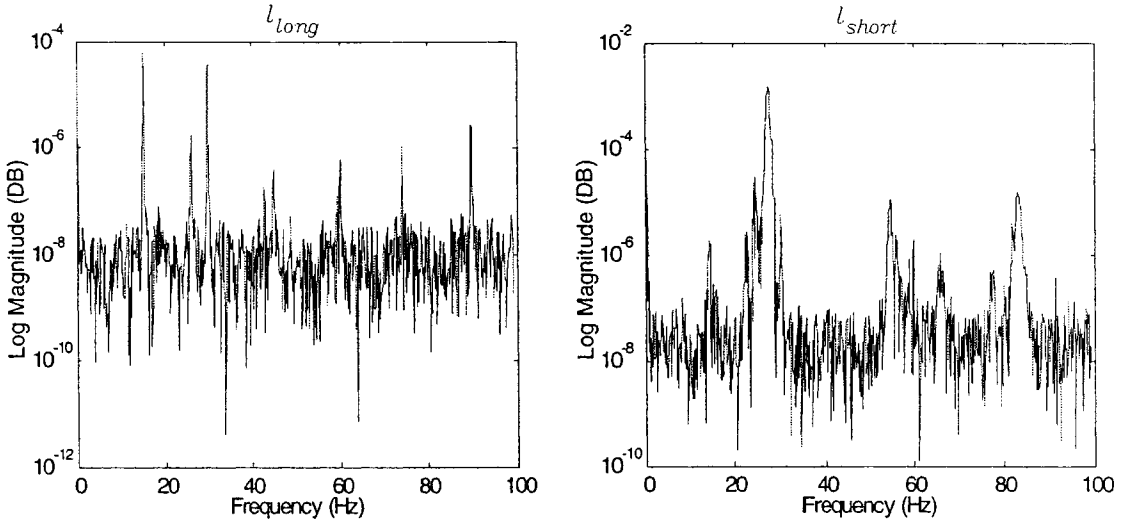

Figure 4.1: Response Spectrum (Condition 1)

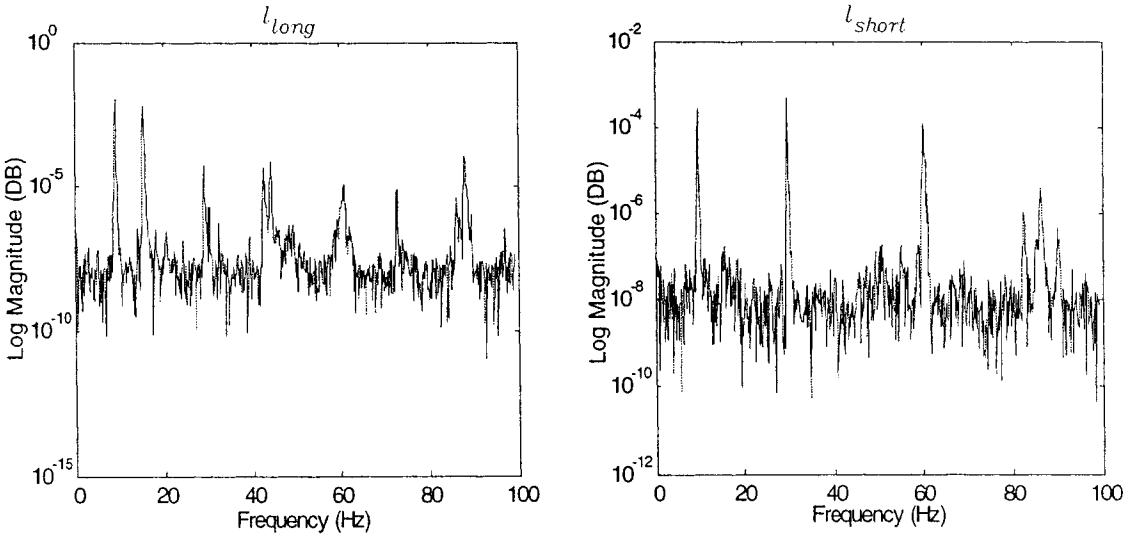

Figure 4.2: Response Spectrum (Condition 2)

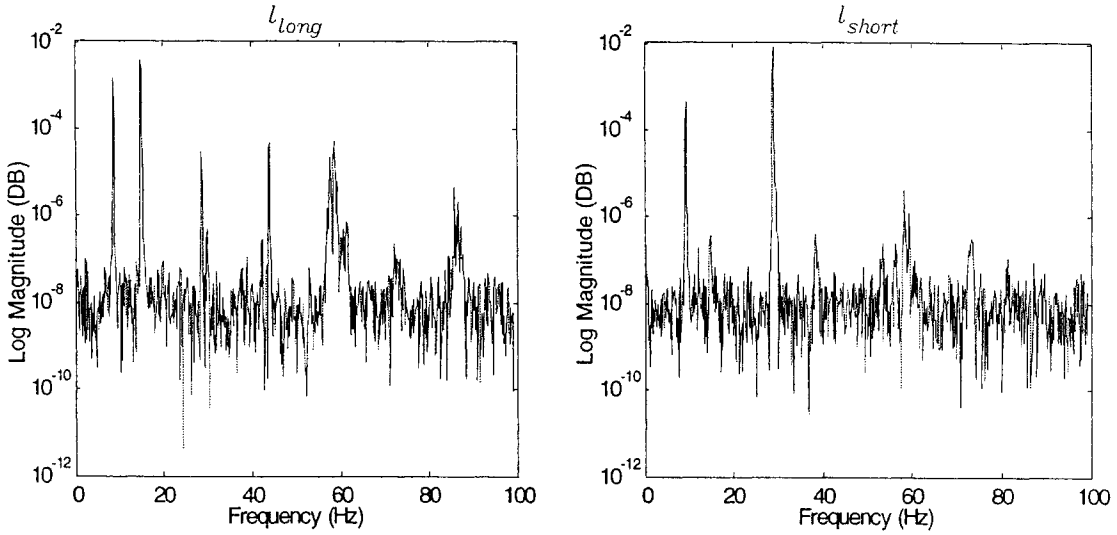

Figure 4.3: Response Spectrum (Condition 3)

The natural frequencies for Condition 1 were used to determine the tension of the belt, as mentioned in Section 3.1.2. A pattern of response spectrum is found by examining Figure 4.1. The first three natural frequencies of the cable at $l = l_{long}$ for condition 1 should be 14.9, 29.8, and 44.7 Hz. From Table 3.2, it is observed that the first three calculated natural frequencies at $l = l_{short}$ are in agreement with the experimental results as well. From Figure 4.2, the first and third natural frequencies are close to the values obtained analytically at both lengths. The first three natural frequencies of each condition with different cable lengths are listed in Table 4.1. Clearly, presence of the permanent magnets reduces the natural frequencies of the system slightly.

	1st mode	2nd mode	3rd mode
$l = l_{long}$			
Condition 1	14.88	29.77	44.65
Condition 2	8.91	15.14	29.05
Condition 3	8.79	15.01	28.93
$l = l_{short}$			
Condition 1	27.83	54.44	83.13
Condition 2	9.64	30.29	60.06
Condition 3	9.28	29.05	58.23

Table 4.1: Experimentally determined natural frequencies

4.2 Stiffness and Damping Coefficient of the Actuator

Free responses of the actuator were used to calculate the stiffness and damping coefficient of the plate spring. The electromagnet was connected to the plate spring only. An impact was applied to the electromagnet to excite free response. The accelerometer was placed on the electromagnet, as indicated in Figure 2.2. The spectrum analysis was conducted on the free vibration response. Two set-ups were considered. Set-up 1: the free vibration responses without the permanent magnets placed; Set-up 2: the actuator with the permanent magnets placed as designed. The stiffness k_a of the actuator is determined by using the equation of natural frequency given by

$$\omega_a = \sqrt{k_a / m_a} \,. \tag{4.1}$$

where is the natural frequency of the actuator. The damping coefficient d_a is determined by using the damping ratio equation given by

$$d_a = 2\varsigma_a \sqrt{k_a m_a} \,, \tag{4.2}$$

where ς_a is the damping ratio of the actuator. The damping ratio can be determined from the concept of logarithmic decrement, denoted by λ and defined by

$$\lambda = \ln \frac{\alpha(t)}{\alpha(t+T)}, \tag{4.3}$$

where $\alpha(t)$ is the measured response and T is the period of the oscillation. The damping ratio ς can be found by solving

$$\varsigma = \frac{\lambda}{\sqrt{4\pi^2 + \lambda^2}}. \tag{4.4}$$

The accelerometer readings of free vibration responses and the spectrums for both cases are plotted in Figure 4.4.

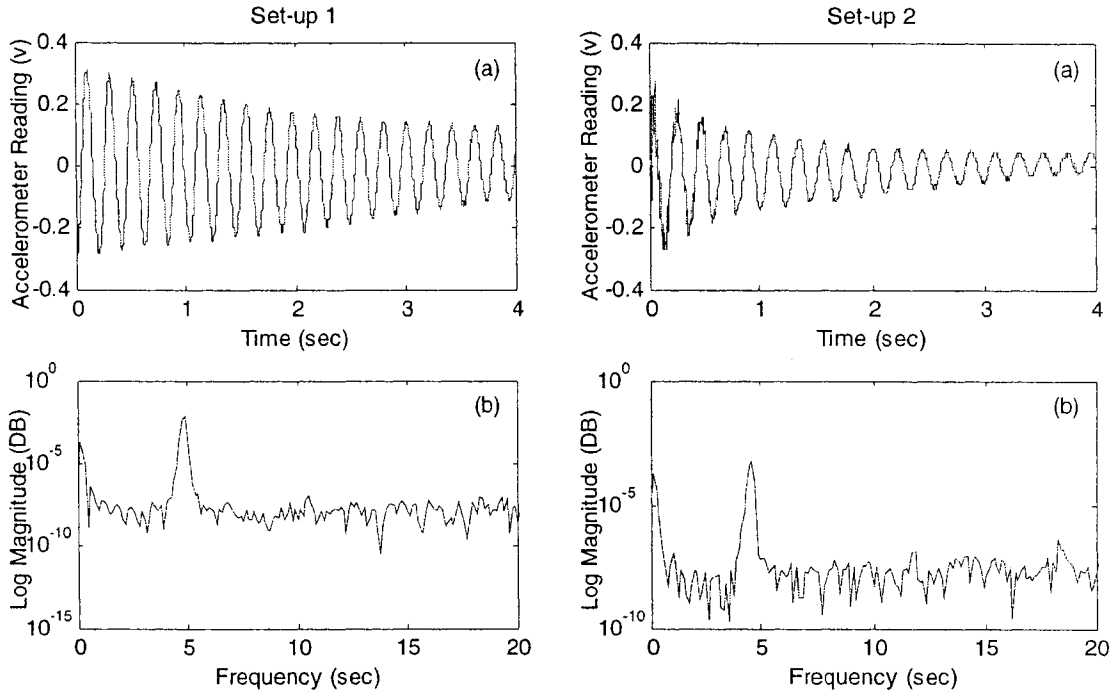

Figure 4.4: Free response spectrum of the actuator. (a) Acceleration signal, (b) Spectrum.

As shown in Figure 4.4, the system of Set-up 2 exhibits greater damping effect. Values of the stiffness and the damping coefficient for both scenarios are calculated and listed in Table 4.2.

	ω (Hz)	k_a (N/m)	ζ	d_a (Ns/m)
Scenario 1	4.88	755	0.0116	0.82
Scenario 2	4.64	682	0.0306	2.16

Table 4.2: Stiffness and damping coefficient of the plate spring

As expected, the system of Set-up 2 has greater damping effect. The magnetic field created by the two permanent magnets attracts the steel rod of the electromagnet and increases the magnitude of the vibration, which explains the lower stiffness in Scenario 2. It is also noted that the natural frequency is lower than the value obtained by treating the actuator as a cantilever beam with an end mass. The gravity force of the electromagnet creates an inverted pendulum effect to lower the effective stiffness of the system.

4.3 Testing of the Actuator

Relationship between magnitude of the actuator acceleration and voltage applied to it was determined experimentally. A LabView program was developed to create a sine wave signal. The signal was sent to the current control circuit through a digital to analog channel to regulate the magnitude and direction of the current of the electromagnet. Frequencies of 9.5 and 13 Hz were considered as the frequencies of the sine wave signal. The amplitude of the sine wave was set to 2.75 volt. Figure 4.5 shows the input voltage versus the acceleration reading of the actuator under 9.5 and 13 Hz exciting frequencies.

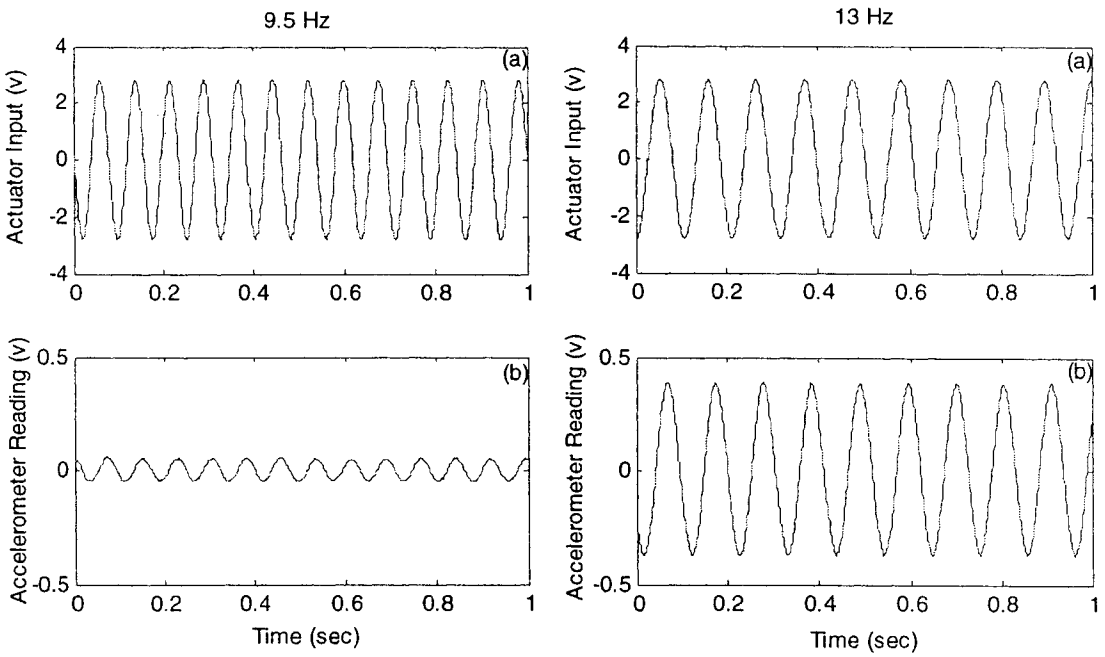

Figure 4.5: Accelerations versus input voltages. (a) Input signals, (b) Measured acceleration signals.

From Figure 4.5, the relationship between the input voltage and the acceleration of the actuator can be observed. The maximum acceleration occurs at the middle of the voltage-alternating period. With the same magnitude of input voltages, the maximum acceleration of the actuator under exciting frequency of 9.5 Hz is much lower than the maximum acceleration of the actuator under exciting frequency of 13 Hz. The above observation

can be explained by the natural frequencies of the system. When a system is excited at a frequency close to its natural frequencies, the system response is close to resonance.

Another experiment was carried out to examine the natural frequencies. With the magnitude of the voltage set to a constant, a sine wave signal was used to excite the actuator. The exciting frequencies were swept through 6 Hz to 30 Hz at a step of 0.25 Hz. The 30 Hz upper limit was set because the physical responses over 30 Hz were too small to detect. For each step, the steady-state amplitude of the acceleration signal was measured. The accelerometer was placed at a position 300 mm above the lower end of the band. Figure 4.6 shows the amplitude of the acceleration signals versus the exciting frequencies for both lengths.

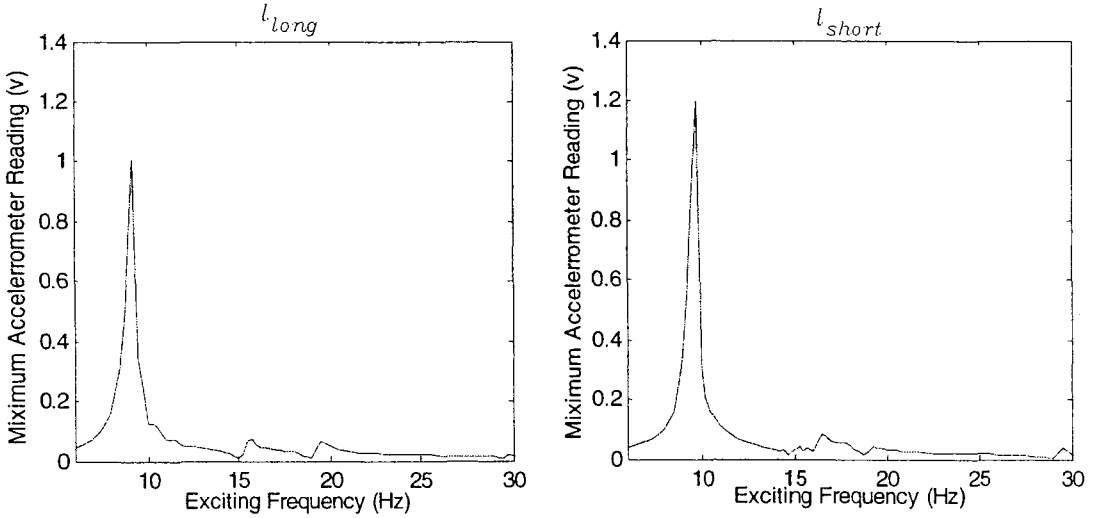

Figure 4.6: Maximum acceleration of the actuator versus the exciting frequencies

From Figure 4.6, a few obsevable facts can be seen. For $l = l_{long}$, the first and last peaks are the first and third natural frequencies. Two peaks exist at exciting frequencies 15.75 Hz and 19.5 Hz. The difference between the responses under this two exiting frequencies was observed visually during the sweeping frequency experiment. When the exciting frequency was set to 16.25 Hz, the actuator was vibrating laterally. When the exciting frequency was set to 19.25 Hz, a torsional vibration was observed. For $l = l_{short}$, the first

and last peaks are the first and second natural frequencies. A peak is found at frequency of 16.5 Hz, which is observed to be the response of the torsional vibration as well. The incorrect experimental results can be explained as follow. First, the type of the sensor used has a major effect. Generally, an accelerometer detects the acceleration of an object in one axis only; and this axis is dependent on how the accelerometer is placed. Second, it is impossible to constrain the vibration of the belt to its lateral direction completely.

4.4 Testing of the Strain Gauge

Strain gauges were installed on the plate spring to measure the lateral displacement of the actuator. Because strain gauge measurement involves sensing extremely small changes in resistance, a Wheatstone full bridge circuit is commonly used to amplify the signal. For this study, a full-bridge configuration, shown in Figure 4.7, with four active gauges was developed.

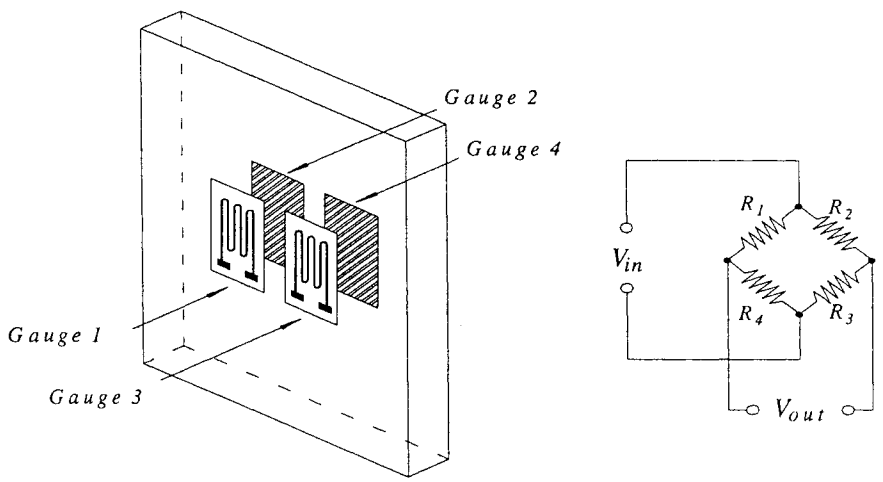

Figure 4.7: Wheatstone full bridge configuration

The output voltage of the Wheatstone full bridge will be equal to:

$$V_{out} = V_{in}\left(\frac{R_3}{R_3 + R_2} - \frac{R_2}{R_1 + R_4}\right). \tag{4.5}$$

Electrical environments often make strain gauge signal noisy. Also, it is very unlikely that the bridge will output exactly zero volts when no strain is applied. Tuning the variable resistor in the strain gauge signal amplifier solved the offset problems. A low pass filter with 30 Hz cut-out frequencies was designed to remove the high frequencies signal received from the strain gauge signal amplifier. A testing of the strain gauges installed was conducted and the results are shown in Figure 4.8.

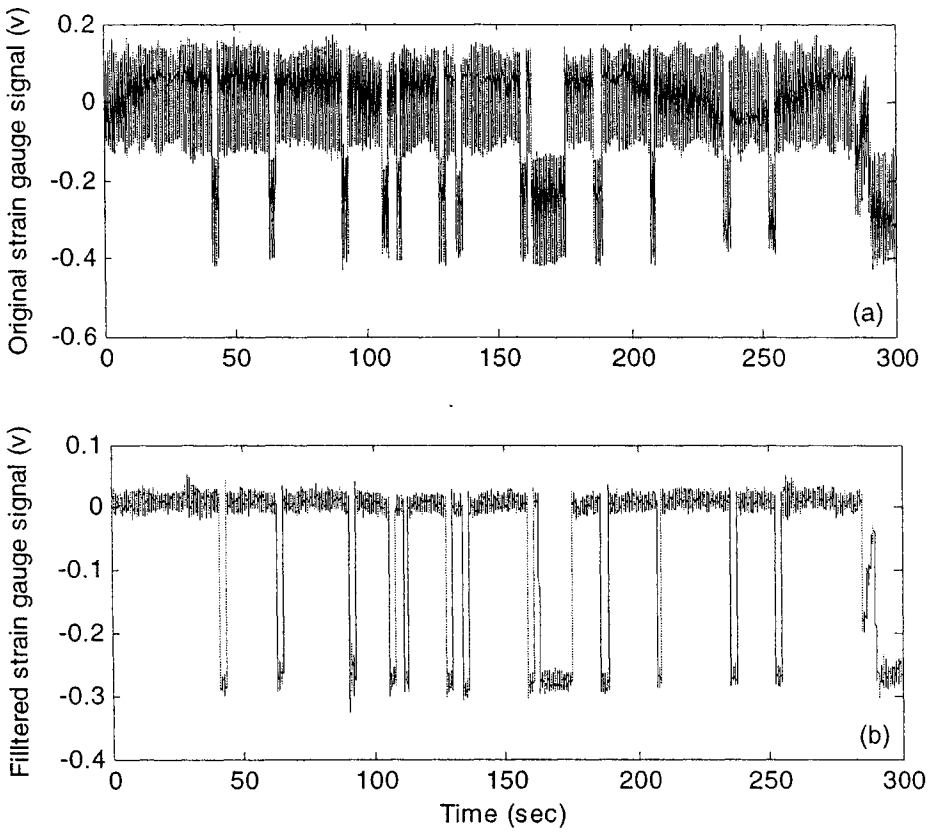

Figure 4.8: Strain gauges testing results. (a) Original strain gauge signal, (b) Filtered strain gauge signal.

From Figure 4.8, the magnitude of the noise is greatly reduced by the low pass filter; and the offset of the signal is zero. However, the amplifier used to condition the strain gauge signal is not stable. Therefore, the strain gauge signal cannot be used especially for the purpose of feedback control.

4.5 DC Motor Position Control

A simple proportional feedback control was used for control of the DC motor. A desired motion was prescribed which has a trapezoidal velocity profile. The relation between the cable length and the potentiometer reading was determined as follows. Every volt increase in the potentiometer reading indicates a 618.8 mm decrease of the cable length. With this relation, the desired length change at each moment was converted into a setpoint. The motor control command proportional to the error between the setpoint and the potentiometer reading was sent to the servo linear amplifier through a digital to analog channel to regulate the current to the motor. Two scenarios were considered. Scenario A: axial extension in which the potentiometer reading changes from 2.5 volts to 1 volt; Scenario B: axial retraction in which the potentiometer reading changes from 1 volt to 2.5 volts. The maximum absolute travelling velocity was set to 309.4 mm/s, and the duration of the acceleration or the deceleration was set to 0.25 sec. The value of the feedback gain was 80. The total sampling time for the experiment was 6 sec, and the sampling rate was 1000 scans/s. A comparison between the desired position profiles and the actual position is shown in Figure 4.9. The dotted lines indicate the desired motion profiles; and the solid lines indicate the actual reading from the potentiometer.

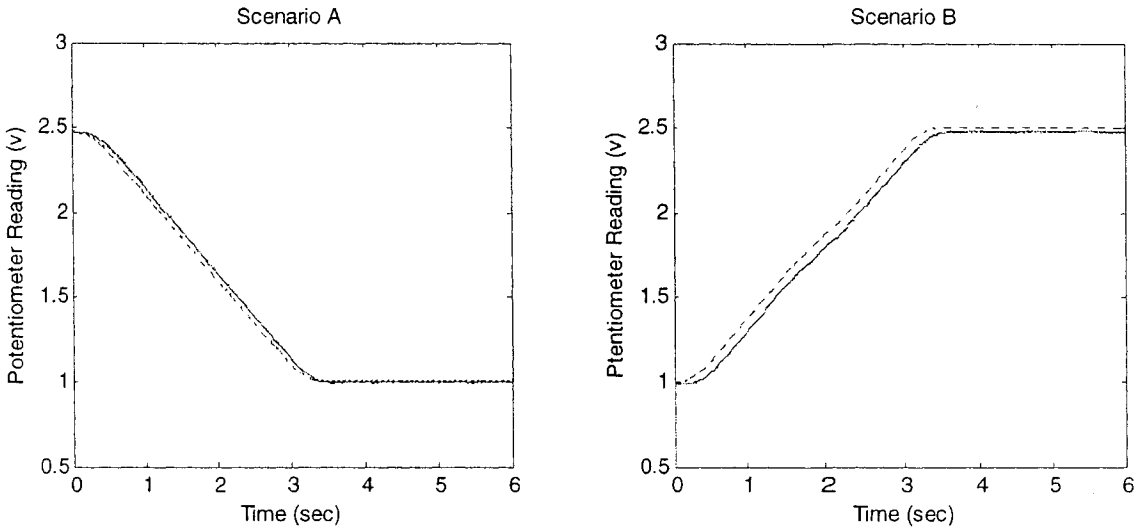

Figure 4.9: DC motor position control

From Figure 4.9, the actual motion profile in each scenario follows the desired motion profile with a small delay and steady-state error, especially in Scenario B. The time delays and steady-state errors can be explained by the limitation of the servo linear amplifier and the design of the proportional feedback gain. The greater driving load during the upward motion can explain the appearances of longer time delays and larger steady error in Scenario B.

4.6 Free Vibration of the Travelling Cable

The accelerometer was placed at a position 498 mm above the lower end of the band. Two boundary conditions were considered. Condition 1: fixed-fixed boundary condition; Condition 2: fixed-spring-constrained boundary condition with the permanent magnets placed as designed. The cable travels up and down in each scenario. In each boundary condition, two scenarios were considered. Scenario A: axial extension in which the potentiometer reading changes from 2.5 volts to 1 volt; Scenario B: axial retraction in which the potentiometer reading changes from 1 volt to 2.5 volts. As soon as the band

was tapped, the motor control was activated. Figures 4.10 and 4.11 show the experimental results of Conditions 1 and 2, respectively.

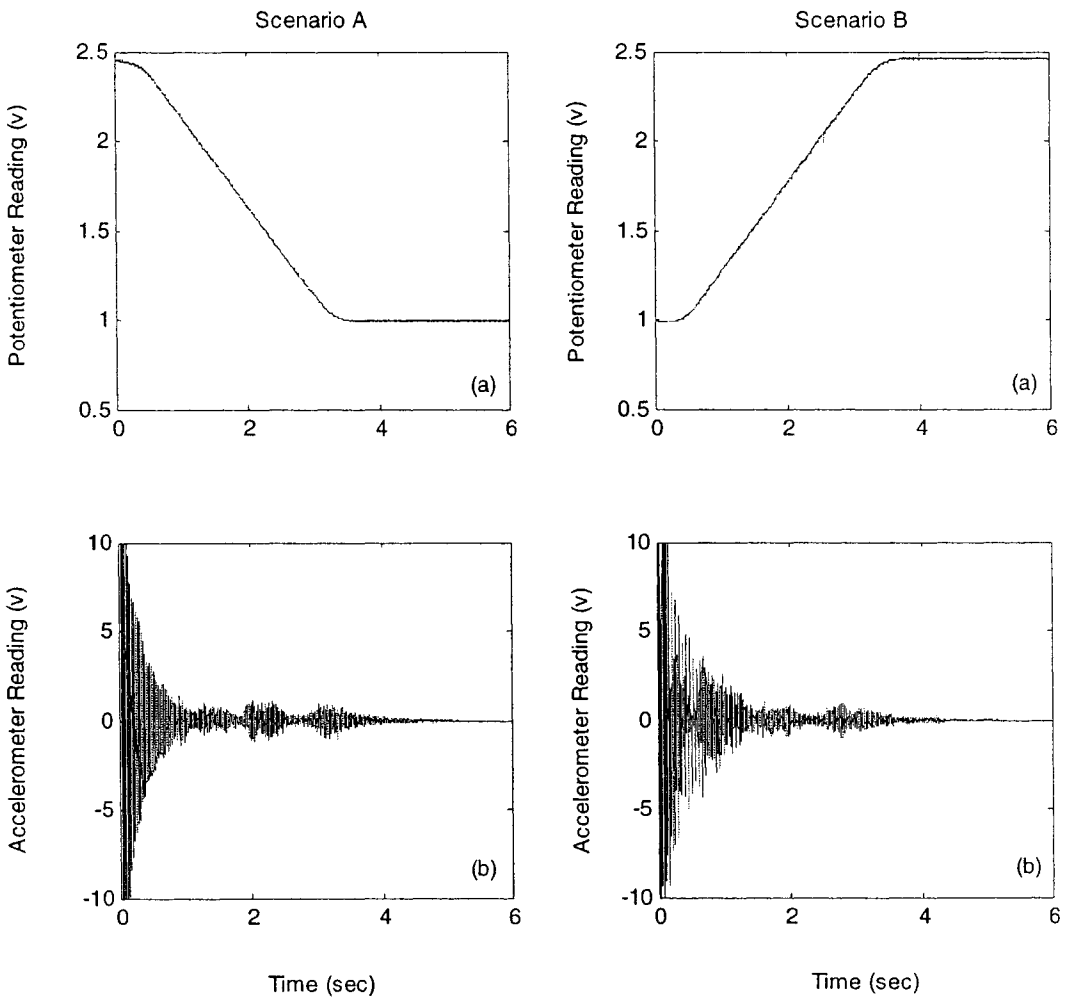

Figure 4.10: Travelling cable with fixed-fixed boundary condition. (a) Cable travelling profile, (b) Free vibration response.

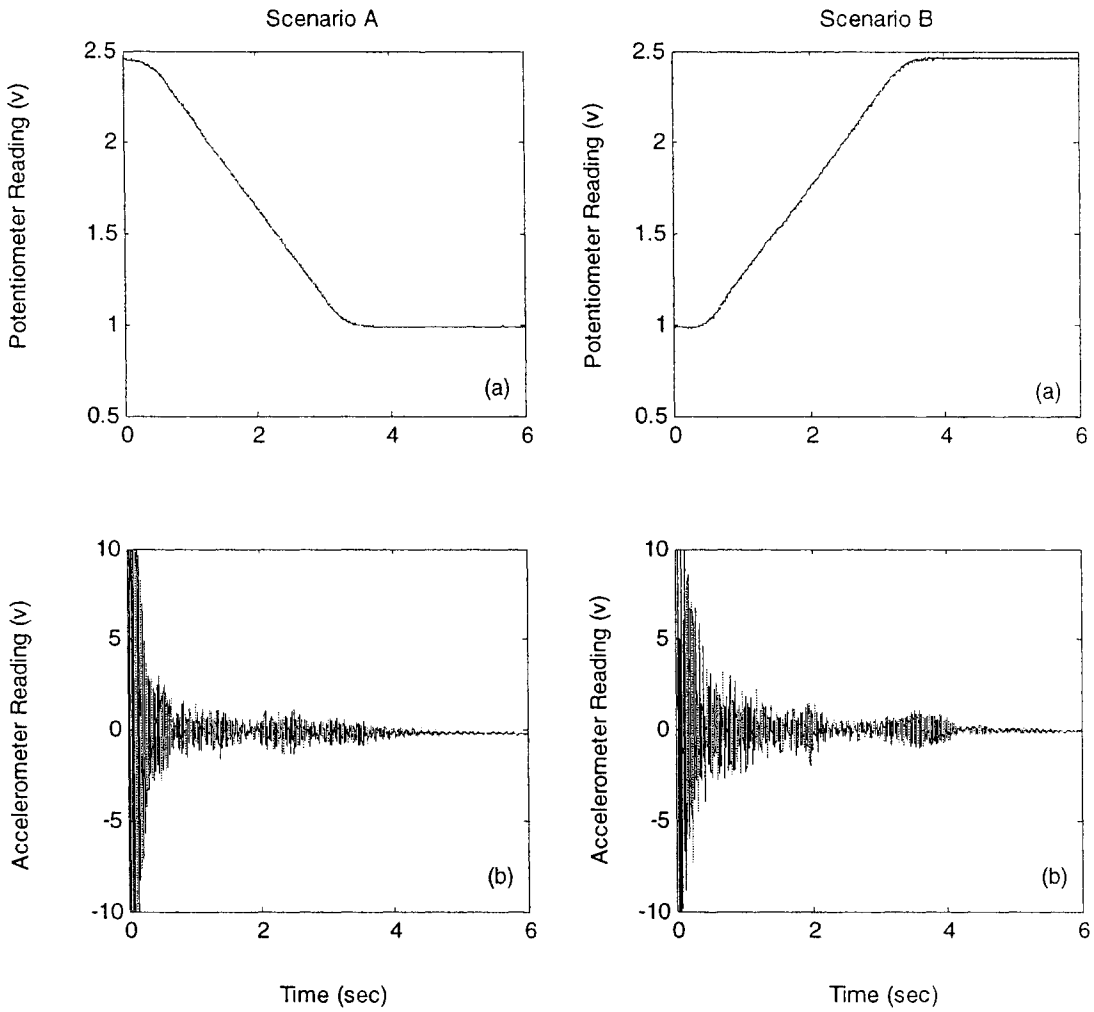

Figure 4.11: Travelling cable with fixed-spring-constrained boundary condition. (a) Cable travelling profile, (b) Free vibration response.

Clearly, a typical "unstable shortening" behaviour occurs as the cable length decreases. Some unexpected increases in the acceleration are founded in Scenario A, which was likely caused by the contact between the belt and the grooves of the pulleys.

4.7 Conclusions

Based on the results presented in this chapter, the following conclusions can be inferred:

1. The natural frequencies obtained experimentaly in the fixed-fixed boundary condition are in better agreement with the analytical results than those obtained for fixed-spring-constrained boundary condition.
2. The magnetic field created by the two permanent magnets apparently has an effect on the dynamics of the system.
3. The actuator functions as expected, which can be used to generate a non-contact force to control the boundary condition of the belt.
4. The quality of the output of the strain gauge amplifier is not acceptable. Thus the strain gauge signal is not suitable for the purpose of feedback control.
5. The greater driving load during the upward motion significantly reduces the performance of the DC motor position control.
6. The experimental results clearly show the unstable shortening effect.

Chapter 5

ACTIVE CONTROL OF THE STATIONARY CABLE

One of the original objectives of this project is to develop an active control system to suppress the vibration of a travelling cable. As mentioned in Chapter 2, in order to drive the cable system a tensioner is designed to increase the friction between the cable and the pulleys. The tension applied will dramatically reduce the magnitude of the cable's free vibration. As shown in Figure 4.11, the free responses of the travelling cable decay quickly even without any control. It is expected that the present system may not be able to demonstrate the effectiveness of any control method. To make the cable vibrate more, the tension needs to be reduced. However, with a smaller tension the cable slips over the pulleys such that travelling up is not possible. This indicates a shortcoming of the present experimental system. This remains a matter to be addressed in future extensions of this research. Limited by the afore-mentioned problem, the rest of the thesis focuses on active control of the stationary cable.

The rest of the chapter is organized as follows: Section 5.1 describes the theory of direct output feedback control method for the stationary cable system and shows some simulation and experimental results, Section 5.2 describes the design of observer-based

feedback control system for the stationary cable system and presents some simulation and experimental results, Section 5.3 is a brief summary.

5.1 Direct Output Feedback

5.1.1 Mathematical Modeling

To control the boundary of the system, a closed loop control system is developed for the purpose of controlling the motion of the actuator shown in Figure 2.2. In general, close-loop systems are designed to obtain more accurate control. In a close-loop system, a well-designed controller will tend to make the error between the actual output and the desired output of the system converge to zero in order to achieve the desired performance of the system. Here, direct output feedback method is first applied. Direct output feedback method directly uses the measured output times a constant gain as the control input to the system to suppress the vibration.

For the stationary cable model, the governing equation is expressed in equation (3.20). The expressions of the system's outputs are stated in equations (3.28) and (3.29), respectively. However, the damping matrix D_q, which is expressed in equation (3.18), and used in equation (3.20), has only considered the damping of the plate spring. In order to model the system more accurately, the damping of the cable has to be considered. Therefore, in the following study, equation (3.18) is rearranged as

$$D_{q_{ij}} = \int_0^l d_b \phi_i(s)\phi_j(s)ds + d_a \phi_i(l)\phi_j(l), \tag{5.1}$$

where d_b is the damping coefficient per length of the cable.

If the feedback is the actuator's lateral displacement $w_a(l, t)$, equation (3.20) can be rearranged as

$$M_q \ddot{q}(t) + D_q \dot{q}(t) + K_q q(t) = -B_{q1} p_d w(l, t) + B_{q2} f(t), \tag{5.2}$$

where p_d is a constant gain multiplied to the displacement. Substituting equation (3.28) into equation (5.2), the governing equation for the direct displacement feedback model can be expressed as

$$M_q \ddot{q}(t) + D_q \dot{q}(t) + \left(K_q + B_{q1} C_1 p_d\right) q(t) = B_{q2} f(t). \tag{5.3}$$

Since K_q is the stiffness matrix for model B, equation (5.3) clearly shows the displacement feedback can be used to enhance the stiffness of the system. If the control input $u(t)$ is the actuator's lateral velocity $\dot{w}(l, t)$, equation (3.20) can be rearranged as

$$M_q \ddot{q}(t) + D_q \dot{q}(t) + K_q q(t) = -B_{q1} p_v \dot{w}(l, t) + B_{q2} f(t), \tag{5.4}$$

where p_v is a constant gain multiplied to the velocity. Substituting equation (3.29) into equation (5.4), the governing equation for the direct velocity feedback model can be expressed as

$$M_q \ddot{q}(t) + \left(D_q + B_{q1} C_1 p_v\right) \dot{q}(t) + K_q q(t) = B_{q2} f(t). \tag{5.5}$$

Since D_q is the damping matrix for model B, equation (5.5) indicates the velocity feedback can improve the damping of the system.

5.1.2 System Identification

Since the experimental apparatus has been adjusted for demonstrating the control effects, some of the parameters used for the stationary cable model have to be changed accordingly. Of all the new parameters, the easiest to determine is the length of the cable. However, other parameters are not readily available. One of the approaches is to make the natural frequencies of the mathematical model as close to those of the experimental system as possible.

Once again the LabView program was used to experimentally determine the natural frequencies of the stationary cable system, as described in Section 4.2. Three set-ups were considered. Condition 1: natural frequencies of the actuator along; Condition 2: natural frequencies of the cable along; Condition 3: natural frequencies of the combined system including the cable and the actuator. The accelerometer readings of free vibration responses and the responses spectrums for Condition 2 are shown in Figure 4.4. The accelerometer readings of free vibration responses and the responses spectrums for Conditions 1 and 3 are shown in Figure 5.1.

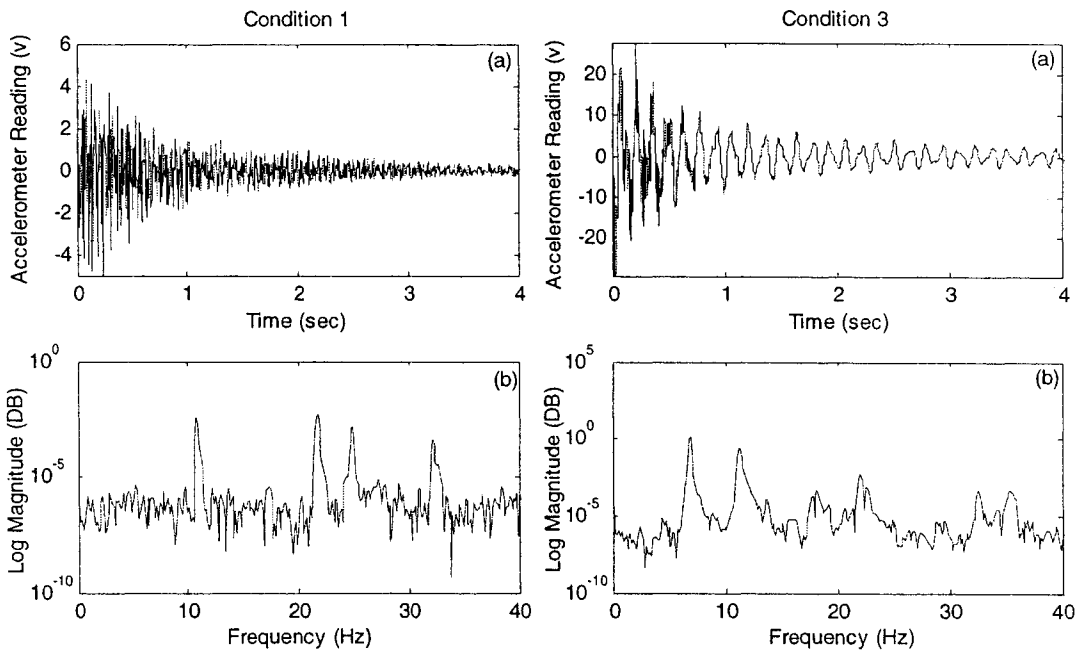

Figure 5.1: Free vibration and responses spectrums for Condition 1 and 3. (a) Acceleration signal, (b) Spectrums.

The natural frequencies for all conditions are listed in Table 5.1.

	1st mode	2nd mode	3rd mode
Condition 1	11.12	21.73	32.23
Condition 2	4.88	N/A	N/A
Condition 3	6.96	11.23	21.97

Table 5.1: Natural frequencies of the stationary cable system

From Table 5.1, the following observations are inferred:

- The first natural frequency of the combined system is mainly influenced by the actuator.
- The second and third natural frequencies of the combined system are mainly associated with the first and second modes of the cable itself, respectively.

The above observations indicate that changing the tension p of the cable and the stiffness k_a of the plate spring can modify the natural frequencies of the stationary model. If the values p and k_a used in the mathematical model are 35.82 N and 1555 N/m, respectively, the first three natural frequencies of the stationary cable model become 6.9589 Hz, 11.2311 Hz, and 22.5073 Hz, which are sufficiently closed to those of the experimental system.

The damping coefficient of the actuator is assumed to be the same. The damping coefficient of the belt is determined by tuning the mathematical model's second mode damping ratio same as the experimental damping ratio of Condition 1. The procedures used to determine the damping ratio have been described in Section 4.2. From the free vibration response of Condition 1, the experimental damping ratio of the cable is determined to be 0.04. If the damping coefficient d_b used for the mathematical model is 0.175, the damping ratio of the second mode for the stationary cable model becomes 0.04. Parameters used for direct feedback control are listed in Table 5.2.

l (m)	$\rho\left(kg/m\right)$	$m_a(kg)$	$k_a\left(N/m\right)$	$d_a\left(N\cdot s/m\right)$	$d_b\left(N\cdot s/m^2\right)$	g_y
1.844	0.03	0.803	1555	0.778	0.175	1

Table 5.2: Parameters used for the direct feedback control model.

5.1.3 Controllability

Before applying any control to any system, the system has to be first determined as uniformly controllable. In theory, a system is said to be controllable if every state variable of the process can be controlled to reach a certain objective in finite time interval by some unconstrained control input $u(t)$.

Mathematically, the controllability of a time-invariant system can be determined by checking the rank of the system's controllability matrix [31]. Equation (3.23) shows the state-space representation for the stationary cable model. The controllability matrix for the stationary cable model can be expressed as

$$P_c = \left[B_1 \; AB_1 \; \ldots \; A^{n-1}B_1\right]. \tag{5.6}$$

If the rank of the controllability matrix is the same with the number of the states, the system is completely controllable. From equation (3.24), if three modes are considered, the number of the states should be six. The rank of the controllability matrix is determined to be six as well; therefore, the system is uniformly controllable.

5.1.4 Simulation Results

To observe the effects of direct displacement and velocity feedback methods, computer simulations have been implemented. The mathematical model used for simulation is described in Section 3.1.1. All parameters used are listed in Table 5.2. The initial conditions for the cable have been described in equation (3.69). Two locations were considered for observation. Location 1: the sensor is placed on the actuator; Location 2: the sensor is placed 0.489 m above the actuator. Different values of p_d and p_v are used to verify the results. Both the lateral velocity and displacement responses are simulated. Figures 5.2 and 5.3 show the direct displacement feedback control simulation results.

Figures 5.4 and 5.6 show the direct velocity feedback control simulation results. To compare the control effects, the dotted lines indicate the uncontrolled responses; and the solid lines indicate the controlled responses.

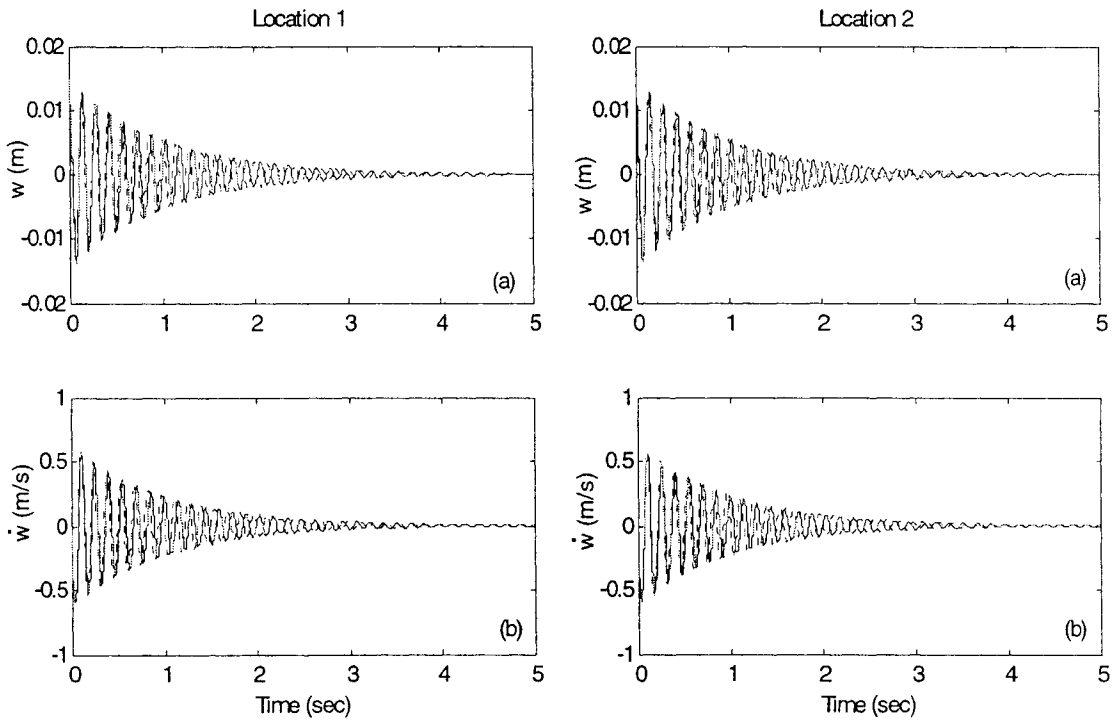

Figure 5.2: Direct displacement feedback control simulation results (p_d = -100). (a) Lateral displacement, (b) Lateral velocity.

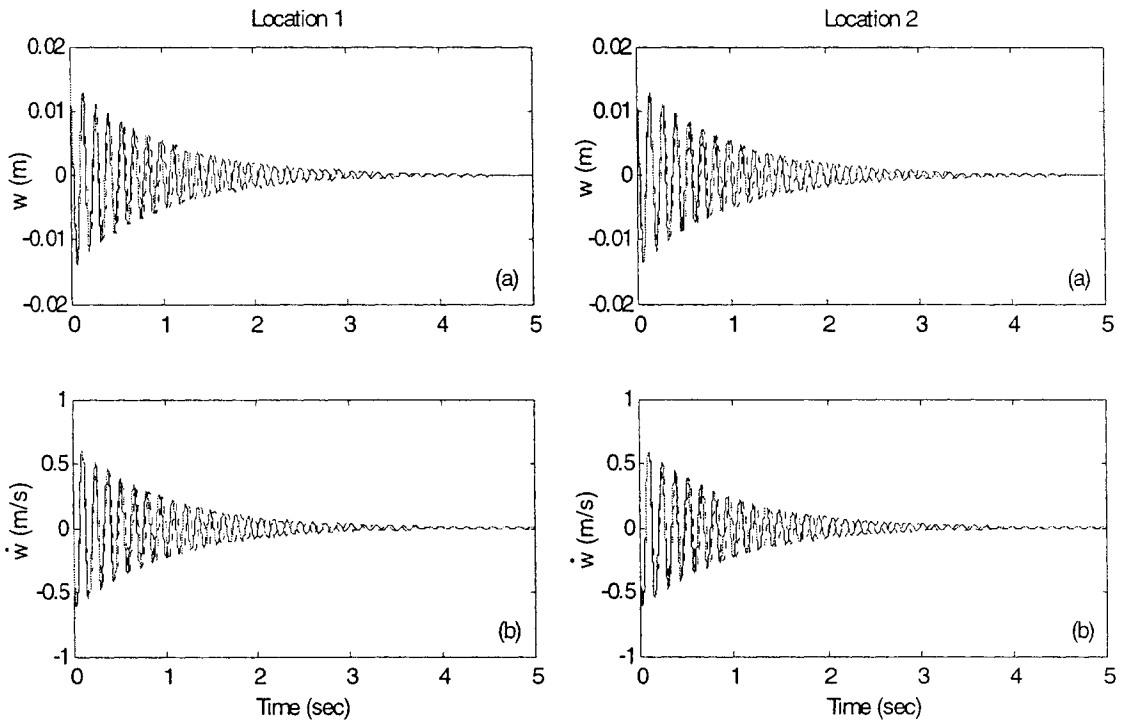

Figure 5.3: Direct displacement feedback control simulation results (p_d = 100). (a) Lateral displacement, (b) Lateral velocity.

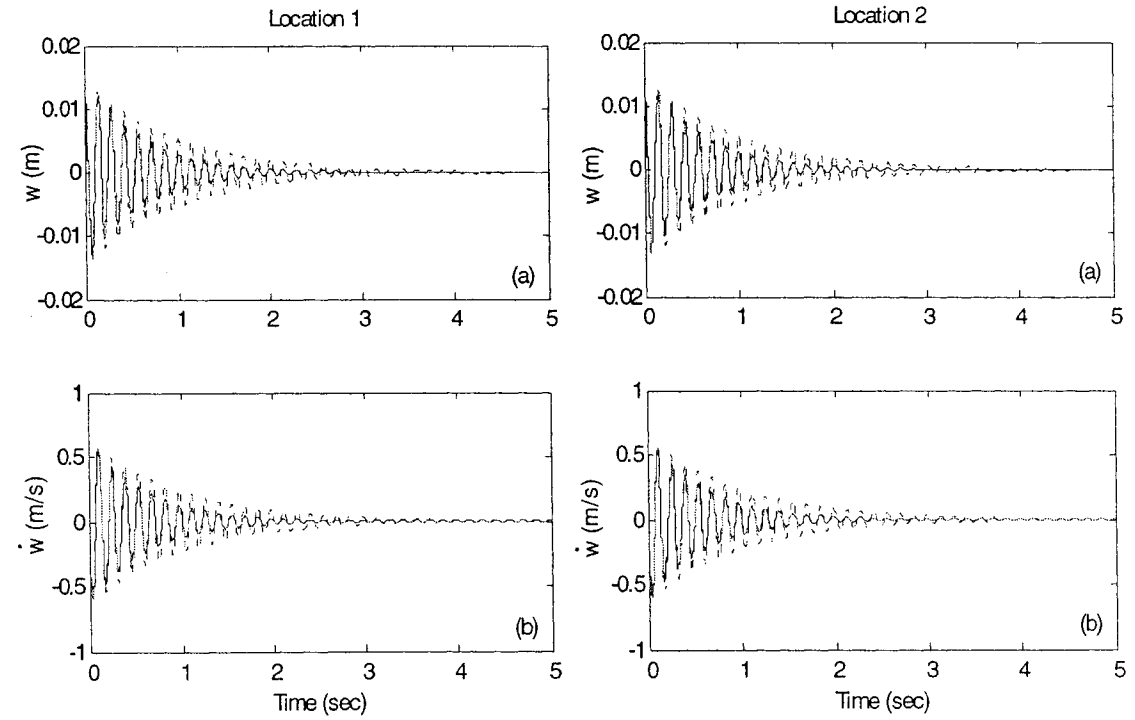

Figure 5.4: Direct velocity feedback control simulation results (p_v = 1). (a) Lateral displacement, (b) Lateral velocity.

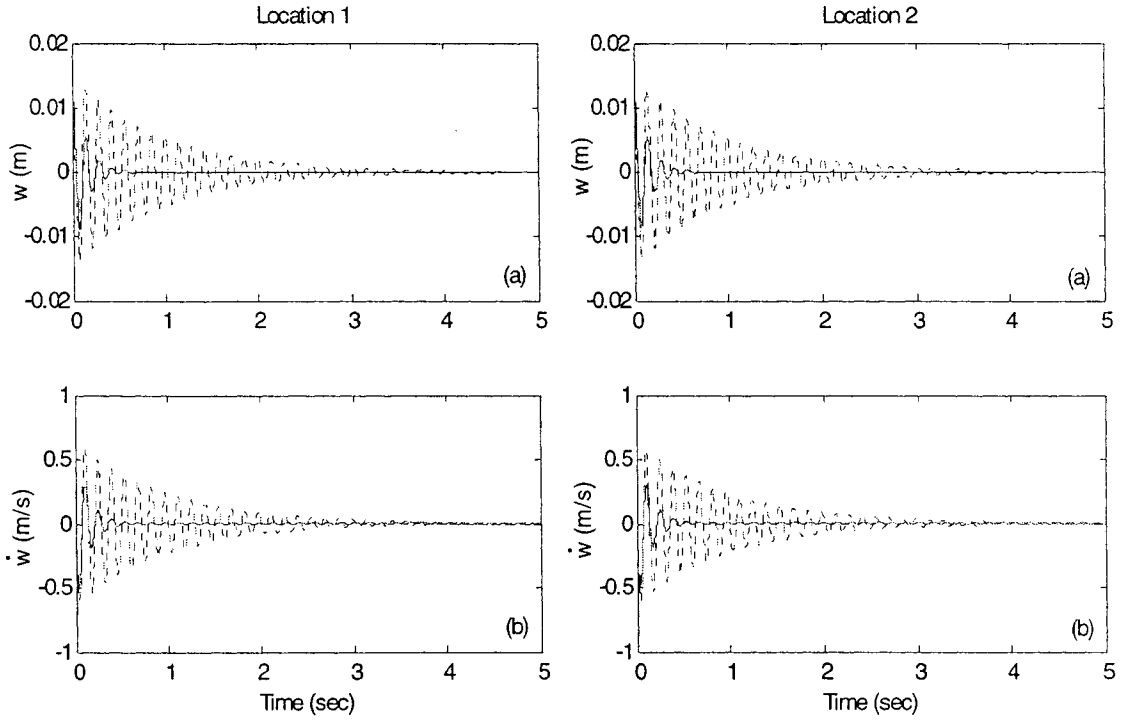

Figure 5.5: Direct velocity feedback control simulation results (p_v = 10). (a) Lateral displacement, (b) Lateral velocity.

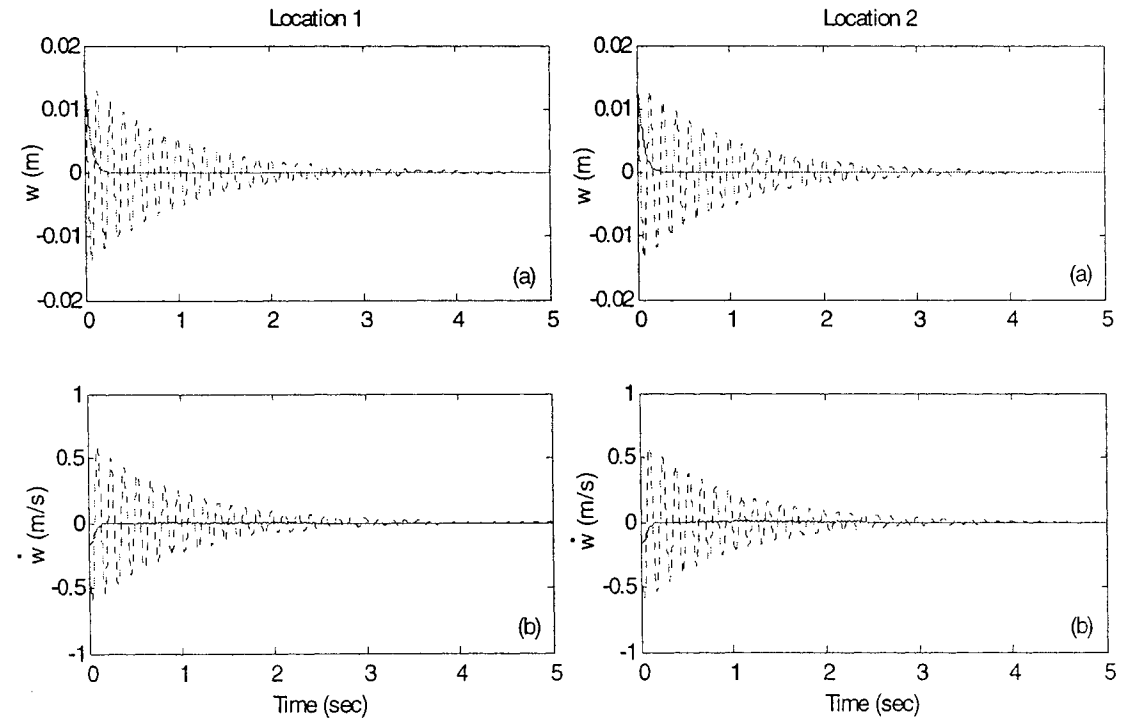

Figure 5.6: Direct velocity feedback control simulation results (p_v = 100). (a) Lateral displacement, (b) Lateral velocity.

From Figures 5.2 to 5.6, the following observations are inferred:

- By controlling the boundary (Location 1), the lateral vibration at Location 2 is controlled.
- The direct displacement feedback method changes the stiffness of the system. The system becomes more flexible when the feedback gain p_d was set to –100. The system becomes stiffer when the feedback gain p_d was set to 100. However, the direct displacement feedback method has little effect on the vibration magnitude.
- The direct velocity feedback method performed as expected; the damping ratio of the system is increased. The higher the value of the feedback gain p_v the better the control.

5.1.5 Experimental Results

The direct velocity feedback method is implemented experimentally. An accelerometer was placed as shown in Figure 2.2 to measure the acceleration of the actuator. The measured acceleration signals were conditioned through the charge amplifier (B & K 2635) before the signals were used for control purpose. The upper and lower frequency limits of the charge amplifier were set to 100 Hz and 2 Hz, respectively. The charge amplifier has three modes of operation, linear (acceleration), single integration (velocity), and double integration (displacement). However, the magnitudes of the velocity signals from the charger amplifier are too large, which increases the difficulty of controlling the vibration at higher mode and creates unstable phenomenon. Therefore, a numerical integration of the acceleration signal was employed. A LabView program was developed to implement the control. In the program, the measured acceleration signals first went through a low-pass filter with a cut-off frequency of 30 Hz and a numerical integration

process. Then, the signals were multiplied by the feedback gain p_v and passed to a digital to analog channel to control the actuator system. An initial displacement was created in the cable at about 0.489 m above the actuator. The scan rate of the program was 500 scans per second. Different values of p_v were used. To compare the control effects, the dotted lines indicate the uncontrolled velocity measurements and the solid lines indicate the controlled velocity measurements. Figures 5.7 to 5.10 show the results.

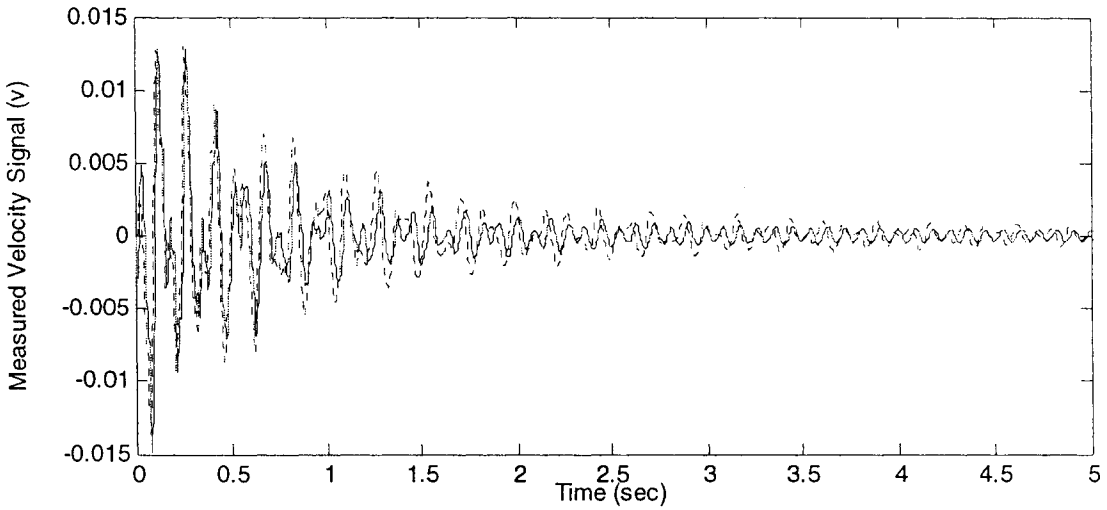

Figure 5.7: Direct velocity feedback control experimental results ($p_v = 100$)

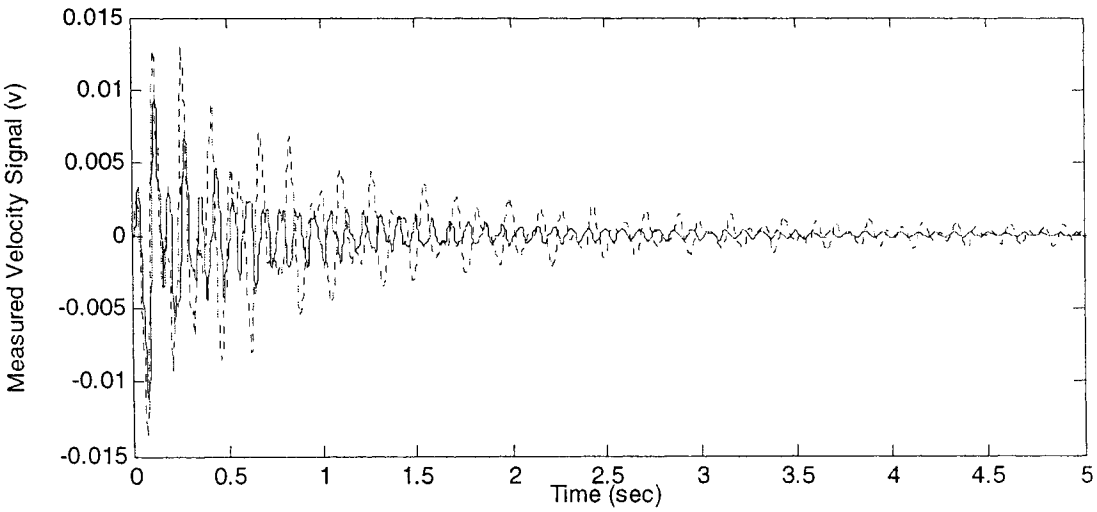

Figure 5.8: Direct velocity feedback control experimental results ($p_v = 500$)

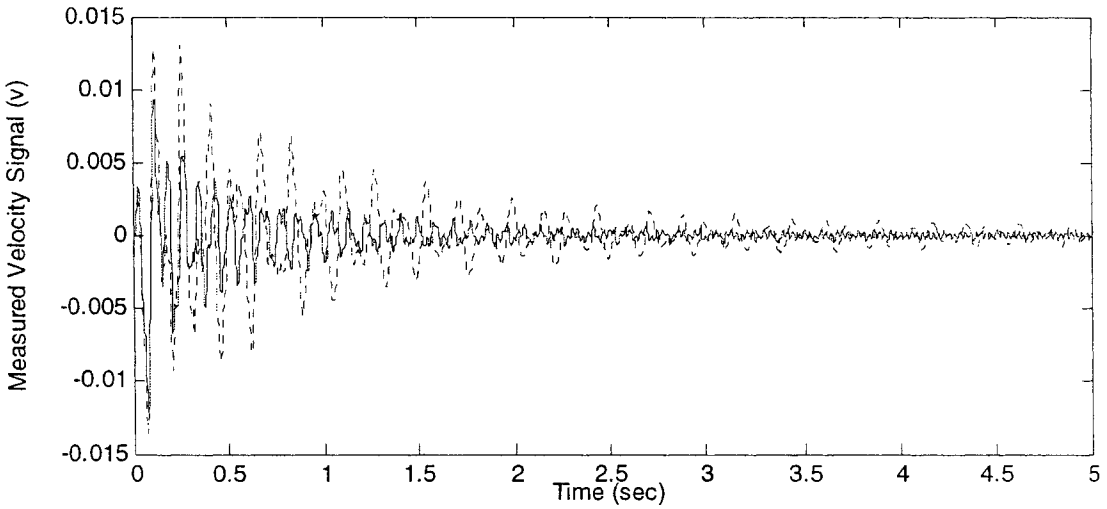

Figure 5.9: Direct velocity feedback control experimental results ($p_v = 800$)

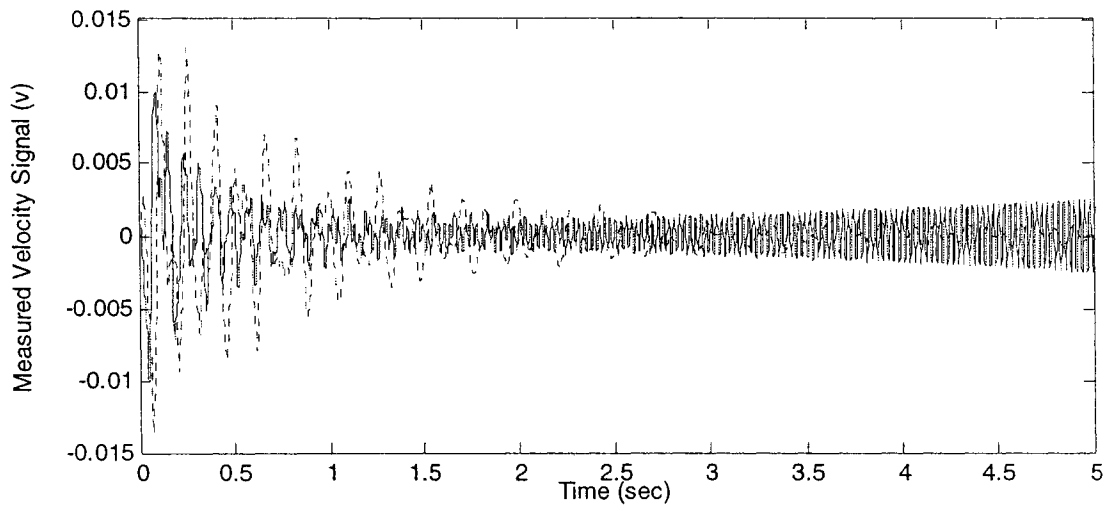

Figure 5.10: Direct velocity feedback control experimental results ($p_v = 1000$)

From Figures 5.7 to 5.10, the following conclusions are drawn:

- With a proper feedback gain p_v, the vibration of the boundary can be suppressed. The direct velocity feedback control is capable of suppressing the cable vibration.
- For the real control system, there is a limit for the feedback gain p_v. A high feedback gain will amplify the noise contained in the measurement, which increases the difficulty of controlling the vibration at higher mode and creates unstable phenomenon.

5.2 Observer-Based Feedback Control

5.2.1 Control Algorithm

The state variables of the system are the generalized coordinates and velocities of the cable. Apparently, the generalized coordinates and velocities are not measurable for the closed loop feedback purposes. The only available measurements are the lateral velocity and displacement of the actuator. The major advantage of observer-based feedback control is that a full-state feedback can be implemented without actually measuring the states. The observer control system model includes a plant and a state observer. Here, the plant represents the stationary cable system. The state observer is able to estimate the state variables based on the measurements of the outputs. Once the state observer estimates the state variables of the real system, full-state feedback control can be applied to control the plant.

Without considering the disturbance force, the model of the plant can be derived into a state-space representation as

$$\begin{aligned} \dot{x}(t) &= Ax(t) + B_1 u(t) \\ y(t) &= Cx(t) \end{aligned} \tag{5.7}$$

The mathematical model for the observer can be written as

$$\begin{aligned} \dot{\hat{x}}(t) &= A\hat{x}(t) + B_1 u(t) + L_g\left(y(t) - \hat{y}(t)\right) \\ \hat{y}(t) &= C\hat{x} \end{aligned} \tag{5.8}$$

where $\hat{x}(t)$ is the estimated state vector, $\hat{y}(t)$ is the estimated output, and L_g is the observer feedback gain matrix. From equation (5.8), the inputs to the observer are the measured output $y(t)$ and control input $u(t)$. By combining equations (5.7) and (5.8), the error between the estimated state and actual state can be expressed as

$$\begin{aligned}\dot{\tilde{x}}(t) &= \dot{x}(t) - \dot{\hat{x}}(t) \\ &= (A - L_g C)(x(t) - \hat{x}(t)) \\ &= (A - L_g C)\tilde{x}(t)\end{aligned} \tag{5.9}$$

In theory, if matrix $A - L_g C$ is a stable matrix, the error vector $\tilde{x}(t)$ will converge to zero for any initial error vector $\tilde{x}(0)$. Therefore, the observer feedback gain L_g has to be designed to bring the eigenvalues of matrix $A - L_g C$ to the desired values to make the errors converge to zero. Once the errors converge to zero, the estimated states are said to be the same as the actual states of the model of the plant. To control the plant, the control input $u(t)$ is defined as

$$u(t) = -K_g \hat{x}(t), \tag{5.10}$$

where K_g is the state feedback gain matrix for the plane system. Substituting equation (5.10) into equation (5.7), the state equation can be rearranged as

$$\dot{x}(t) = Ax(t) + B_1(-K_g \hat{x}(t)). \tag{5.11}$$

Once the errors between the estimated output and the real system's output converge to zero, equation (5.11) can be expressed as

$$\dot{x}(t) = (A - B_1 K_g)x(t). \tag{5.12}$$

Then a proper designed state feedback gain K_g can make all state variables converge to zero for any initial vector $x(0)$ in a desired way.

Both the observer feedback gain L_g and the state feedback gain K_g are determined by the Linear-Quadratic Regulator (LQR) method. With the LQR method, an optimal feedback gain is determined such that a performance index is minimized. The performance index is expressed as

$$J = \int_0^\infty (x'Qx + u'Ru)dt, \tag{5.13}$$

where R is a positive-definite real integer and Q a positive-definite (or positive-semidefinite) real symmetric matrix. The values of Q and R are specified and defined with considerations of the trade-off between regulation performance and control effort.

5.2.2 Consideration of the actuator dynamics

Up to now the mathematical model has not included the dynamics of the actuator. To model the actual control system closely, the dynamics of the actuator needs to be considered. The actuator's dynamics can be expressed as

$$L_a \dot{i} + R_a i = v_a, \tag{5.14}$$

where $L_a = 18.2$ mH is the inductance of the actuator, $R_a = 5$ ohm is the resistance of the actuator, v_a is the voltage applied to the actuator. From equation (2.5), the original control input u can be expressed as

$$u = g_u i, \tag{5.15}$$

where is g_u a correction factor expressed as

$$g_u = \frac{2\gamma}{G_{ap}^2}, \tag{5.16}$$

Equation (5.7) is rearranged as

$$\begin{aligned} \dot{\bar{x}}(t) &= \bar{A}\bar{x}(t) + \bar{B}_1 v_a(t) \\ \bar{y}(t) &= \bar{C}\bar{x}(t) \end{aligned}, \tag{5.17}$$

where the state vector is

$$\bar{x}(t) = \begin{bmatrix} q(t) \\ \dot{q}(t) \\ i(t) \end{bmatrix}, \tag{5.18}$$

the system matrix is

$$\overline{A} = \begin{bmatrix} 0_{n\times n} & I_{n\times n} & 0_{n\times 1} \\ -M_q^{-1}K_q & -M_q^{-1}D_q & M_q^{-1}B_{q1}g_u \\ 0_{1\times n} & 0_{1\times n} & -\dfrac{R_a}{L_a} \end{bmatrix}, \tag{5.19}$$

the control input matrices are

$$\overline{B}_1 = \begin{bmatrix} 0_{n\times 1} \\ 0_{n\times 1} \\ \dfrac{1}{L_a} \end{bmatrix}. \tag{5.20}$$

If the displacement of the actuator is used as the output $\overline{y}(t)$, the output matrix $\overline{C}$ can be expressed as

$$\overline{C} = [g_y\phi(l) \quad 0_{1\times n} \quad 0]. \tag{5.21}$$

If the velocity of the actuator is used as the output $\overline{y}(t)$, the output matrix $\overline{C}$ can be expressed as

$$\overline{C} = [0_{1\times n} \quad g_y\phi(l) \quad 0]. \tag{5.22}$$

The values of g_u and g_y need to be determined. A LabView program was developed. The program included a Sub'VI (Virtual Instrument) that implemented the mathematical model through the Runge-Kutta (RK) numerical integration. A sine wave signal was generated and used as the input to the actuator and v_a in the mathematical model (equation (5.17)) within the program. The measured velocity output and simulated one were compared. Then the values of g_u and g_y were adjusted in order to make the simulated outputs as close as possible to the measured ones. After many trials, the selection of $g_u = 3$ and $g_y = 2$ resulted in the best agreement of the simulated outputs and measured ones. Table 5.3 listed the parameters used for the mathematical model.

l (m)	$\rho\left(Kg/m\right)$	$m_a(kg)$	$k_a\left(N/m\right)$	$d_a\left(N^2/m\right)$	$d_b\left(N^2/m^2\right)$	g_u	g_y
1.844	0.03	0.803	1555	0.778	0.175	3	2

Table 5.3: Parameters used for the observer-based feedback control model

Figures 5.11 to 5.15 show the gain selection results. In the figures, the dotted lines represent the measured velocity outputs while the solid lines represent the simulated velocity outputs.

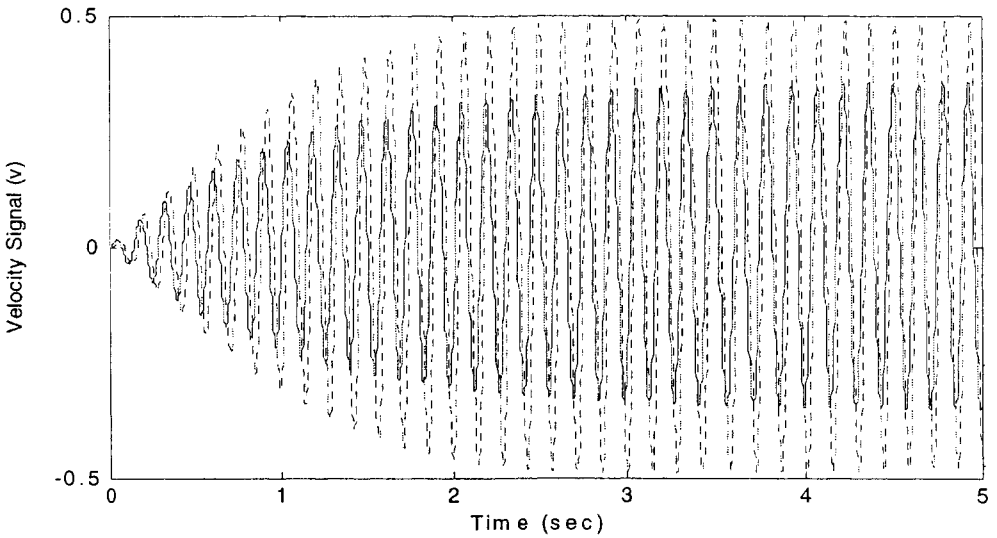

Figure 5.11: Measured and simulated velocity outputs (Sine wave: frequency = 6.95 Hz, amplitude =0.5 V)

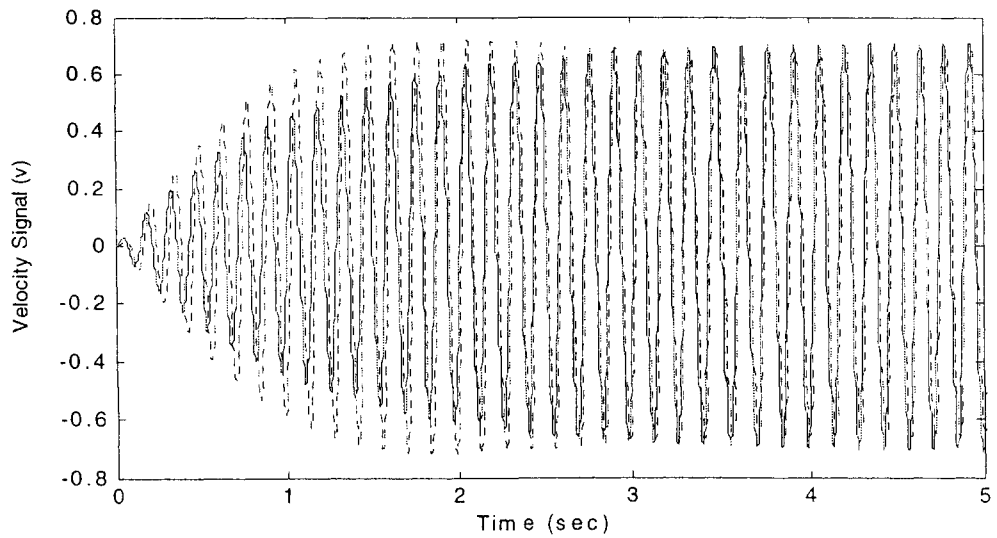

Figure 5.12: Measured and simulated velocity outputs (Sine wave: frequency = 6.95 Hz, amplitude = 1 V)

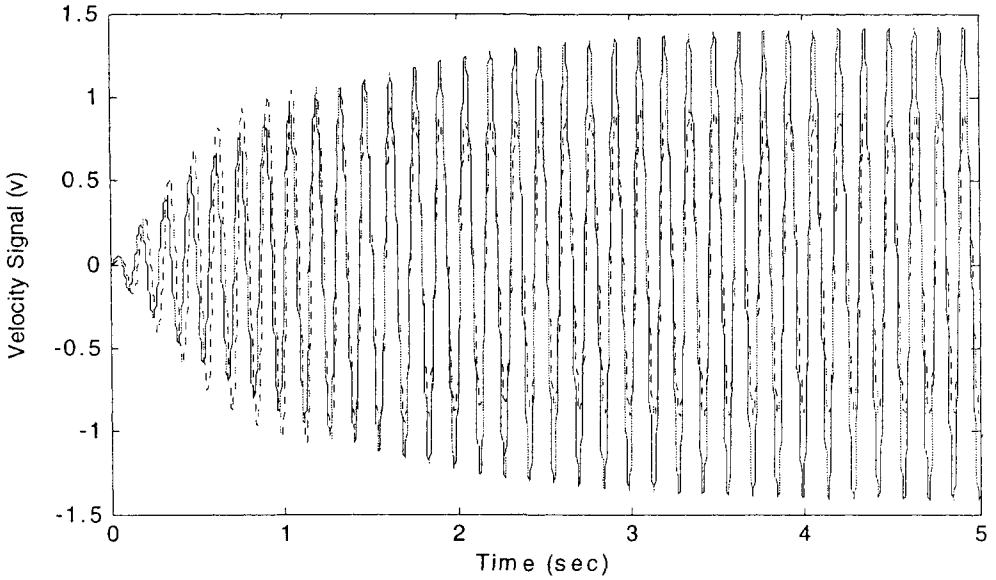

Figure 5.13: Measured and simulated velocity outputs (Sine wave: frequency = 6.95 Hz, amplitude = 2 V)

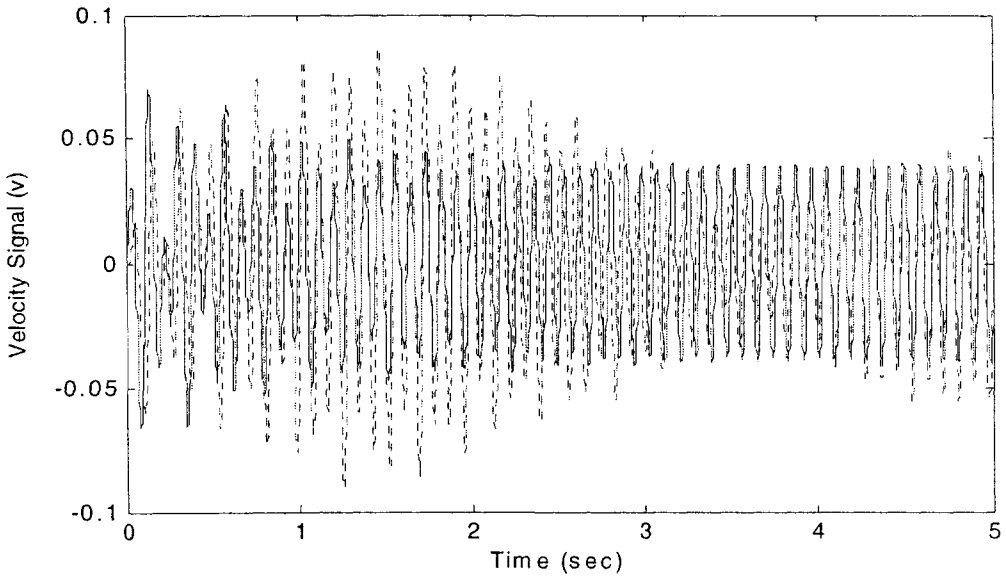

Figure 5.14: Measured and simulated velocity outputs (Sine wave: frequency = 6.95 Hz, amplitude = 1 V).

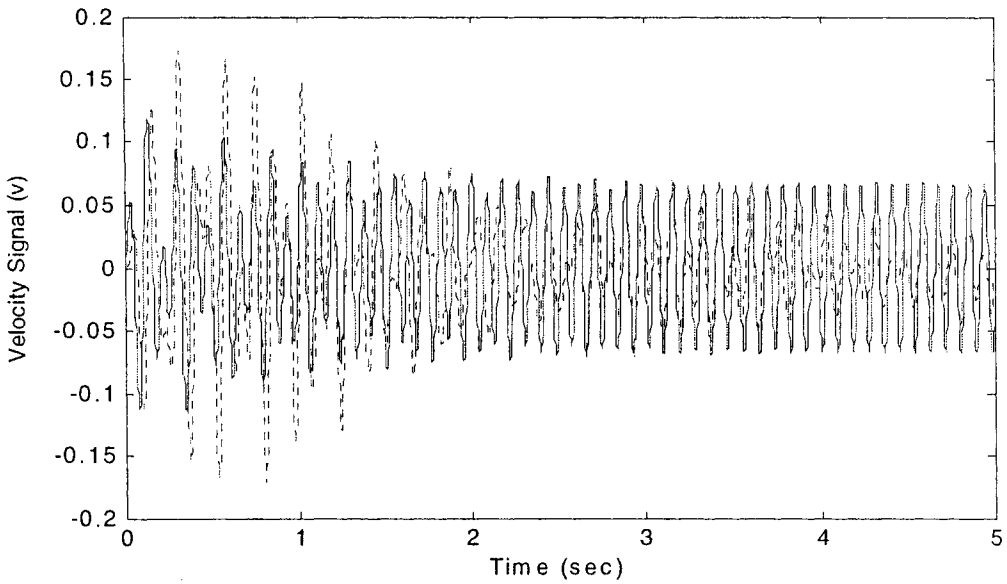

Figure 5.15: Measured and simulated velocity outputs (Sine wave: frequency = 6.95 Hz, amplitude = 2 V).

It can be seen that it is not possible to make the two outputs completely agree one another. However, with the values of $g_u = 3$ and $g_y = 2$, a reasonable agreement exists when the amplitude of the sine signal was 1 V.

5.2.3 Controllability and observability

Before using the LQR method to design the observer feedback gain L_g and the state feedback gain U, the plant system has to be proved as controllable and observable [31]. The controllability matrix for the stationary cable model can be expressed as

$$\overline{P}_c = \left[\overline{B}_1 \ \overline{A}\overline{B}_1 \ \ldots \ \overline{A}^{n-1}\overline{B}_1\right]. \tag{5.23}$$

For the plant system's observability, the system is said to be completely observable if every state can be determined from the observation of system's output over a finite time interval. Mathematically, the observability of a time-invarying system can be determined by checking the rank of the system's observability matrix

$$\overline{P}_o = \begin{bmatrix} \overline{C} \\ \overline{C}\,\overline{A} \\ . \\ . \\ \overline{C}\,\overline{A}^{n-1} \end{bmatrix}. \tag{5.24}$$

If the rank of the observability matrix is the same as the number of the states, the system is proved to be completely observable.

From equation (5.19), if three modes are considered, the number of the states should be seven. The ranks of the controllability and observability matrix are both determined to be seven as well; therefore, the plant system is completely controllable and observable.

5.2.4 Simulation results

Computer simulations have been implemented to investigate the performance of the observer-based control,. From equations (5.4) and (5.8), the dynamics of the observed output feedback control system can be described as

$$\begin{bmatrix} \dot{\overline{x}}(t) \\ \dot{\hat{\overline{x}}}(t) \end{bmatrix} = \begin{bmatrix} \overline{A} & -\overline{B}_1 K_g \\ L_g \overline{C} & \overline{A} - \overline{B}_1 K_g - L_g \overline{C} \end{bmatrix} \begin{bmatrix} \overline{x}(t) \\ \hat{\overline{x}}(t) \end{bmatrix} \tag{5.25}$$

The parameters used for the simulation are listed in Table 5.3. The optimal feedback gain matrixes L_g and K_g are calculated by using the Matlab's LQR command. The weighting matrix Q was first assigned as an identity matrix, and then the values were adjusted with respect to the desired performance of the plant and the observer. For example, if the optimal gain K_g is designed to emphasize the vibration control of the plant at its first mode, the weighting matrix Q is expressed as

$$Q = \begin{bmatrix} Q_K & & & & & & \\ & 1 & & & & & \\ & & 1 & & & & \\ & & & Q_K & & & \\ & & & & 1 & & \\ & & & & & 1 & \\ & & & & & & 1 \end{bmatrix}, \tag{5.25}$$

where $Q_K > 1$. Similarly, Q can be designed to emphasize the vibration control at the second mode or the third mode. Similarly, the controller can be designed for the observer subsystem; and Q_L is the constant value used to enhance the performance of the controller designed for the observer. To limit the control effort, $R = 10$ was used to design the feedback gains for both subsystems. Values used for Q_K and Q_L were 1000 and 10, respectively.

Figures 5.16 to 5.22 show the simulation results of the observer-based feedback control with different feedback gain matrixes L_g and K_g. Three plots were presented in each figure. In Plot (a) the dotted lines indicate the uncontrolled velocity simulation and the solid lines indicate the controlled velocity simulation; Plot (b) presents the error between the plant and the observer outputs; Plot (c) presents the control effort applied to the plant system.

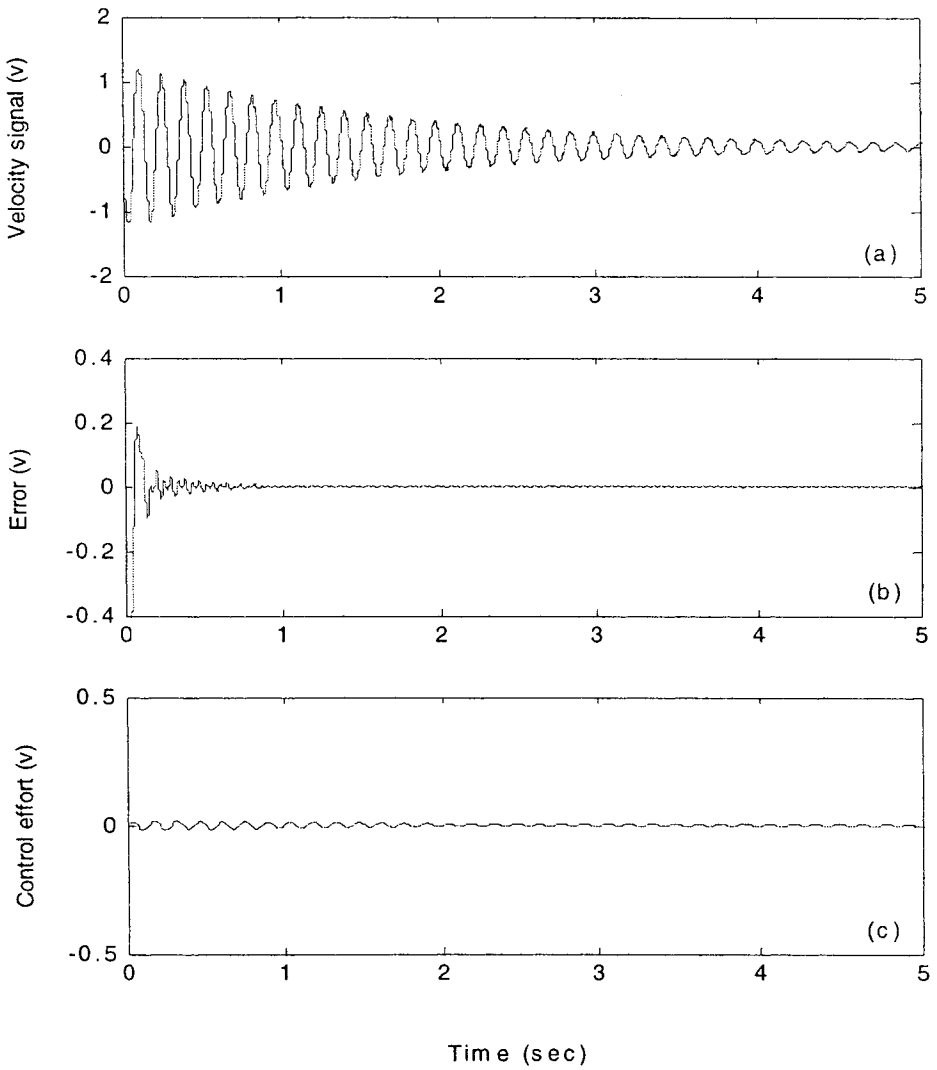

Figure 5.16: Observer-based feedback control simulation results with $Q = I$ and $R = 10$ for both subsystems. (a) Velocity output, (b) Error, (c) Control effort. *

Figure 5.16 shows the simulation results with the weight matrix $Q = I$ for both subsystems. From Figure 5.16, there is almost no difference between the controlled and uncontrolled output. However, the observer is able to estimate the output of the plant with no error within 1 sec. Therefore, the values of Q used for designing the feedback gain K_g have to be increased to enhance the performance of the controller.

* In Figure 5.16 (c), the range of the Y-axis is from 0.5 to –0.5.

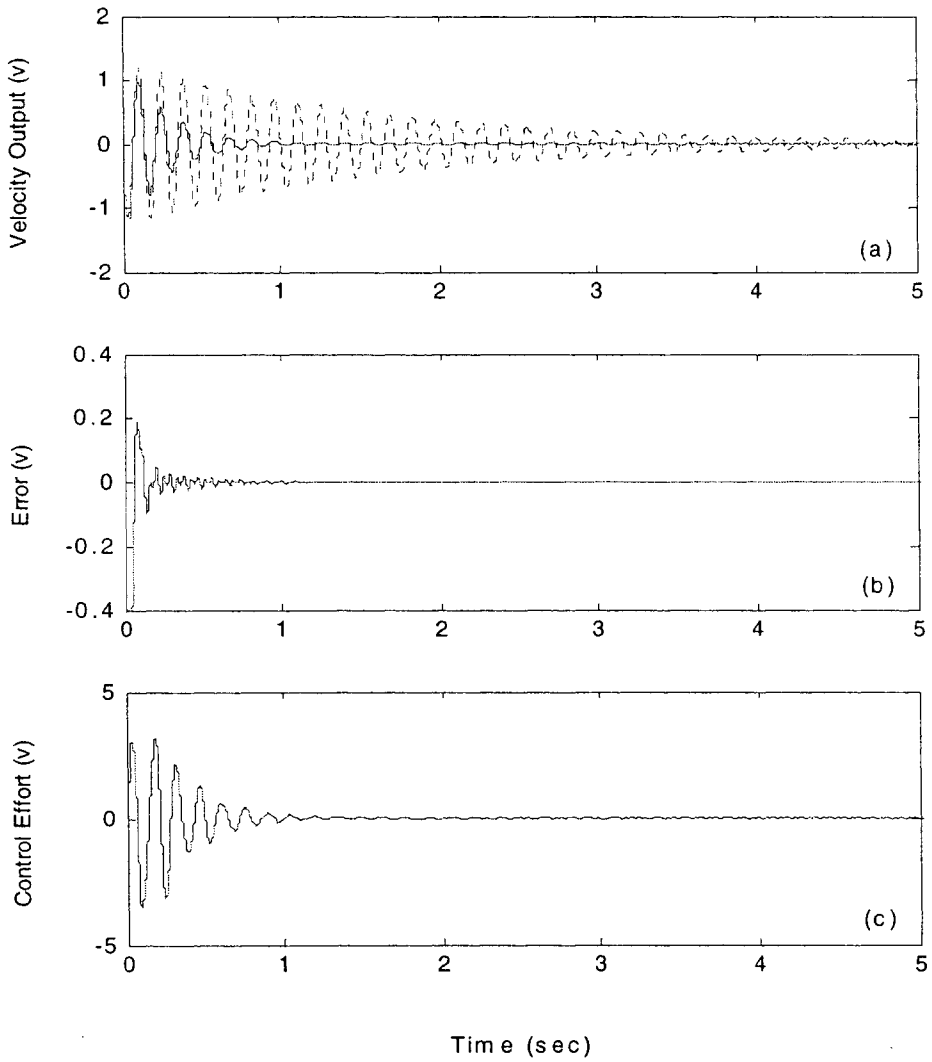

Figure 5.17: Observer-based feedback control simulation results when the control effort of the plant controller is focused on all three modes. (a) Velocity output, (b) Error, (c) Control effort.

Figure 5.17 shows the simulation results when the control effort of the plant controller is focused on all three modes and $Q = I$ for the observer. From Figure 5.17, the vibration is significantly suppressed with the controller. The performance of the observer is the same as that shown in Figure 5.16. The maximum magnitude of the simulated control effort is less than 4 volt.

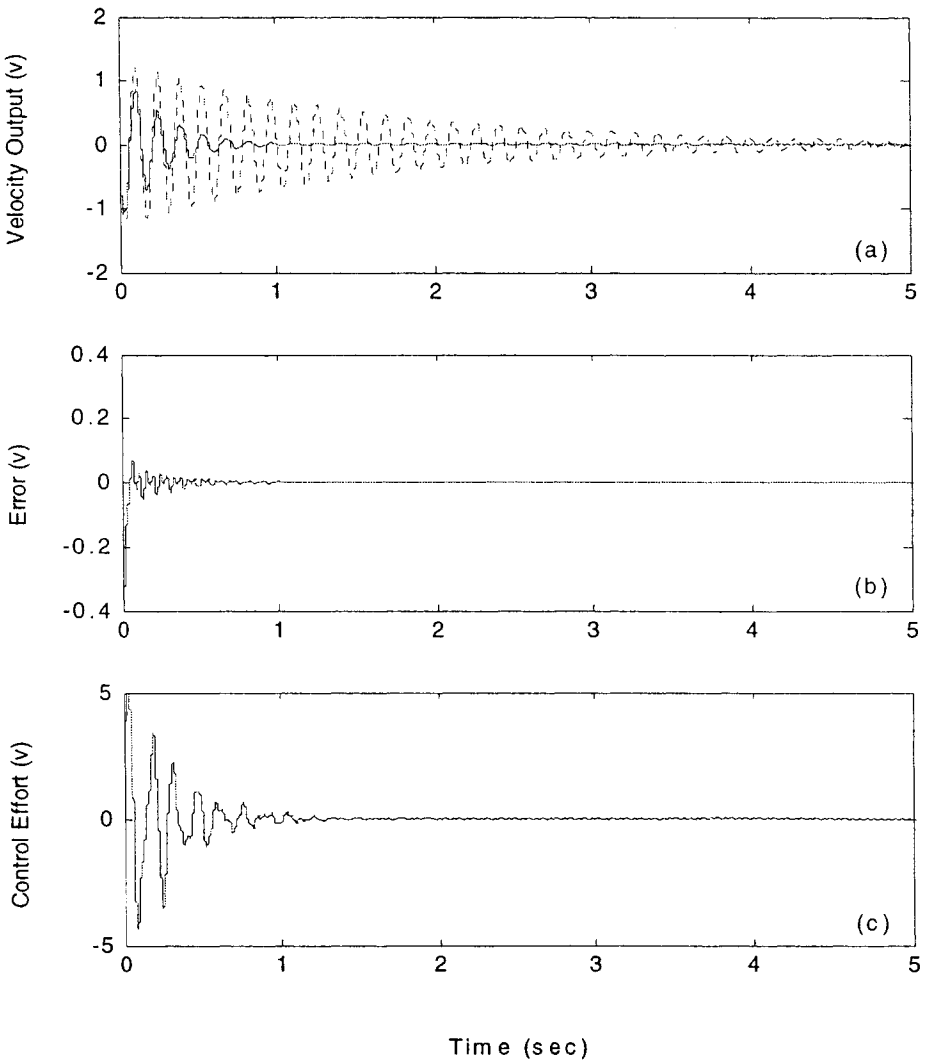

Figure 5.18: Observer-based feedback control simulation results when the control effort of both controllers are focused on all three modes. (a) Velocity output, (b) Error, (c) Control effort.

Figure 5.18 shows the simulation results when the control effort of both controllers are focused on all three modes. From Figure 5.18, the controlled output is almost the same as the controlled output shown in Figure 5.17. However, the overall error between the true states and estimated ones is reduced at a faster rate, and the magnitude of the control effort is increased.

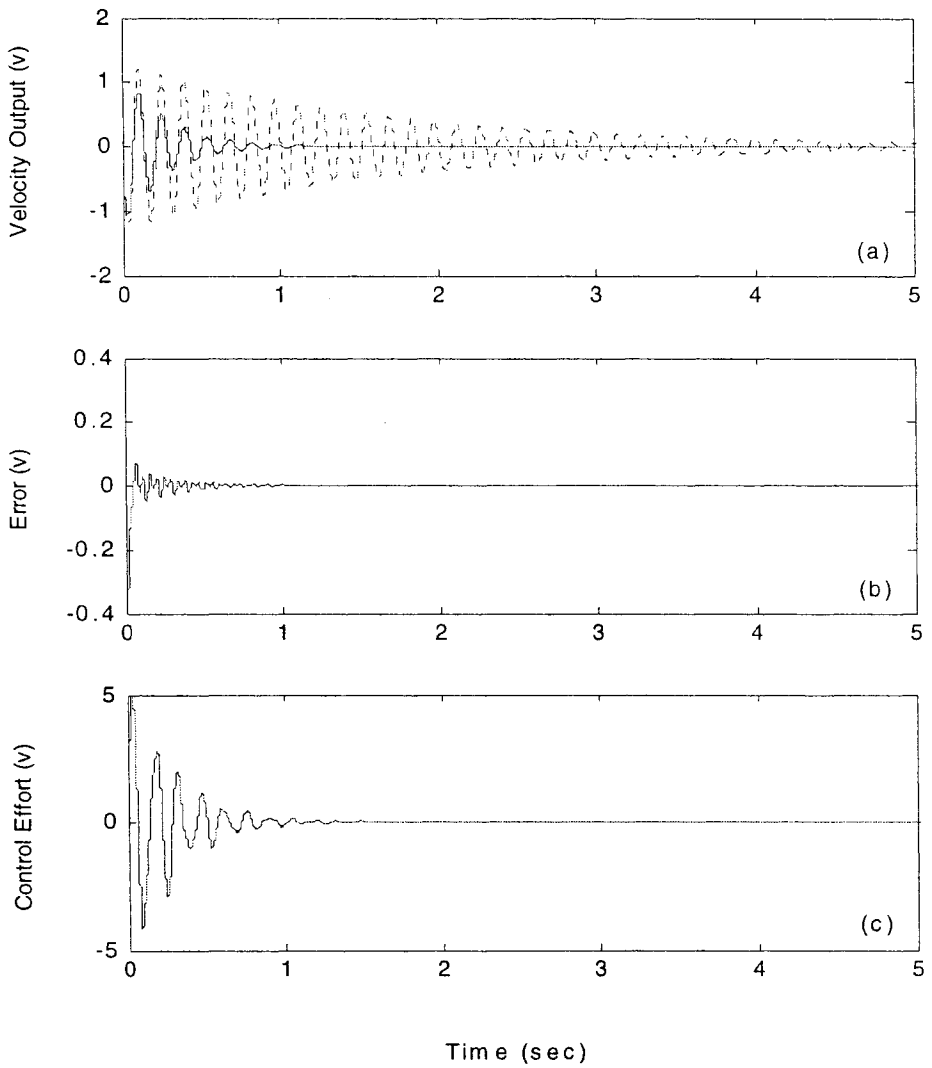

Figure 5.19: Observer-based feedback control simulation results when the control effort of the observer is focused on all three modes and the control effort of the plant is focused on the first mode. (a) Velocity output, (b) Error, (c) Control effort.

Figure 5.19 shows the simulation results when the control effort of the observer is focused on all three modes and the control effort of the plant is focused on the first mode. From Figure 5.19, although the controller designed for the plant is focusing the control effort on the first mode vibration, the simulated plant output is very well controlled. The simulated vibration of the plant completely dissipates in 1 sec.

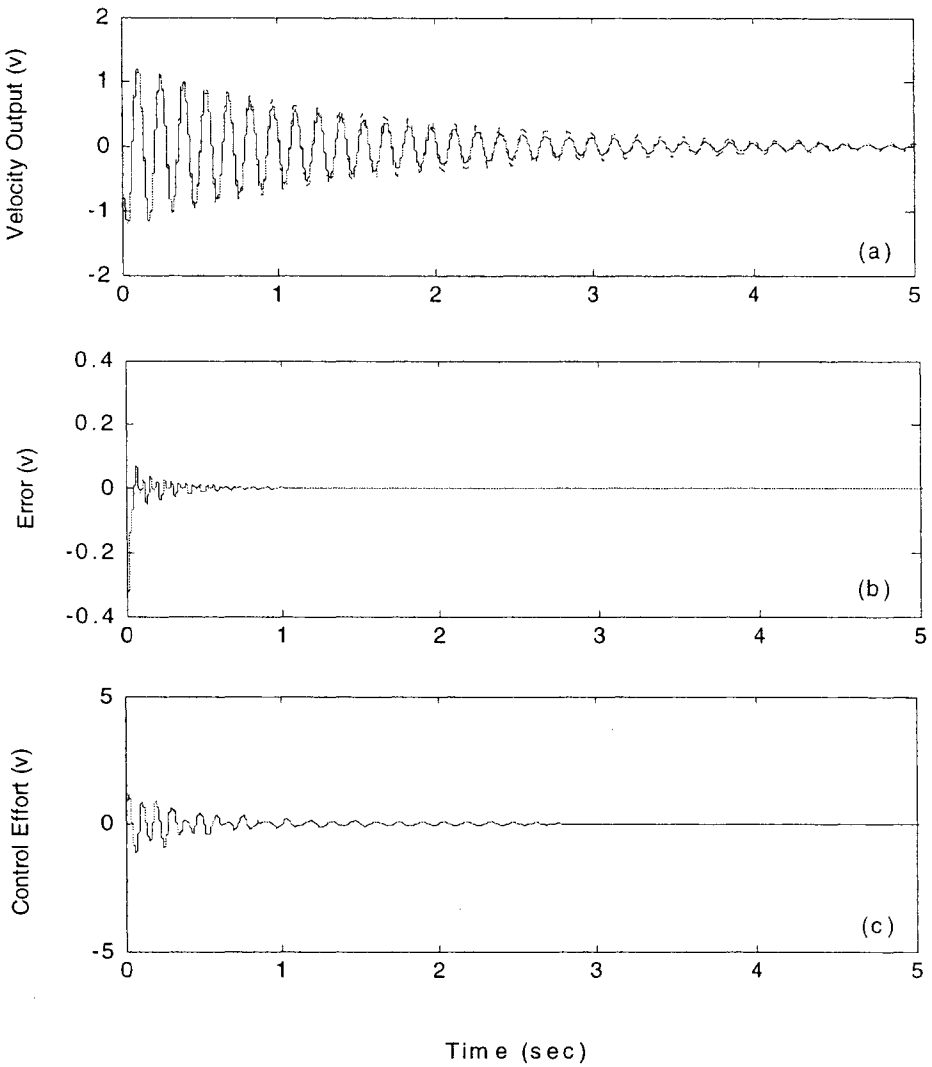

Figure 5.20: Observer-based feedback control simulation results when the control effort of the observer is focused on all three modes and the control effort of the plant is focused on the second mode. (a) Velocity output, (b) Error, (c) Control effort.

Figure 5.20 shows the simulation results when the control effort of the observer is focused on all three modes and the control effort of the plant is focused on the second mode. Form Figure 5.20, the vibration of the plant is poorly controlled, because the magnitude of the second mode is small. This observation explains why the vibration of the plant is well controlled when emphasizing the control effort of the plant at the first mode.

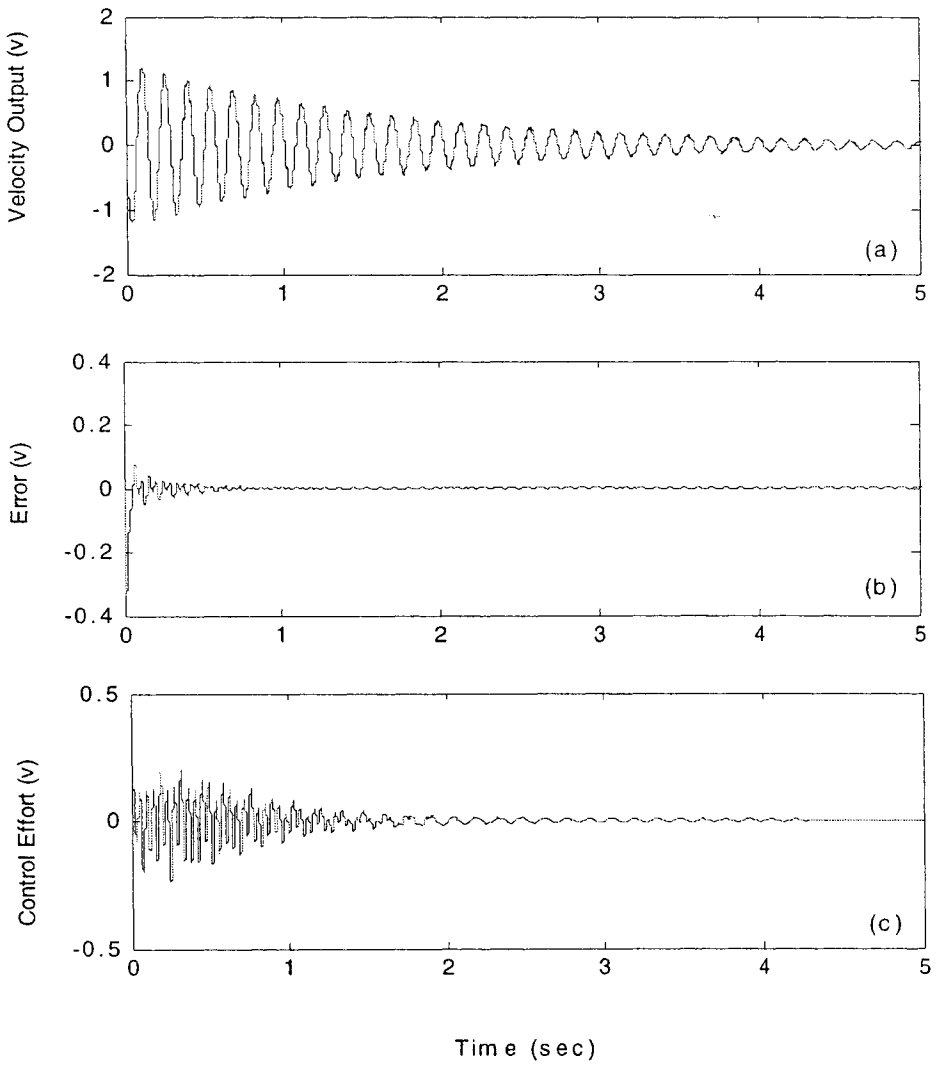

Figure 5.21: Observer-based feedback control simulation results when the control effort of the observer is focused on all three modes and the control effort of the actuator is focused on the third mode. (a) Velocity output, (b) Error, (c) Control effort.*

Figure 5.21 shows the simulation results when the control effort of the observer is focused on all three modes and the control effort of the plant is focused on the third mode. From Figure 5.21, there is almost no difference between the controlled and uncontrolled output, which proves the vibration magnitude of the third mode is very small.

* In Figure 5.21 (c), the range of the Y-axis is from 0.5 to -0.5.

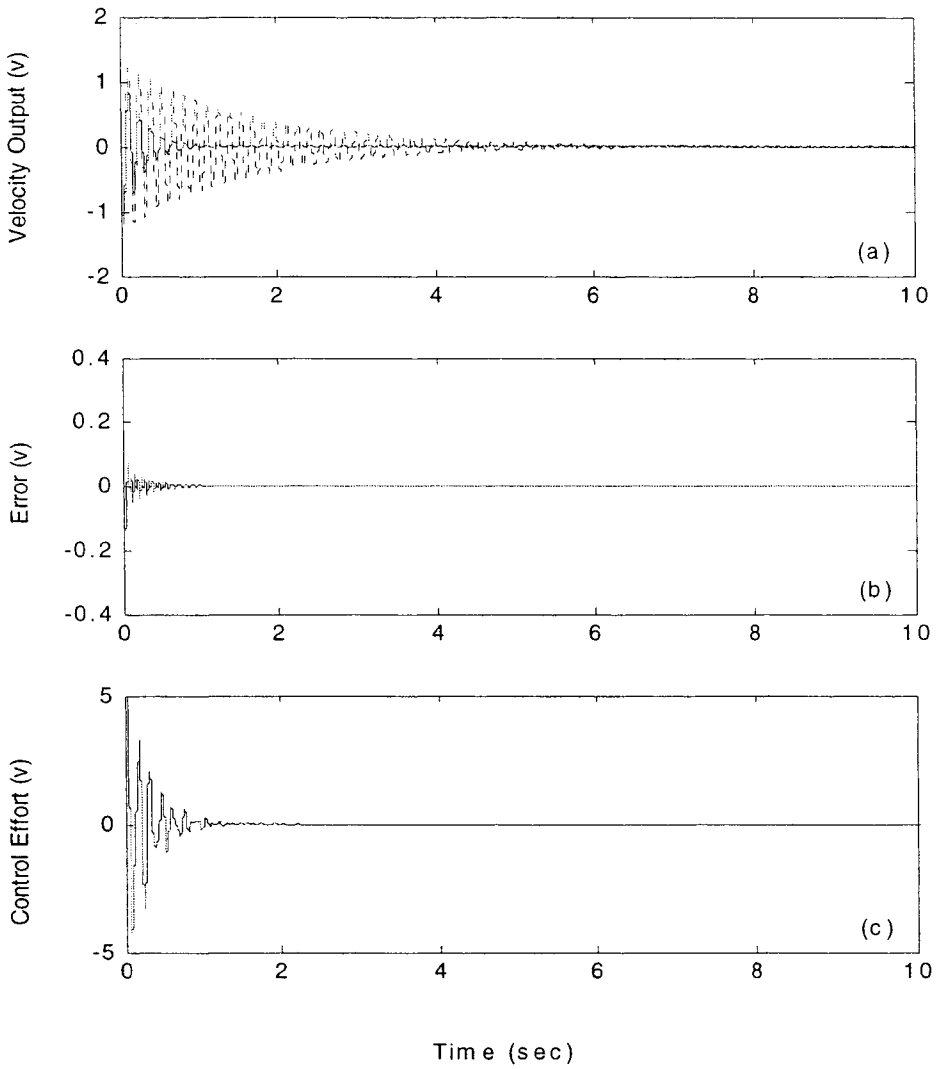

Figure 5.22: Observer-based feedback control simulation results when the control effort of the observer is focused on all three modes and the control effort of the actuator is focused on the first and the second modes. (a) Velocity output, (b) Error, (c) Control effort.

Figure 5.22 shows the simulation results when the control effort of the observer is focused on all three modes and the control effort of the plant is focused on the first and the second mode. From Figure 5.22, the vibration of the plant is well controlled, which indicates the importance of controlling the first and the second mode vibration.

From figure 5.17 to 5.22, the following observations are inferred:

- With the matrix $Q = I$ and $R = 10$, the observer can perform very well. The error between the observer output and the plant output converges to zero in about one second. If the observer focuses the control effort on all three modes vibration with $Q_L = 10$, the error converges faster. However, the control effort increases and there is no dramatic change in the controlled output.
- With the matrix $Q_K = 1000$ and $R = 10$, the vibration of the stationary cable can be well controlled with less than 6 volts control input to the actuator.
- The uncontrolled cable vibration is dominated by the first mode vibration. The third mode vibration is hardly observable in the output.

5.2.5 Experimental results

A LabView program was developed to implement the observer-based feedback control. The velocity signal from the charger amplifier was used as feedback signal. Figure 5.23 shows the block diagram of the developed VI. In the program, a mean removing block was used to remove the signal's offset. A low-pass filter block with cut-off frequency at 30 Hz was used to filter the measured signal. A Runge Kutta (RK) integrator block was used to estimate the states. A formulated block was used to estimate the output $\hat{y}$ and calculate the control input v_a. The control input v_a was sent to the digital to analog channel to control the actuator system. The estimate output $\hat{y}$ was compared with the measured output, and the difference was fed back to the RK integrator block with the control input v_a to estimate the states.

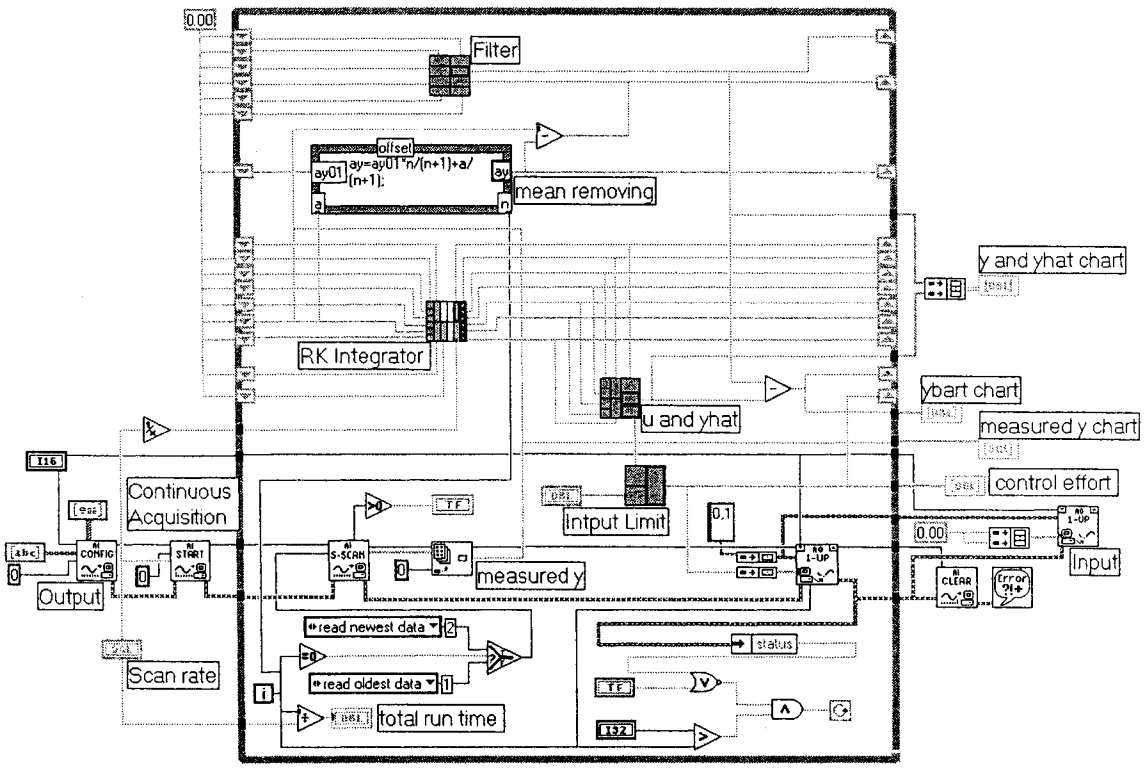

Figure 5.23: The block diagram of the Observer-based feedback control VI

An initial displacement was applied to the cable at about 0.489 m above the actuator. The scan rate of the program was 500 scans/sec. Different values of K_g and L_g were designed as described in Section 5.1.4. Figures 5.24 to 5.30 show the experimental results. Three plots were presented, in each figure. Plot (a): the dotted lines indicate the observer's estimated output signal and the solid lines indicate the measured lateral velocity signal; Plot (b): presents the error between the measured and the estimated outputs; Plot (c): presents the control effort applied to the actuator.

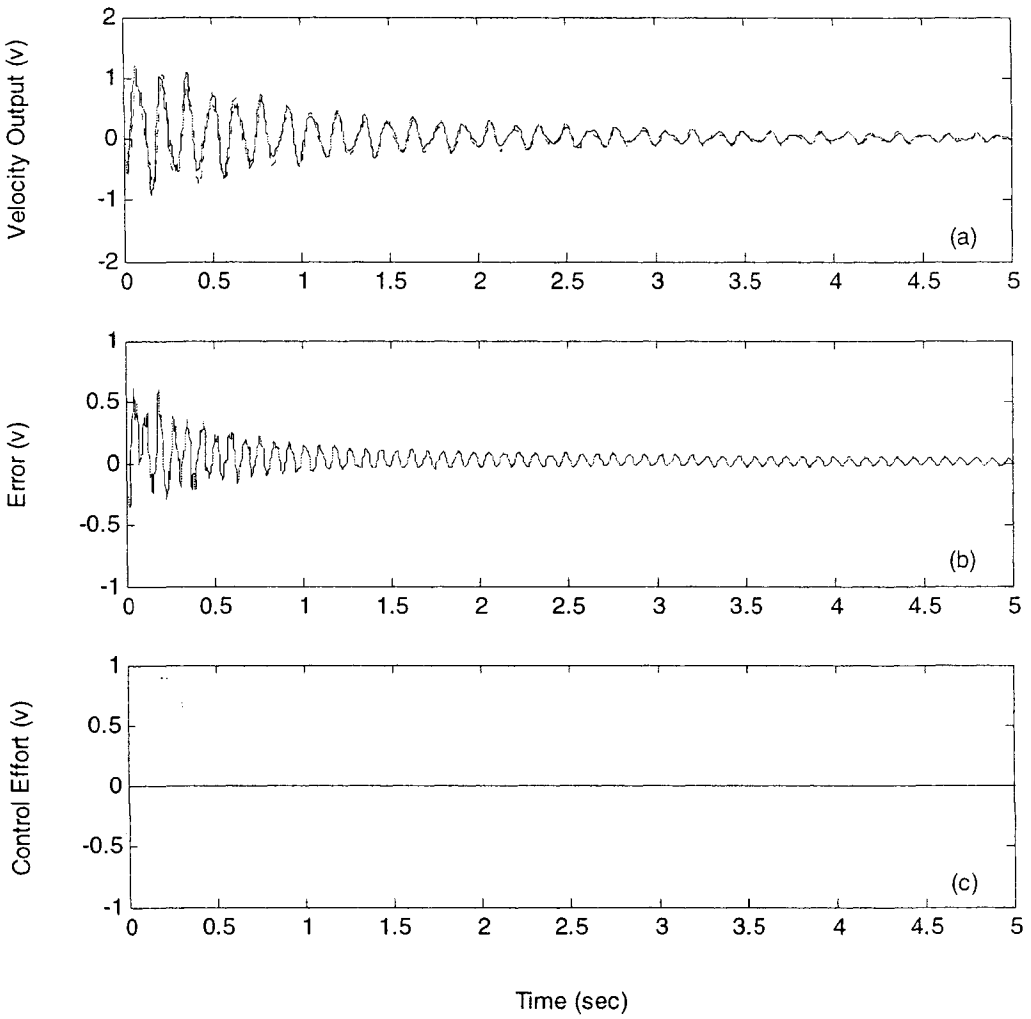

Figure 5.24: Observer-based feedback control experimental results with no control. (a) Velocity output, (b) Error, (c) Control effort.

Figure 5.24 shows the uncontrolled experimental results. From Figure 5.24, the estimated output is able to follow the measured velocity signal at the first mode but not quite well at the second and the third mode. The free vibration of the stationary cable system is completely dissipated in 10 seconds.

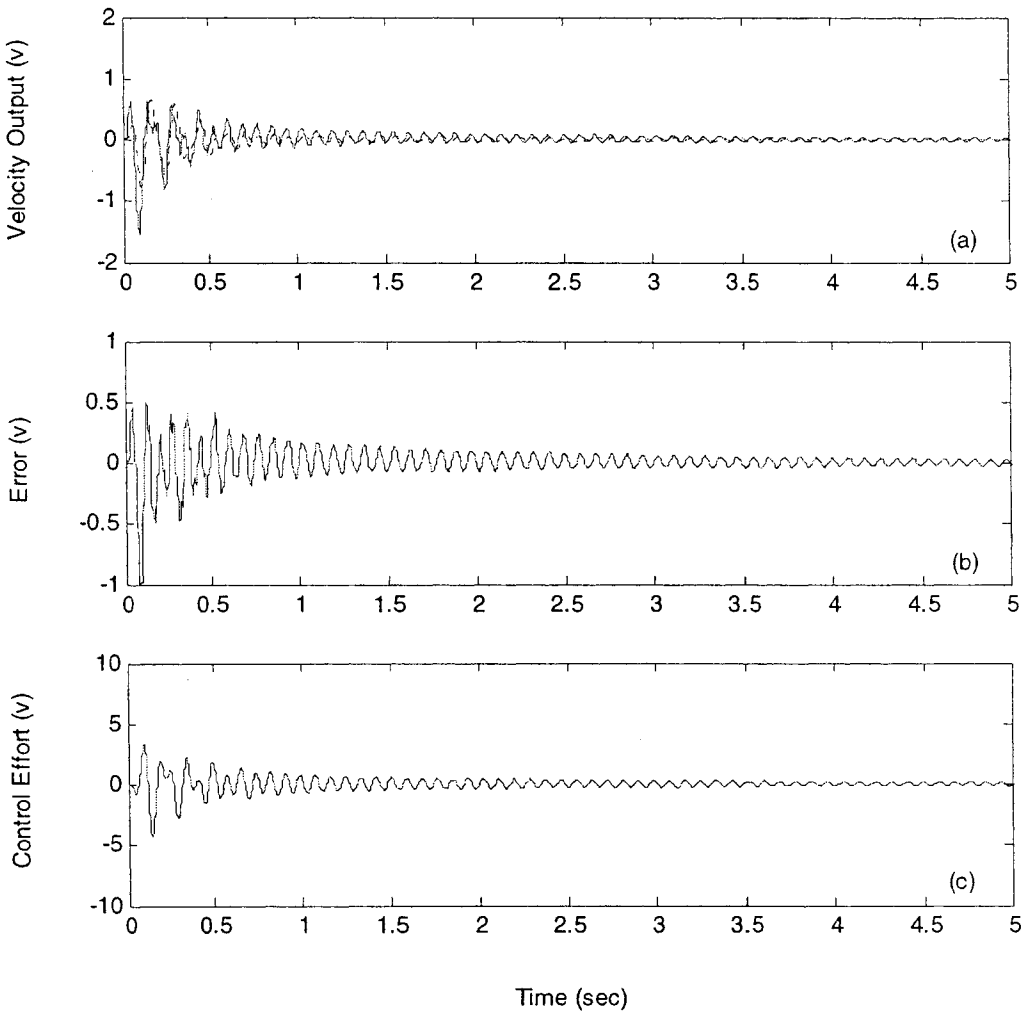

Figure 5.25: Observer-based feedback control experimental results when the control effort of the actuator is focused on all three modes. (a) Velocity output, (b) Error, (c) Control effort.

Figure 5.25 shows the experimental results when the control effort of the actuator is focused on all three modes. From Figure 5.25, the vibration of the stationary cable system is suppressed at the beginning of the vibration. The controlled vibration does not completely dissipate in 10 seconds, which can be explained by the existence of the error signal caused by the second and third mode vibration. The error signal will lead the observer to produce an incorrect control input to excite the cable system through the actuator.

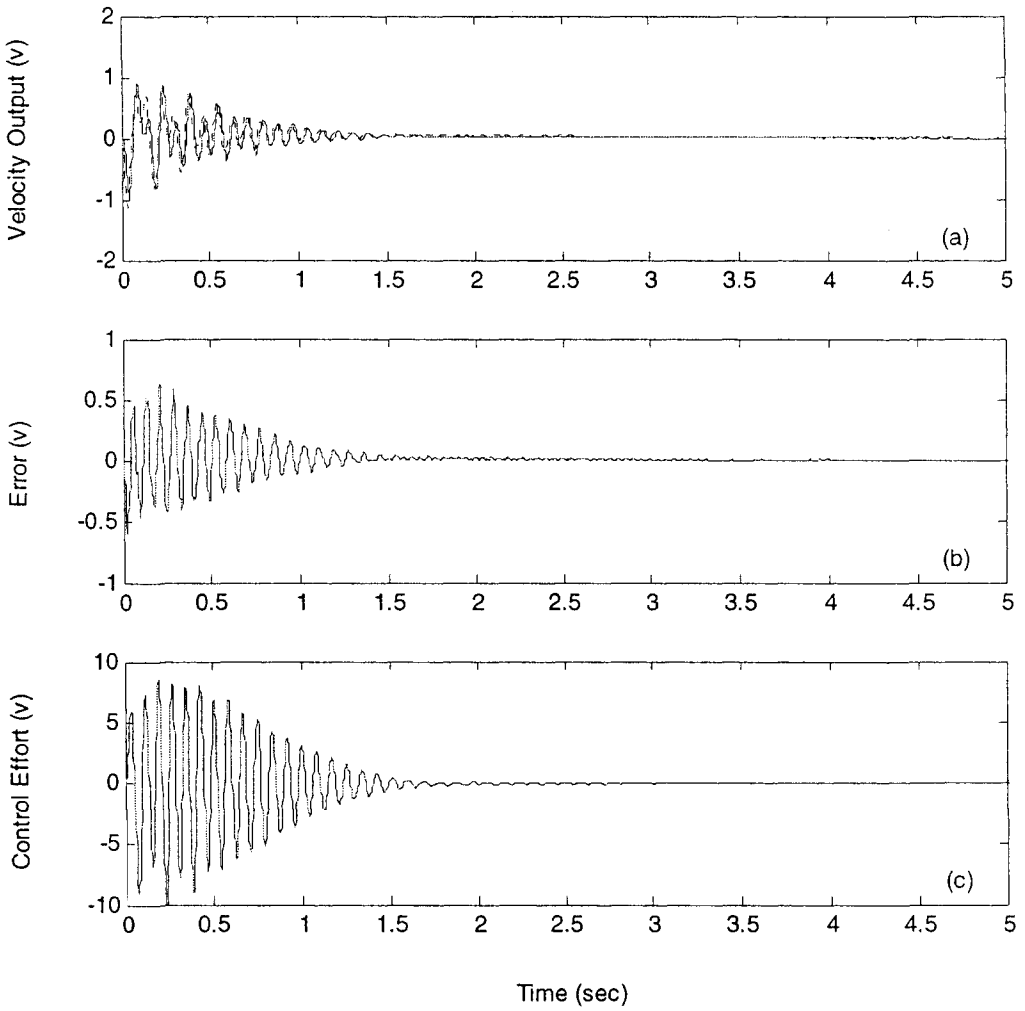

Figure 5.26: Observer-based feedback control experimental results when the control effort of both the observer and the actuator are focused on all three modes. (a) Velocity output, (b) Error, (c) Control effort.

Figure 5.26 shows the experimental when the control effort of both the observer and the actuator are focused on all three modes. From Figure 5.26, the vibration of the stationary cable system is successfully controlled. The controlled vibration is completely dissipated in 4 seconds. This is the best result obtained from the observer output feedback experiment.

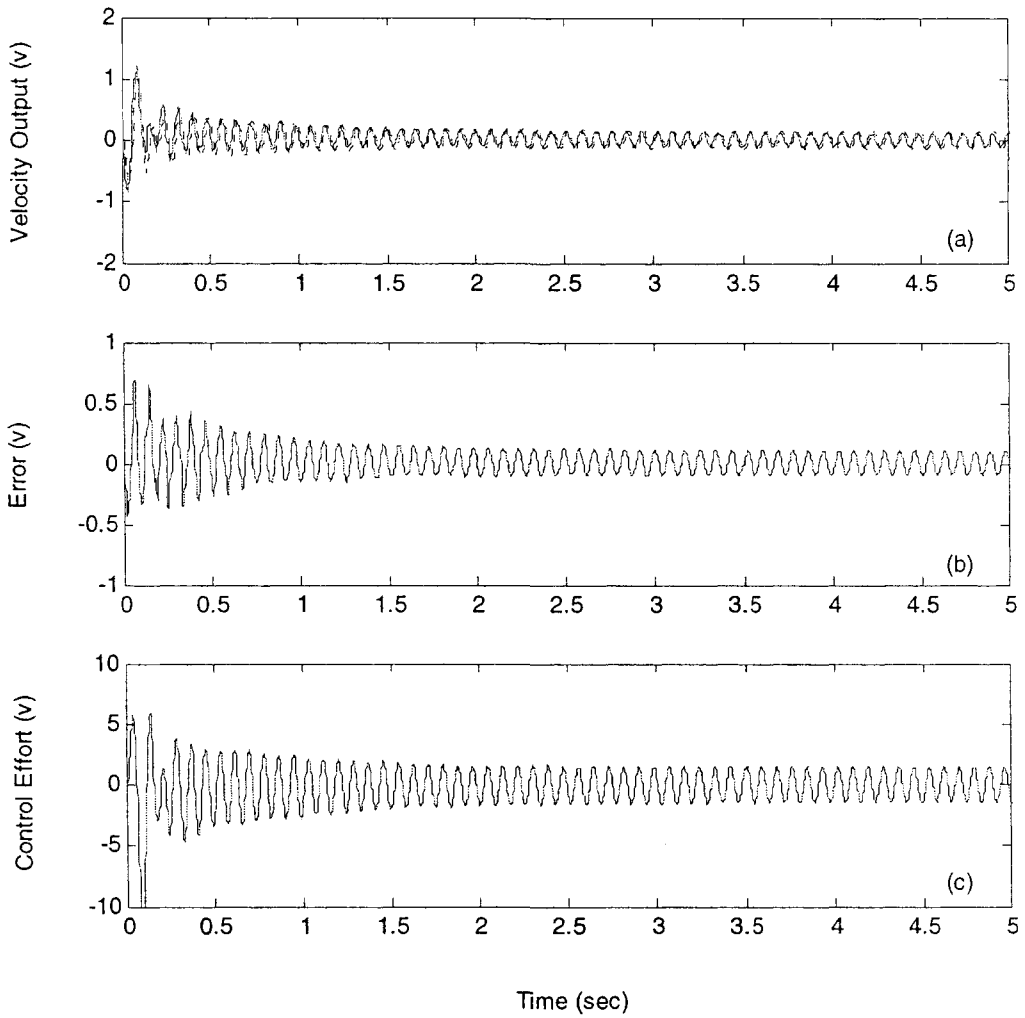

Figure 5.27: Observer-based feedback control experimental results when the control effort of the observer is focused on all three modes and the control effort of the actuator is focused on the first mode. (a) Velocity output, (b) Error, (c) Control effort.

Figure 5.27 shows the experimental results when the control effort of the observer is focused on all three modes and the control effort of the actuator is focused on the first mode. From Figure 5.27, the first mode vibration of the stationary cable system is successfully controlled. Because the controller was designed to focus the control effort on the first mode, the magnitude of the error signal caused by the second and third mode vibration became bigger. This error signal causes the cable system to vibrate at a higher magnitude.

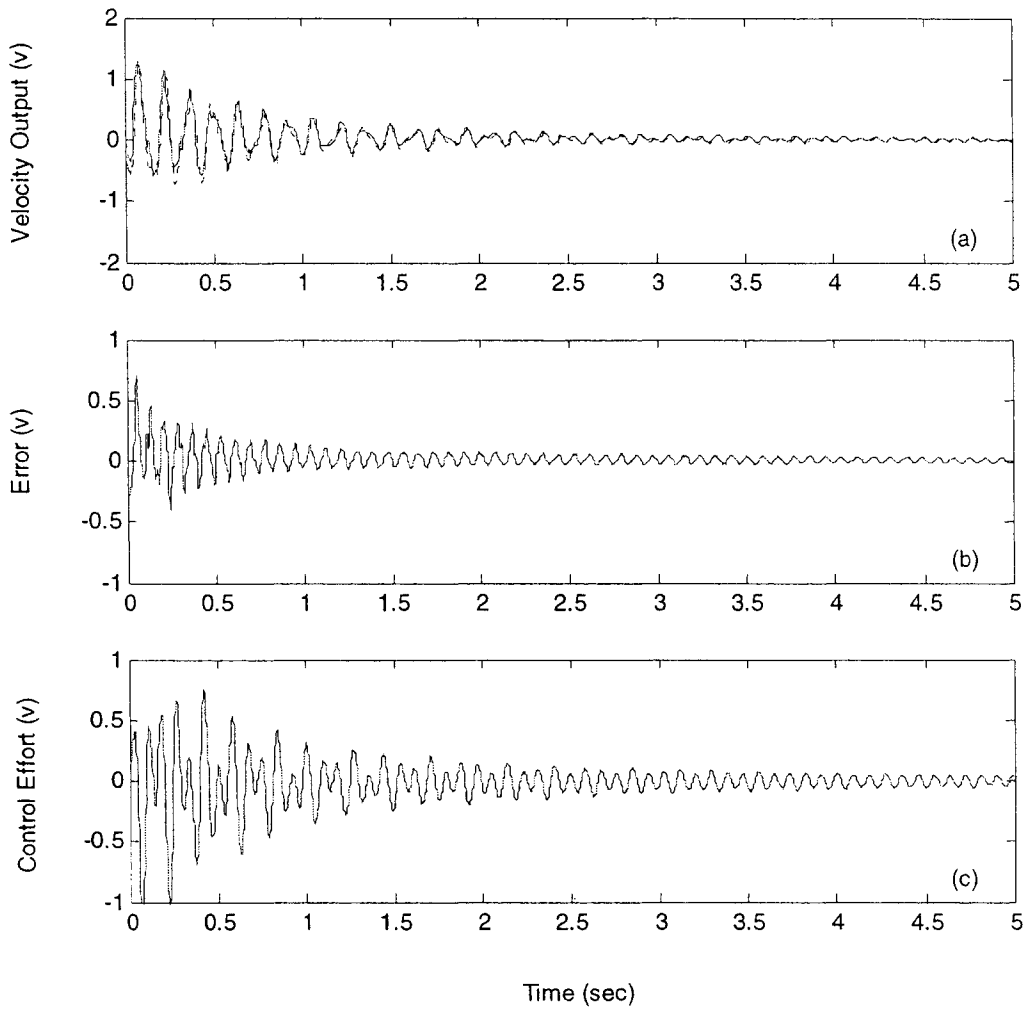

Figure 5.28: Observer-based feedback control experimental results when the control effort of the observer is focused on all three modes and the control effort of the actuator is focused on the second mode. (a) Velocity output, (b) Error, (c) Control effort.*

Figure 5.28 shows the experimental results when the control effort of the observer is focused on all three modes and the control effort of the actuator is focused on the second mode. The importance of controlling the second mode vibration is demonstrated in Figure 5.28. As can be inferred from a comparison with Figure 5.26, the control system reveals much better results. Since the magnitude of the third mode vibration is small, the error signal caused by the third mode has no dramatic effect to the actuator system.

* In Figure 5.28 (c), the range of the y-axis is from 1 to –1.

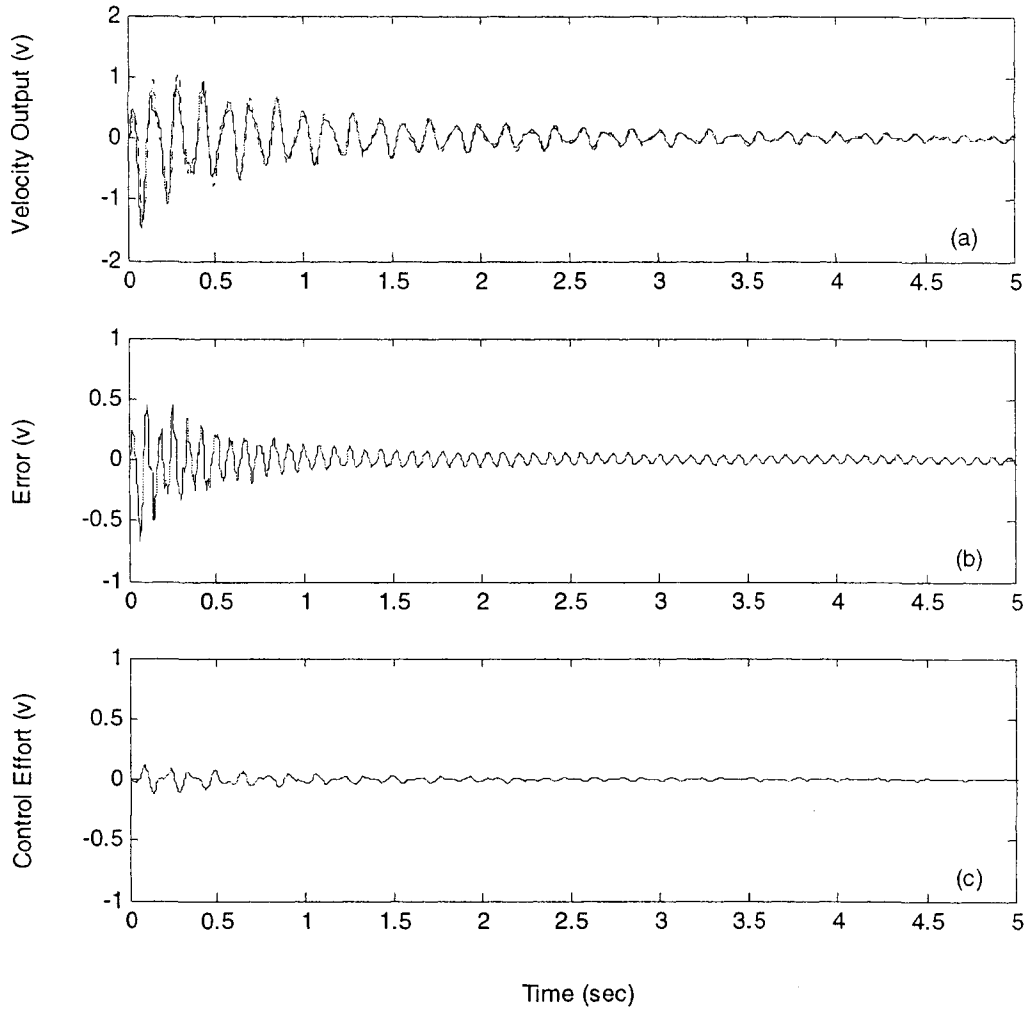

Figure 5.29: Observer-based feedback control experimental results when the control effort of the observer is focused on all three modes and the control effort of the actuator is focused on the third mode. (a) Velocity output, (b) Error, (c) Control effort.*

Figure 5.29 shows the experimental results with emphasizing the control effort of the observer at all three modes and the control effort of the actuator at the third mode. From The importance of controlling the third mode vibration is demonstrated. As can be inferred from a comparison with Figure 5.28, the effort used to control the third mode vibration is less that used to control the second mode vibration. The weakly controlled second mode vibration has more vivid effect on the system.

* In Figure 5.29 (c), the range of the Y-axis is from 1 to –1.

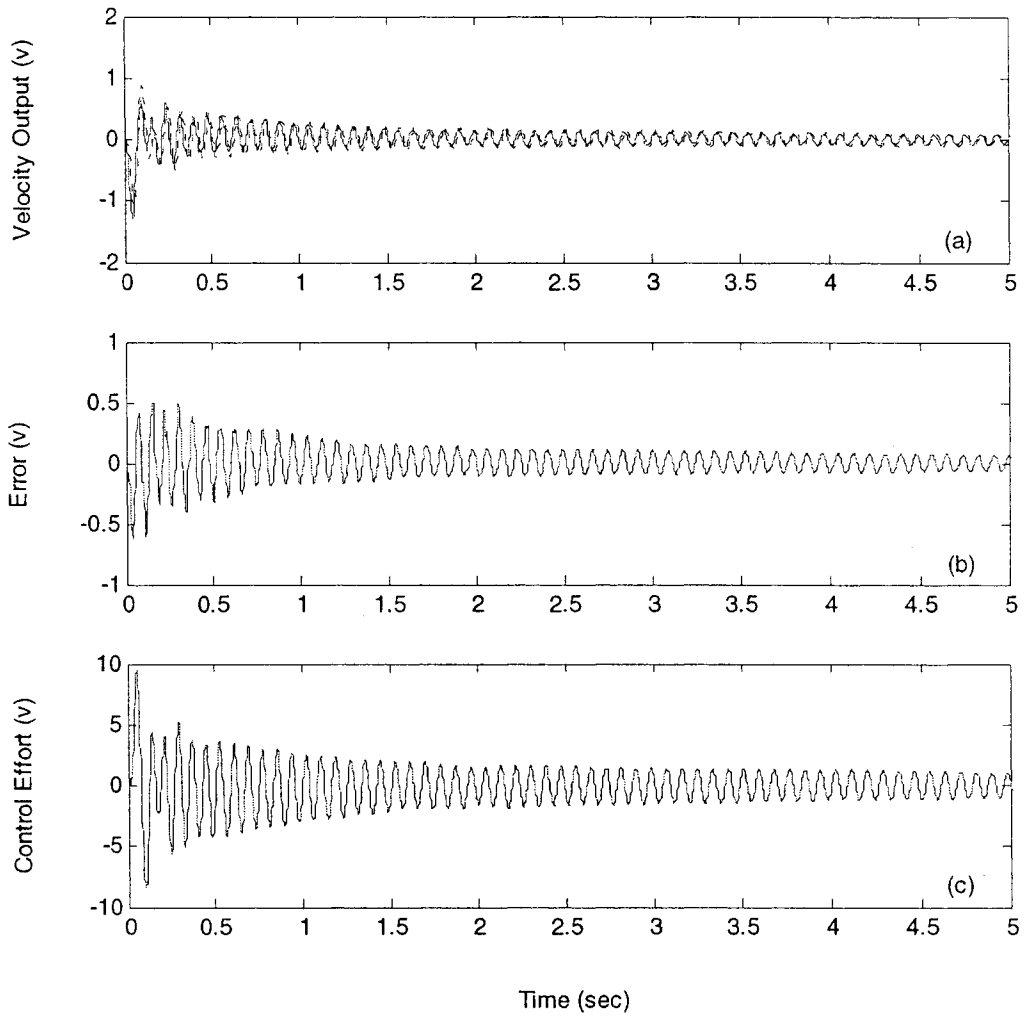

Figure 5.30: Observer-based feedback control experimental results when the control effort of the observer is focused on all three modes and the control effort of the actuator is focused on the first and the second modes. (a) Velocity output, (b) Error, (c) Control effort.

Figure 5.30 shows the experimental results when the control effort of the observer is focused on all three modes and the control effort of the actuator is focused on the first and the second modes. From Figure 5.30, the first mode vibration of the stationary cable is dissipated in 1 sec. The second mode vibration is observed to be decaying. To conclude the experimental results, the observer output feedback control is successfully realized; and the best results are shown in Figure 5.26.

5.3 Summary

Two active control methods were used to implement the boundary control of the stationary cable system. The direct output feedback control method was first presented. Computer simulations were performed to study the difference between the direct displacement feedback and the direct velocity feedback. The performance of the boundary control method was also analysed. The parameters used for the direct output feedback simulation were experimentally identified. The controllability of the direct feedback control model was investigated. The direct velocity feedback control was experimentally implemented and the results were discussed. The observer-based feedback control was also used to control the boundary of the stationary cable system. The state-space representation of the stationary cable model was rearranged to include the dynamics of the actuator. And this new model was tuned to estimate the measured velocity signal from the real system and to generate proper control input to the actuator. Both the controllability and the observability for the new model were investigated. The optimal feedback gains used to stabilize the stationary cable system and the observer system were calculated using the LQR method. Computer simulations were performed to study the effectiveness of the observer output feedback control. The observer was also implemented to estimate the states to perform a full-state feedback control through the actuator. The experimental results demonstrated the observer output feedback control could suppress the stationary cable system.

Chapter 6

PRELIMINARY STUDY ON ACTIVE CONTROL OF THE TRAVELLING CABLE SYSTEM

As shown in Chapter 3, the governing equation for the moving cable system is time-varying. Control of a time-varying is challenging both in control algorithm and implementation. This chapter presents a preliminary study on the control of lateral vibration of a travelling cable.

The rest of the chapter is organized as follows: Section 6.1 discusses the controllability and observability of the travelling cable system, Section 6.2 develops a varying gain observer-based controller, Section 6.3 presents the simulation results, Section 6.4 is a brief summary.

6.1 Controllability and Observerability

Unlike the stationary cable system, the travelling cable model is time varying. The controllability and observability are determined by examining the controllability grammian and the observability grammian of the system [20, 32]. For the controllability ,

the system is said to be uniformly controllable if there exist constants α_1 and α_2 such that

$$\alpha_1 \mathrm{I} \le P_c(t) \le \alpha_2 \mathrm{I}, \qquad \forall t > 0, \tag{6.1}$$

where $P_C(t)$ is the controllability grammian defined by

$$P_c(t) = \int_{t_0}^{t_f} \Phi(t, t_0) B(t) B^T(t) \Phi^T(t, t_0) dt, \tag{6.2}$$

where $\Phi(t, t_0)$ is the state transition matrix, and t_0 to t_f denotes cable travelling period. The transition matrix has the following properties

$$\frac{\partial \Phi(t, t_0)}{\partial t} = A(t)\Phi(t, t_0), \qquad \Phi(t_0, t_0) = \mathrm{I}. \tag{6.3}$$

For observability, the system is said to be uniformly observable if there exist constants β_1 and β_2 such that

$$\beta_1 \mathrm{I} \le P_o(t) \le \beta_2 \mathrm{I}, \qquad \forall t > 0, \tag{6.4}$$

where $P_o(t)$ is the observability grammian defined by

$$P_o(t) = \int_{t_0}^{t_f} \Phi^T(t, t_0) C^T(t) C(t) \Phi(t, t_0) dt. \tag{6.5}$$

The controllability and observability of the travelling cable model under the two motion scenarios are examined. Figures 6.1 to 6.3 show the maximum and minimum singular values of the controllability grammian and the observability grammian for both scenarios.

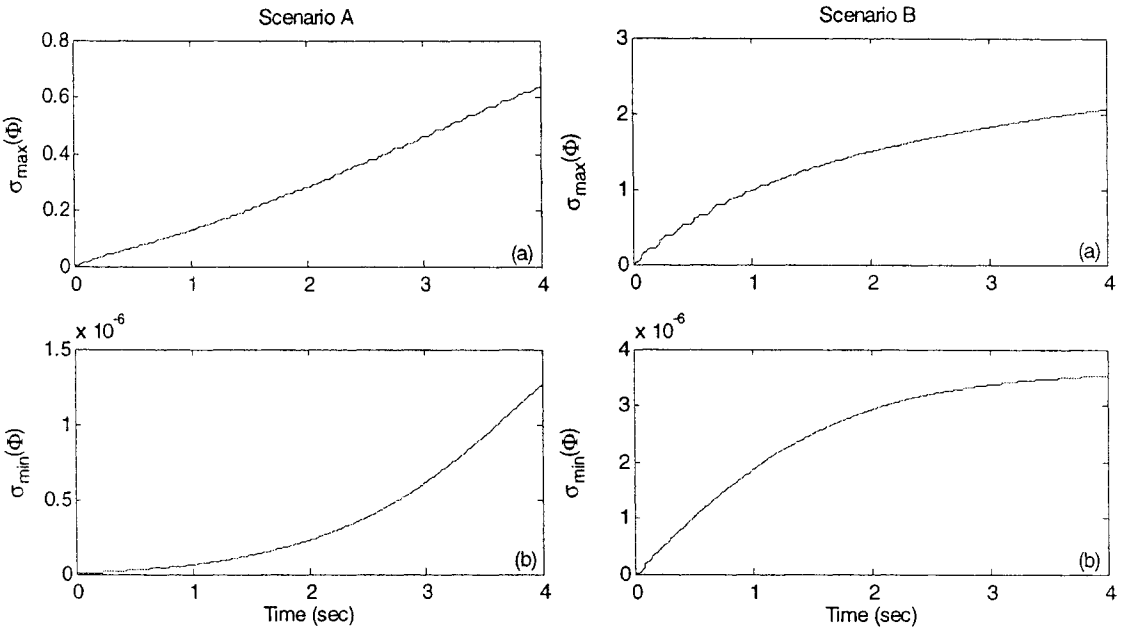

Figure 6.1: Controllability. (a) Maximum singular values of $P_c(t)$, (b) Minimum singular values of $P_c(t)$.

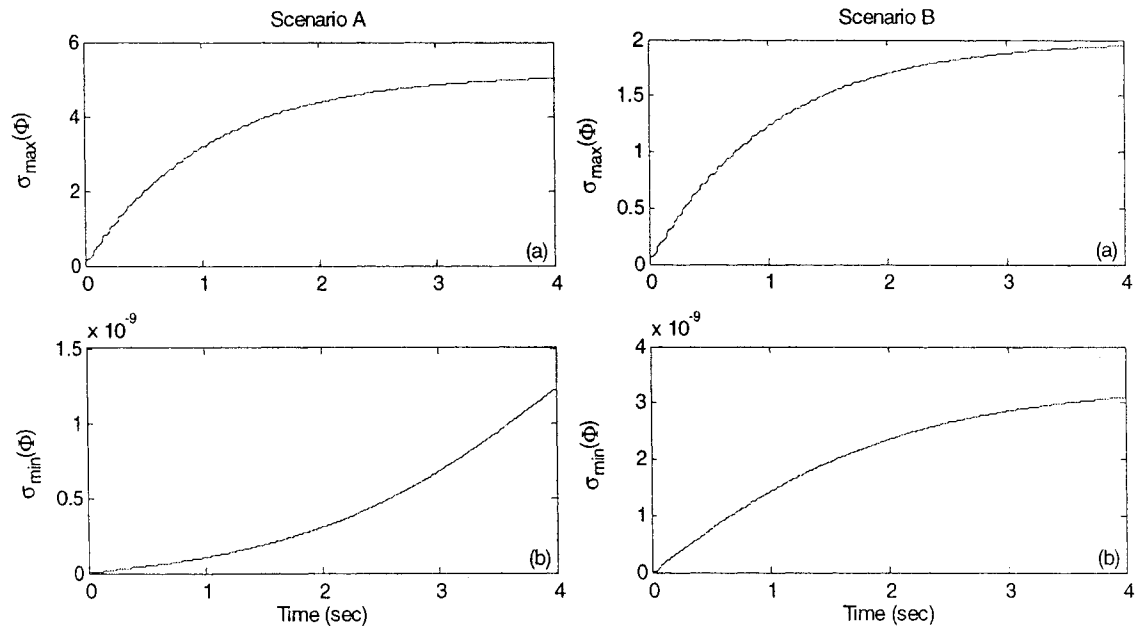

Figure 6.2: Observability with the displacement output. (a) Maximum singular values of $P_c(t)$, (b) Minimum singular values of $P_c(t)$.

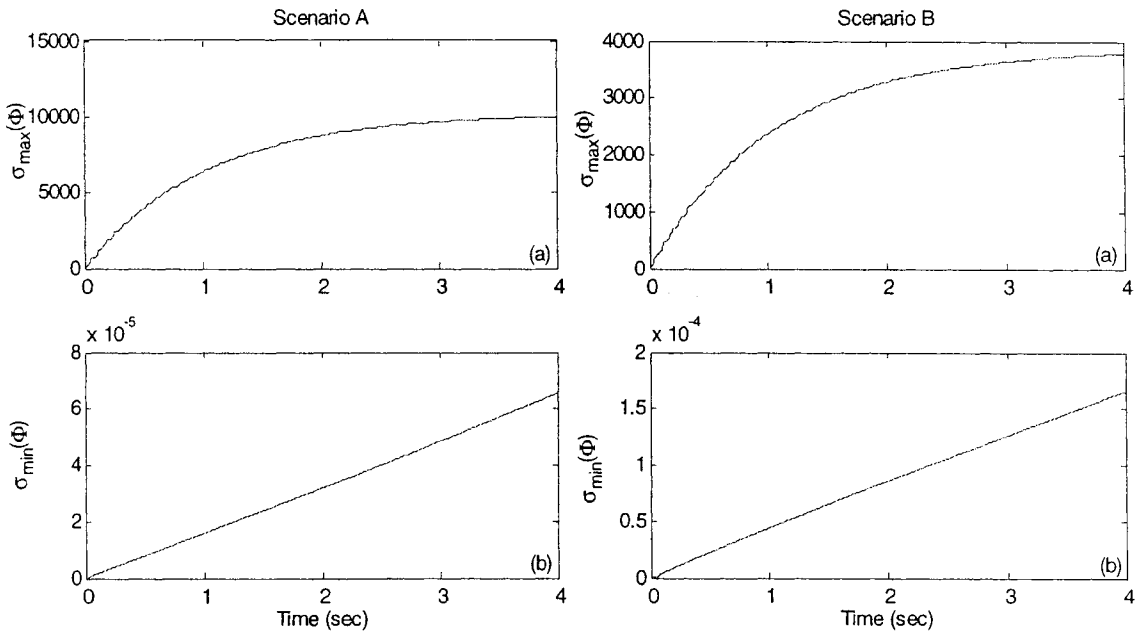

Figure 6.3: Observability with the velocity output. (a) Maximum singular values of $P_c(t)$, (b) Minimum singular values of $P_c(t)$.

From Figures 6.1 to 6.3, the following observations are inferred:

- From Figure 6.1, both the maximum and minimum singular values of $P_c(t)$ for both scenarios are constrained by positive constants. The system is uniformly controllable.
- From Figure 6.2, both the maximum and minimum singular values of $P_c(t)$ for both scenarios are increased. The system is uniformly observable while the system's output is the lateral displacement of the actuator.
- From Figure 6.3, both the maximum and minimum singular values of $P_c(t)$ for both scenarios are constrained by positive constants. The system is uniformly observable while the system's output is the lateral velocity of the actuator.
- The minimum singular values of $P_c(t)$ are very small.

- The minimum singular values of $P_c(t)$ in Figure 6.2 are much lower than those in Figure 6.3, which implies that the observerability with the displacement output is poorer than that with the velocity output.

Based on the above observations, the controllability and the observability were determined again while considering only the first two modes. Figures 6.4 to 6.6 show the results for both scenarios.

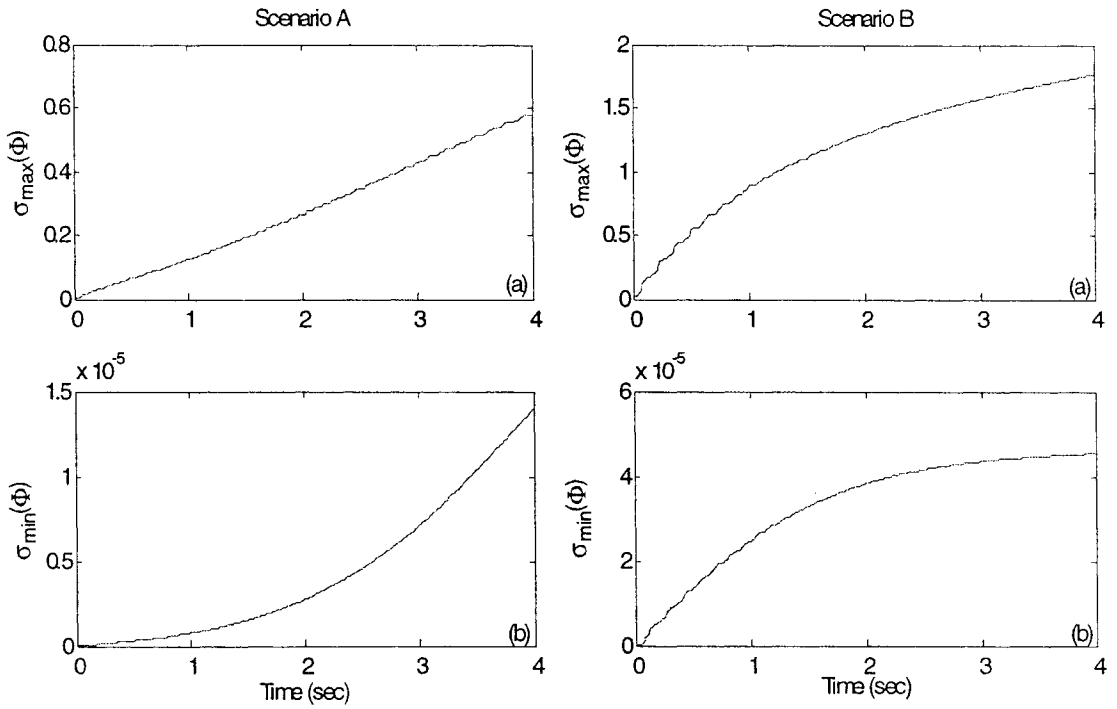

Figure 6.4: Controllability. (a) Maximum singular values of $P_c(t)$, (b) Minimum singular values of $P_c(t)$.

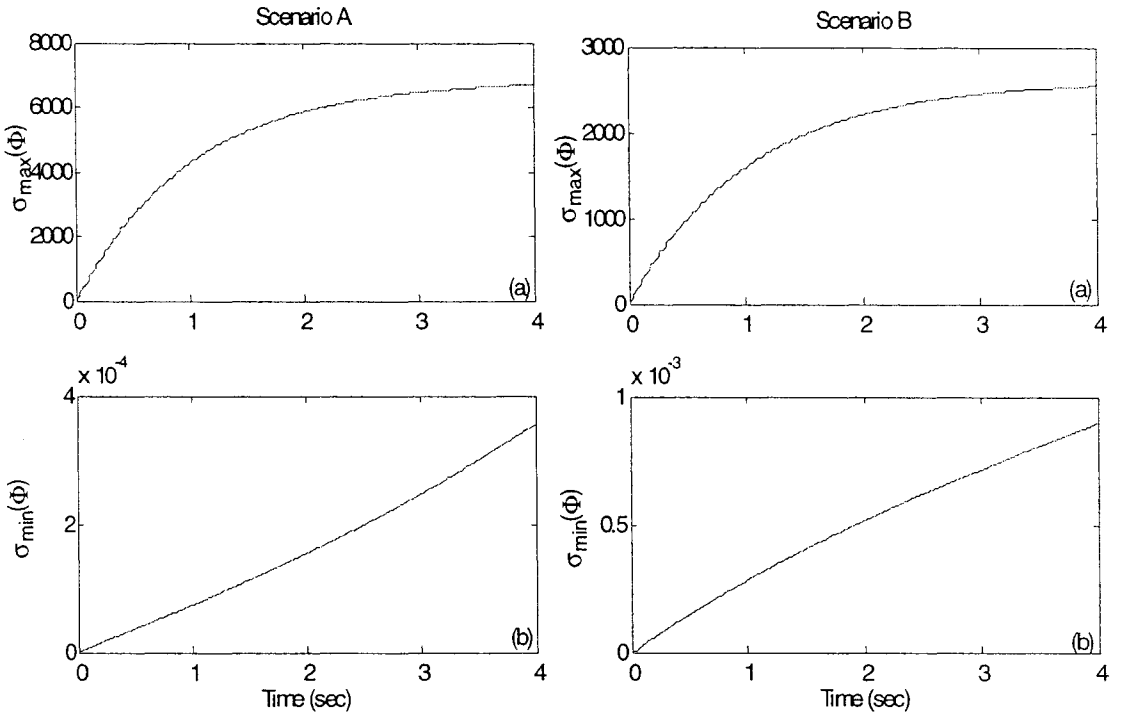

Figure 6.5: Observability with the displacement output. (a) Maximum singular values of $P_c(t)$, (b) Minimum singular values of $P_c(t)$.

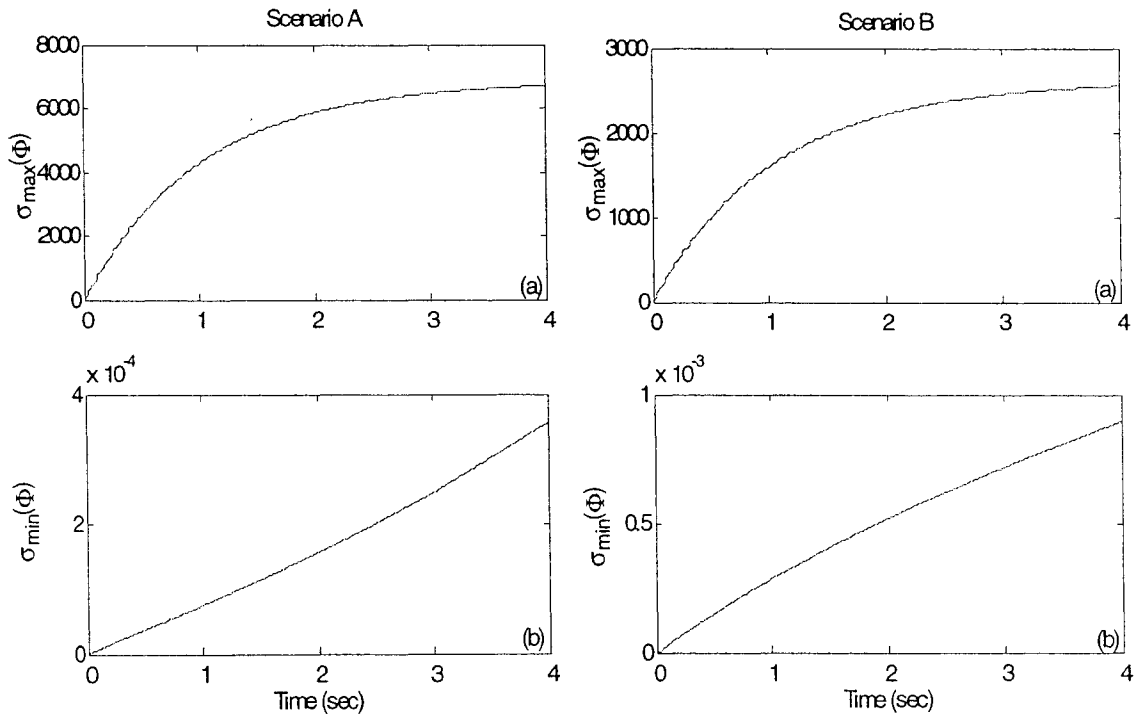

Figure 6.6: Observability with the velocity output. (a) Maximum singular values of $P_c(t)$, (b) Minimum singular values of $P_c(t)$.

From Figures 6.4 to 6.6, the following observations are inferred:

- The maximum singular values of $P_c(t)$ for both scenarios are almost the same as the previous results. The minimum singular values of $P_c(t)$ are increased, which indicates that the model is easier to control if only the first two modes are considered.
- From Figure 6.5, both the maximum and minimum singular values of $P_c(t)$ for both scenarios are increased, which implies that the third mode vibration is very small and not easy to observe.

6.2 Observer-Based Feedback Control Design

To highlight the control effect of the travelling cable, the damping of the cable is not included. Therefore, the travelling cable model described in Section 3.2.1 is used. Without considering the disturbance force, the model of the plant can be rearranged into a state-space representation as

$$\begin{aligned} \dot{x}(t) &= A(t)x(t) + B_1(t)u(t) \\ y(t) &= C(t)x(t) \end{aligned} \quad . \tag{6.6}$$

The control algorithm of the observer-based feedback control has been explained in Section 5.2.1. For the stationary cable model, the system's parameters are fixed, therefore the feedback gains L_g and K_g can be determined by using the LQR algorithm. However, the LQR algorithm is not valid for a time-varying system in general. A close examination of the model of equation (3.58) reveals that the time-varying terms associated with $\dot{l}$ or $\ddot{l}$ are very small compared with the terms associates with l. If $\dot{l}$ and $\ddot{l}$ are set to zero,

equation (3.58) reduces to equation (3.23). As A, B, and C in equation (3.23) are related to the cable length, it is rewritten as

$$\begin{aligned} \dot{x}(t) &= A(l)x(t) + B_1(l)u(t) \\ y(t) &= C(l)x(t) \end{aligned} \quad . \tag{6.7}$$

If the LQR algorithm is applied to equation (6.2) to design an observer-based control by treating $A(l)$, $B(l)$, and $C(l)$ as constants, with the obtained gains L_g and K_g, the controller is valid when the cable stops at the corresponding length l. Following this rationale, the LQR method is used to determine a series of $L_g(l)$s and $K_g(l)$s by varying l from 0.6 to 1.8 m in a step of 0.01 m. Then each element of $L_g(l)$ and $K_g(l)$ is represented by a fourth order polynomial by a least squares error curve fitting of its discrete values corresponding to discrete length values. This fourth order polynomial is then used as a feedback gain function to generate the element of $L_g(l)$ or $K_g(l)$. Now this observer-based controller is applied to the model of the travelling cable. From equation (5.8), the mathematical model for the observer can be rearranged as

$$\begin{aligned} \dot{\hat{x}}(t) &= A(t)\hat{x}(t) + B_1(t)u(t) + L_g(l)(y(t) - \hat{y}(t)) \\ \hat{y}(t) &= C(t)\hat{x}(t) \end{aligned} \quad . \tag{6.8}$$

And the control input $u(t)$ used to control the plant is defined as

$$u(t) = -K_g(l)\hat{x}(t). \tag{6.9}$$

To use such a control strategy, the information of the varying cable length is needed, which is readily provided by the potentiometer attached to the DC motor. Figure 6.7 shows the elements of $L_g(l)$ and $K_g(l)$. Both $L_g(l)$ and $K_g(l)$ were designed to focus the vibration control on all three modes with $R = 10$, $Q_K = 1000$, and $Q_L = 10$. In

Figure 6.7, the solid lines represent the gains pre-determined by the LQR method, and the dotted lines represent the gains generated by the fourth order polynomial.

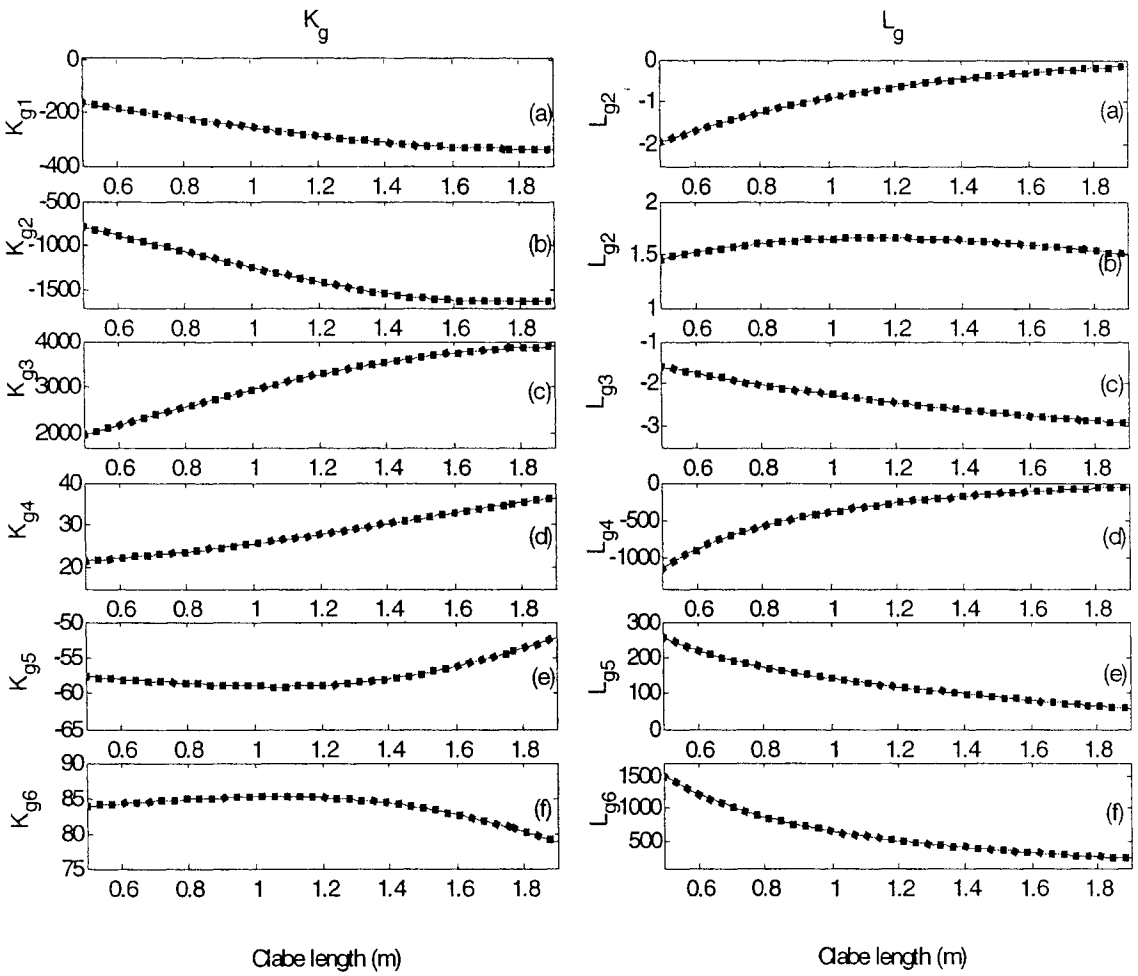

Figure 6.7: $K_g(l)$ and $L_g(l)$ index.

From Figure 6.7, it can be seen that the fourth order polynomials fit the designed gains closely.

6.3 Simulation Results

Computer simulations are conducted to evaluate the performance of the observer-based feedback control proposed in Section 6.2. The motion profiles and the initial conditions of the travelling cable have been described in Section 3.2.1. Similarly, Scenario A and Scenario B were considered. The damping of the actuator was first assumed to be zero.

The output of the system was set to be the lateral velocity at the actuator. The total simulation time is 5 sec while the travelling time is 3.5 sec. Figures 6.8 to 6.10 show the simulation results for both scenarios. In each figure the dotted lines indicate the uncontrolled simulation results and the solid lines indicate the controlled simulation results.

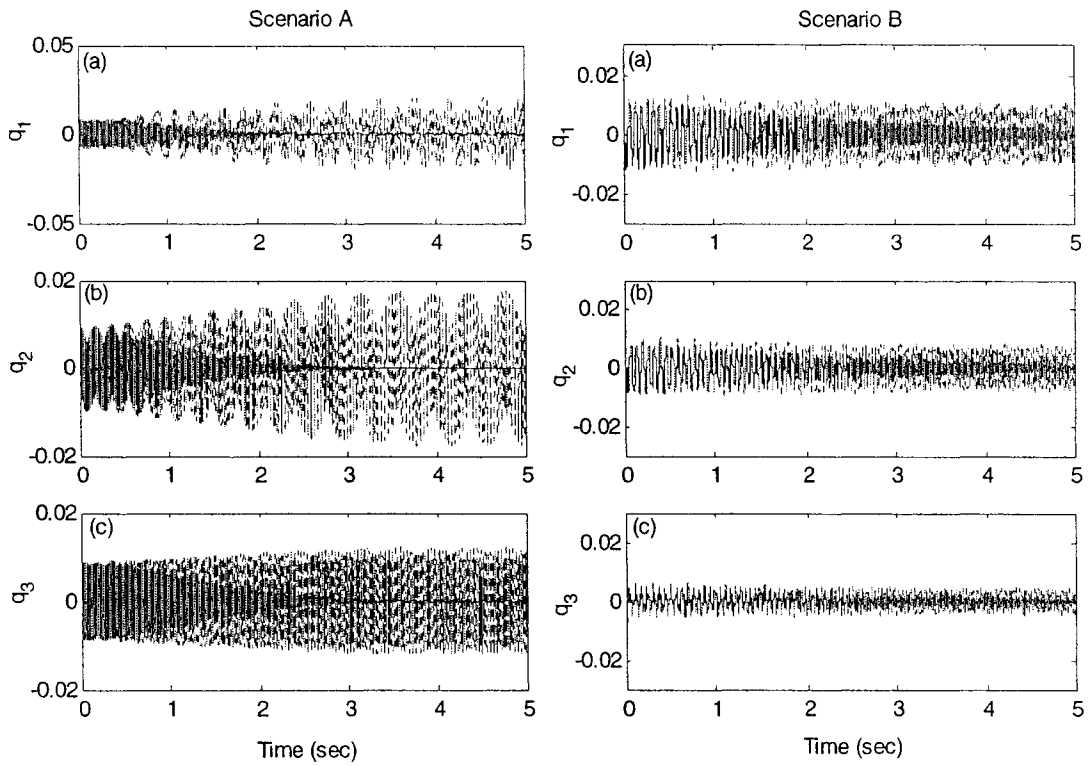

Figure 6.8: The generalized displacements of the travelling cable. (a) First mode, (b) Second mode, (c) Third mode.

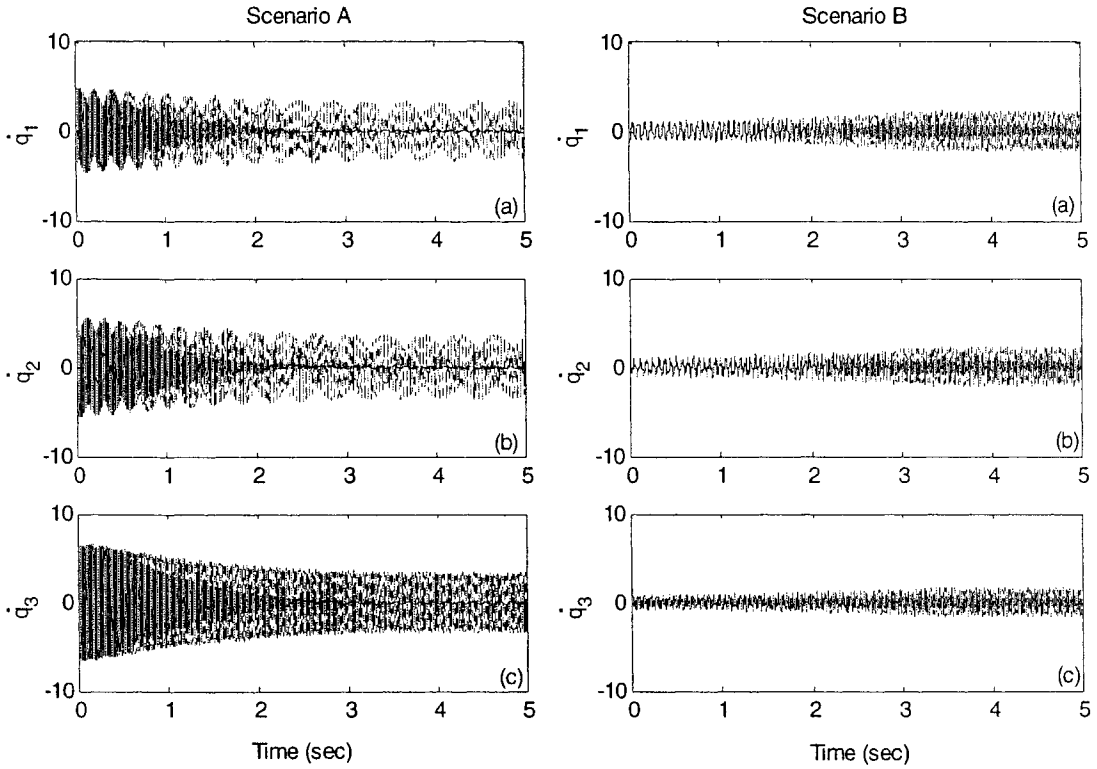

Figure 6.9: The generalized velocities of the travelling cable. (a) First mode, (b) Second mode, (c) Third mode.

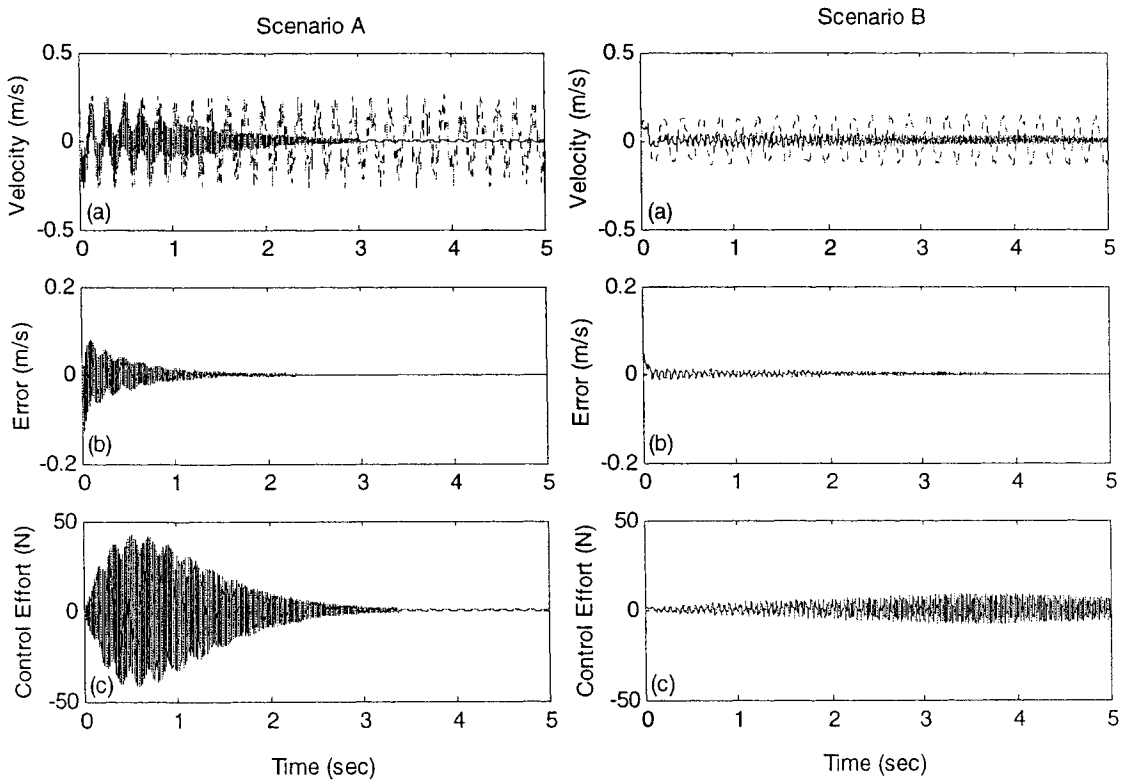

Figure 6.10: Observer-based control system simulation results. (a) Velocity output, (b) Error, (c) Control effort.

From Figures 6.8 to 6.10, the following observations are inferred:

- It is easier for the controller to suppress the vibration in Scenario A. The unstable shortening behaviour increases the difficulty of the vibration control in Scenario B.
- From Figures 6.8 and 6.9, the magnitudes of both the generalized displacements and velocities are greatly reduced in Scenario A. The controller seems to have little effect in Scenario B.
- From Scenario A as shown in Figure 6.10, the control effort increases to almost 50 N at 0.5 sec and gradually reduces to near zero at 3.5 sec. This observation not only indicates that the magnitude of the vibration in Scenario A is greater, but also indicates that the vibration energy is easier to be overcome in Scenario A.
- From Scenario B of Figure 6.10, the control effort gradually increases to 9 N at the end the travelling period and then gradually reduces while the cable remains stationary. This observation illustrates that the magnitude of the vibration in Scenario B is quite small. However, the unstable shortening behaviour increases the difficulty of the vibration control.

From the observations above, it seems that the observer-based control has less effect on the cable is retracting. However, the above simulations were based on the model where the physical damping of the actuator is ignored. Therefore, simulations in which the physical damping is included are also implemented. Figures 6.11 to 6.13 show the simulation results for both scenarios.

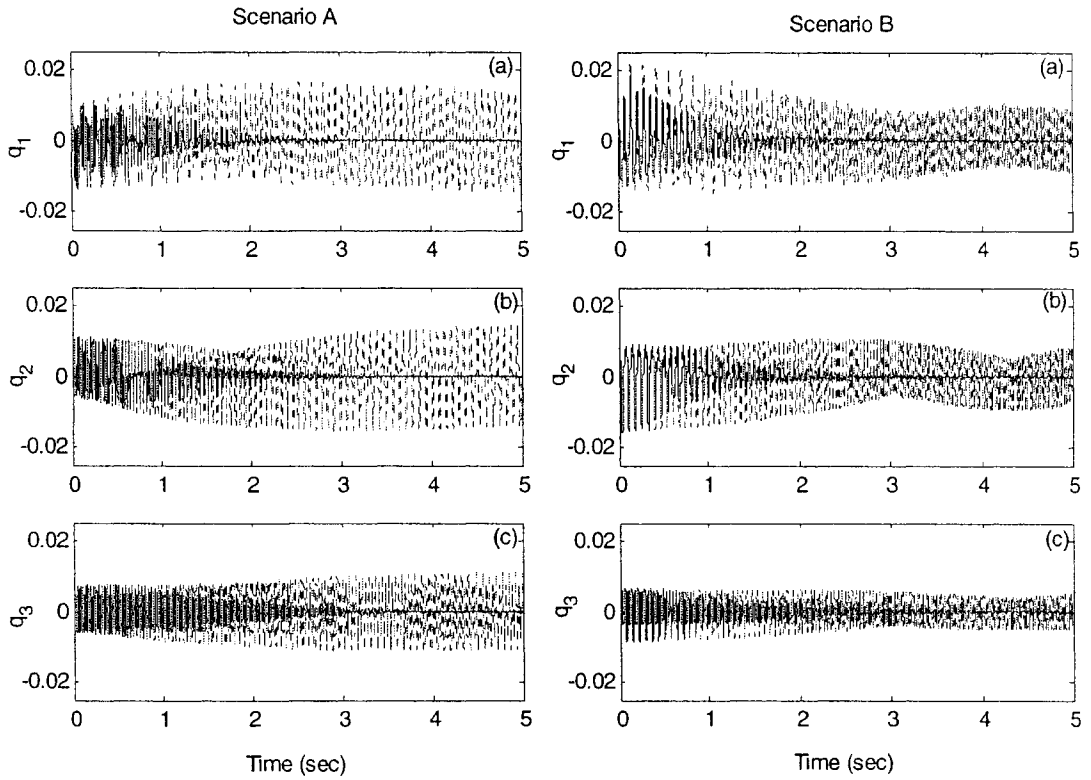

Figure 6.11: The generalized displacements of the travelling cable. (a) First mode, (b) Second mode, (c) Third mode.

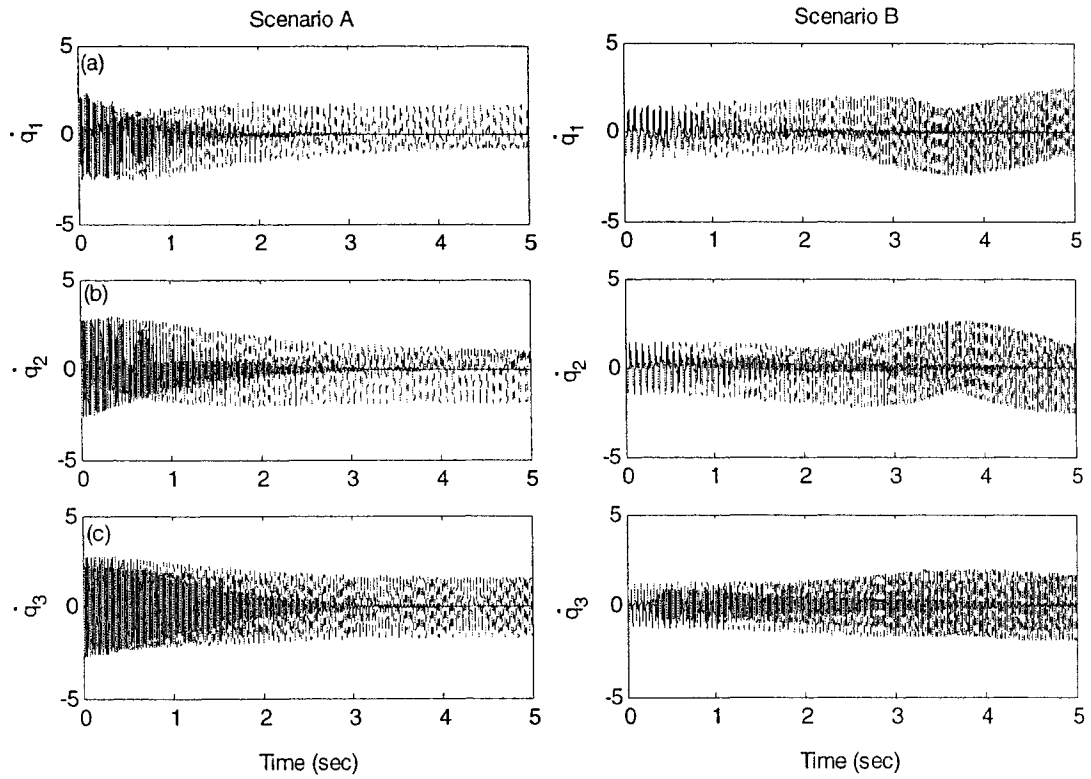

Figure 6.12: The generalized velocities of the travelling cable. (a) First mode, (b) Second mode, (c) Third mode.

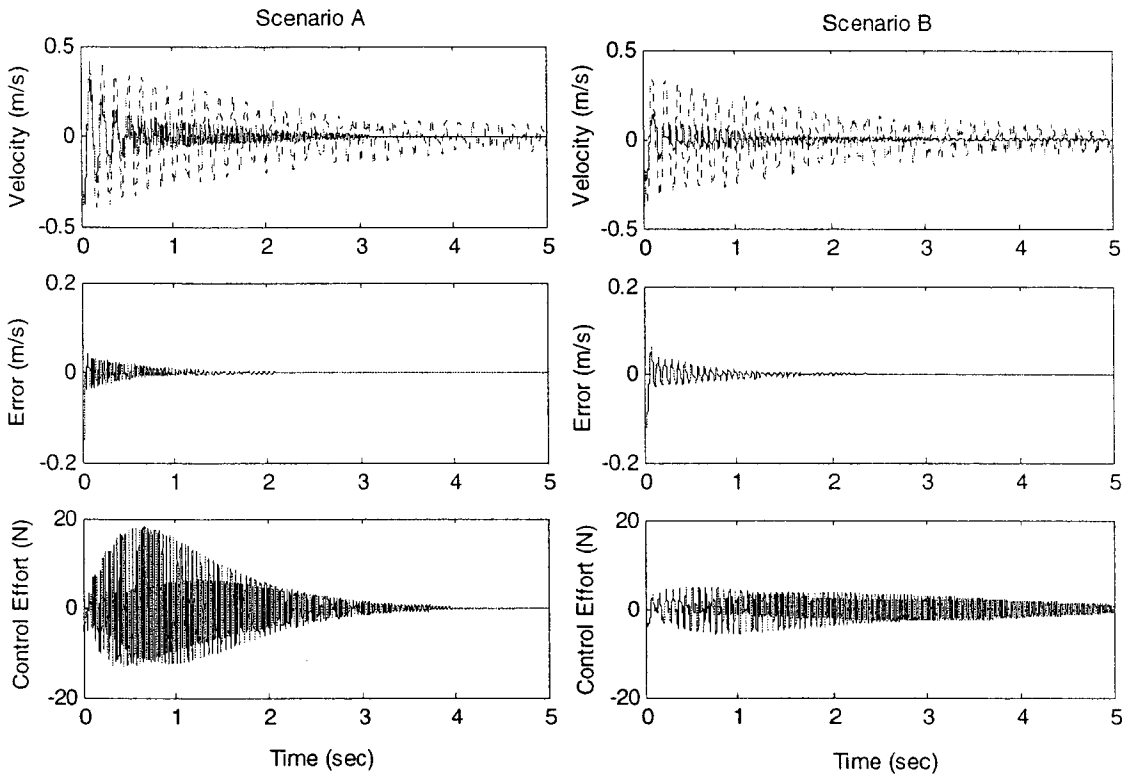

Figure 6.13: Observer-based control system simulation results. (a) Velocity output, (b) Error, (c) Control effort.

From Figures 6.11 to 6.13, the following observations are inferred:

- The magnitudes of both the generalized displacements and velocities are greatly reduced in both scenarios.
- The lateral velocities of the actuator are reduced during the cable-travelling period in both scenarios.
- A greater control effort is needed in Scenario A.

From the simulation results, the ability of the observer-based feedback control for suppressing the moving cable vibration of the experimental system can be predicted.

6.4 Summary

The model governing lateral vibration of the travelling cable is time-varying. With the boundary output and control, the system is both controllable and observable. However, the third mode is difficult to observe and control. An approximate observer-based feedback control was proposed. Computer simulations were performed to study the effect of the active control to the moving cable system. Simulation results were discussed. The simulation results indicated that the observer-based feedback control is capable of suppressing the moving cable vibration.

Chapter 7

SUMMARY AND FUTURE WORK

7.1 Summary

An experimental system has been developed to study the vibration of travelling cables with variable length. The developed travelling cable apparatus has met most of the design requirements. An actuator has been also designed to generate a non-contact actuating force to the lower end boundary of the cable. A signal conditioning system has been developed to condition the signals from the sensors, the DC motor, the actuator, and the computer system.

Two stationary cable models with different boundary conditions have been studied. The travelling cable model has been also developed. The boundary control method has been used to control the vibration of the cable. State-space representation of stationary and travelling cable models have been presented for the purpose of developing boundary control strategies.

To better understand the dynamics of the travelling cable apparatus and the actuator, a preliminary testing has been done. The natural frequencies of the stationary cable with different boundary conditions have been determined. The stiffness and damping ratio of the plate spring have been found. The relationship between the magnitude of the actuator acceleration and the voltage applied to the actuator has been also examined. A position control for the DC motor has been implemented.

The tension of the cable has been intentionally reduced to increase the magnitude of the cable's vibration. The implementation of active boundary control techniques has focused on the stationary cable system only. Two active control methods have been investigated, namely the direct feedback control method has been presented. Computer simulations have been performed to study the difference between the direct displacement feedback and the direct velocity feedback. System identification has been done. The direct velocity feedback control has been implemented.

The observer-base feedback control has been employed. The dynamics of the actuator has been included in the model. The input and output gains have been determined experimentally in order to match the model with the real system. The LQR method was used to design the optimal feedback gains used to stabilize the stationary cable system and the observer system. Computer simulations were conducted to study the effectiveness of the observer-based feedback control. The observer was also successfully implemented to estimate the actual velocity output measured from the stationary cable system and to perform full state feedback control through the actuator. The experimental results show that the observer-based feedback control can suppress the vibration of the stationary cable system.

Further, an observer-based feedback control system was also designed to suppress the vibration of the moving cable system. Pre-defined feedback gain equations were used to generate the optimal feedback gain matrices while the cable was travelling. Computer simulations were performed to study the effect of the active control to the moving cable system. The simulation results show that the observer-based feedback control is capable of suppressing the moving cable vibration.

7.2 Future Work

The original objective of this research is to develop an active control system to control the vibration of the travelling cable. Some technical difficulties have been encountered during the study. The following are some suggestions for future work:

- Study the dynamics of the actuator system for more accurate control.
- Search for better material for the cable in order to increase vibration magnitude and the friction for vibration control of the travelling cable.
- Develop a better signal conditioning circuit to condition the vibration signal measured from the strain gauge.
- Implement the observer-based feedback control to the future modified experimental system to suppress the vibration of the travelling cable.

References

[1] Chi, R. M. and Shu, H. T., "Longitudinal vibration of a hoist rope coupled with the vertical vibration of an elevator car," *Journal of Sound and Vibration* 148 (1991), 154-159.

[2] Kaczmarczyk, S. and Ostachowicz, W., "Transient vibration phenomena in deep mine hoisting cables. Part 1: mathematical model," *Journal of Sound and Vibration* 262 (2003), 219-244.

[3] Kaczmarczyk, S. and Ostachowicz, W., "Transient vibration phenomena in deep mine hoisting cables. Part 2: numerical simulation of the dynamic response," *Journal of Sound and Vibration* 262 (2003), 245-289.

[4] Kumaniecka, A. and Niziol, J., "Dynamic stability of a rope with slow variability of the parameters," *Journal of Sound and Vibration* 178 (2003), 211-226.

[5] Lee, S. Y. and Lee, M., "A new wave technique for free vibration of a string with time-varying length," *Journal of Applied Mechanics* 69 (2002), 83-87.

[6] Terumichi, Y., Yasuda, K., and Kato. M., "Vibration of a string with time-variable length," *Bulletin of the Japan Society of Mechanical Engineering* 162 (1978), 1677-1684.

[7] Trumichi, Y., Ohtsuka, M., Yoshizawa, M., Fukawa, Y., and Tsujioka, Y., "Non-stationary vibrations of a string with time-varying length and a mass-spring system attached at the lower end." *Nonlinear Dynamics* 12 (1997), 39-55.

[8] Zhu, W. D. and Ni, S., "Energetics and stability of translating media with an arbitrarily varying length," *ASME Journal of Vibration and Acoustics* 122 (2000), 295-304.

[9] Zhu, W. D., "Control volume and system formulations for translating media and stationary media with moving boundaries," *Journal of Sound and Vibration* 254 (2002), 189-201.

[10] Zhu, W. D., and Xu, G. Y., "Vibration of elevator cables with small bending stiffness," *Journal of Sound and Vibration* 263 (2003), 679-699.

[11] Zhu, W. D., and Teppo, L. J., "Design and analysis of a scaled model of a high-rise, high-speed elevator," *Journal of Sound and Vibration* 264 (2003), 707-731.

[12] Misra, A. K. and Modi, V.J., Deployment and retrieval of shuttle supported tethered satellites, *J. of Guidance*, 5 (1982), 278-285.

[13] Behdinan, K., Stylianou, M. C., and Tabarrok, B., "Dynamics of flexible sliding beams. Non-linear analysis part II: Transient response," *Journal of Sound and Vibration* 208(1997), 541-565.

[14] Behdinan, K., and Tabarrok, B., "Dynamics of flexible sliding beams. Non-linear analysis part I: Formulation," *Journal of Sound and Vibration* 208(1997), 517-539.

[15] Wang, P. K. C. and Wei, J. D., "Vibrations in a moving flexible robot arm," *Journal of Sound and Vibration* 116 (1987), 149-160.

[16] Zajaczkowski, J. and Lipinski, J., " Instability of the motion of a beam of periodically varying length," *Journal of Sound and Vibration* 63(1979), 9-18.

[17] Wickert, J. A. and Mote, Jr. C. D., "Current research on the vibration and stability of axialy moving materials," *Shock and Vibration Digest* 20 (1988), 201-220.

[18] Wang, J. and Li, Q., "Active vibration control methods of axially moving materials," *Journal of Vibration and Control* 10 (2004), 475-491.

[19] Yang, B., and Mote, Jr. C. D., "Controllability and observability of distributed gyroscopic systems," *ASME Journal of Dynamic, System, Measurement, and Control* 113 (1991), 11-17.

[20] Chen, M. S. and Fu, R.J., "An active control design for a class of parametrically excited systems based on the gradient algorithm," *Journal of Vibration* and Acoustics 120 (1998), 727-732.

[21] Fung, R. F. and Tseng, C. C., "Boundary control of an axially moving string via Lyapunov method," *ASME Journal of Dynamic, System, Measurement, and Control* 121 (1999), 105-110.

[22] Fung, R. F., Wu, J.W., and Wu, S. L., "Stabilization of an axially moving string by nonlinear boundary feedback." *ASME Journal of Dynamic, System, Measurement, and Control* 121 (1999), 117-121.

[23] Fung, R. F., Chou, J.H., and Kuo, Y. L., "Optimal boundary control of an axially moving material system," *ASME Journal of Dynamic, System, Measurement, and Control* 124 (2002), 55-61.

[24] Shahruz, S. M., 2000, "Boundary control of a nonlinear axially moving string," *International Journal of Robust Nonlinear Control* 10 (2002), 7-25.

[25] Shahruz, S. M. and Kurnaji, D. A., "Vibration suppression of a non-linear axially moving string by boundary control," *Journal of Sound and Vibration* 201 (1997), 145-152.

[26] Zhu, W. D., Guo, B. Z., and Mote, Jr. C. D., "Stabilization of a translating tensioned beam through a pointwise control force," *ASME Journal of Dynamic, System, Measurement, and Control* 122 (2000), 322-331.

[27] Zhu, W. D., Ni, J., and Huang, J., "Active control of translating media with arbitrarily varying length," *ASME Journal of Vibration and Acoustics* 123 (2001), 347-358.

[28] Butkovskiy, A. G, Structural Theory of Distributed Systems, Halsted Press, Wiley, New York, 1983.

[29] Inman, D. J, Egineering Vibration, Prentice-Hall, Upper Saddle River, New Jersey, 2001.

[30] Kuo, B. C., and Golnaraghi, F., Automatic Control Systems, John Wiley and Sons, New York, 2003.

[31] Ogata, K., Modern Control Engineering, Prentice-Hall, Upper Saddle River, New Jersey, 2002.

[32] Rugh, W. J, Linear System Theory, Prentice-Hall, Upper Saddle River, New Jersey, 2000.